UC Berkeley
UC Berkeley Electronic Theses and Dissertations

Title

Vertebral Micromechanics and Failure Mechanisms

Permalink

https://escholarship.org/uc/item/33w734qw

Author

Wu, Tongge

Publication Date

2022

Peer reviewed|Thesis/dissertation

eScholarship.org Powered by the California Digital Library
University of California

Vertebral Micromechanics and Failure Mechanisms

by

Tongge Wu

A dissertation submitted in partial satisfaction of the

requirements for the degree of

Doctor of Philosophy

in

Engineering - Mechanical Engineering

in the

Graduate Division

of the

University of California, Berkeley

Committee in charge:

Professor Tony M. Keaveny, Chair
Professor Lisa Pruitt
Professor Per-Olof Persson

Spring 2022

Vertebral Micromechanics and Failure Mechanisms

Copyright 2022

by

Tongge Wu

Abstract

Vertebral Micromechanics and Failure Mechanisms

by

Tongge Wu

Doctor of Philosophy in Engineering - Mechanical Engineering

University of California, Berkeley

Professor Tony M. Keaveny, Chair

The overall objective of this work is to provide a fundamental understanding of changes in bone structure–function relationship and failure mechanism with the presence of a certain degree of degradation in bone micro–architecture. Since it is of scientific interest to illustrate the mechanism by which aging, disease, and environmental factors, such as ionizing radiation, affect bone morphology and consequently alter the bone mechanical behaviors. More importantly, such insights would also potentially enhance the assessment of bone fracture risk in a clinical setting.

Combing a small animal model, where the mouse vertebral body morphological changes were introduced by the whole–body ionizing radiation, with high–resolution micro–computed tomography (micro–CT) based finite element (FE) analysis, we demonstrated how ionizing radiation altered the mouse vertebral body micro–architecture, structure-function relationship, as well as the failure mechanism. Our key results showed a reduction in trabecular mass fraction (by 12.8% on average, $p = 0.0014$) and a reduction in trabecular load fraction as the trabecular mass fraction was controlled (by an 8% decrease in the linear correlation slope, $p = 0.0264$). Related to this, nonlinear FE results showed that there were a reduction in the mouse vertebral stiffness (by 7.4%, $p = 0.0054$), a reduction in the vertebral strength (by 8.8%, $p = 0.0002$), and an significant offset for the linear correlation between them ($p = 0.011$) due to changes in the volume of failure tissue ($p = 0.036$). Our results suggested that, following ionizing radiation, the loss of trabecular load sharing could be more substantial than the loss of mass sharing since the trabecular structure–function relationship was altered. Moreover, the loss of vertebral strength could be more significant than the loss of vertebral stiffness, as the failure mechanism was altered. Such insights may apply to changes in vertebral micro–architecture induced by aging and diseases.

Using eight human vertebral body specimens with high–resolution micro–CT based nonlinear FE analysis, we established the damage law for the human vertebrae. The key results were that the human vertebral body damaged tissue accumulated exponentially as the axial compressive load applied (max $p = 0.04$, min $R^2 = 0.98$), and the damaged tissue growth rate was nonlinearly correlated with the whole–bone strength ($p < 0.001$). With the aid of two simplified analytical

models, our results implied that a weak human vertebra accumulated fracture tissue at a higher rate than a strong one due to a low number of vertical load paths.

In closure, this work presents the fundamental mechanisms by which changes in vertebrae morphology translate into alterations in the vertebrae structure–function relationship and failure mechanism, then ultimately into alterations in vertebrae strength and fracture risk.

To Mom and Dad

Contents

Contents **ii**

List of Figures **iv**

List of Tables **vii**

1 Introduction **1**
1.1 Composition and Structure of Bone 4
1.2 Mechanical Performance of Bone 5
1.3 Numerical Methods for Bone Biomechanics 8
1.4 Novelty of This Work 10
1.5 Objectives and Scopes 11

2 Structure–Function Relationship and Load–Sharing within Irradiated Murine Vertebral Body **24**
2.1 Introduction 24
2.2 Methods 25
2.3 Results 27
2.4 Discussion 28

3 Distinct Changes in Bone Stiffness and Strength in Irradiated Murine Vertebral Body **35**
3.1 Introduction 35
3.2 Methods 36
3.3 Results 38
3.4 Discussion 38

4 Damage Law and Structural Redundancy in Human Vertebral Body **46**
4.1 Introduction 46
4.2 Methods 47
4.3 Results 49
4.4 Discussion 50

5 Conclusion and Future Works **61**

6 Reference **65**

List of Figures

1-1 Comparison of frontal slices (1 mm of thickness) from the vertebral body of a healthy (left) and an elderly (right). The osteoporotic one (right) shows significant loss of bone mass and deterioration of the trabecular micro–architecture. 14
1-2 Distribution of BMD in women of different ages. The prevalence of osteoporosis is indicated by blue area under the curve. (Taken from [13]) 15
1-3 Mechanistic pathways to mechanical failure of bone (Taken from [26]) 16
1-4 Hierarchical structure of bone tissue. Left to right: Haversian bone, lamellae, mineralized collagen fiber, collagen fibril, and collagen molecules with hole zones filled by minerialization. (Taken from [150]) 17
1-5 Schematic diagram of cortical and trabecular bone showing the different micro–structures. (Taken from [45]) 18
1-6 Typical stress–strain behavior for human cortical bone. The bone is stiffer in the longitudinal direction, indicative of its elastic anisotropy. It is also stronger in compression than in tension, indicative of its strength asymmetry. (Taken from [36]) 19
1-7 Log–log plots for (a) trabecular Young's modulus and (b) trabecular compressive yield strength as functions of trabecular apparent density. Lines indicating power–law exponents of one and two are drawn on the plots. (Taken from [5]) 20
1-8 Box plots with gender differences in age–matched groups for (a) maximum failure load, (b) apparent bone volume fraction (app. BV/TV), (c) apparent trabecular number (app. Tb. N), (d) apparent trabecular separation (app. Tb.Sp), (e) apparent trabecular thickness (app. Tb.Th), and (f) fractal dimension (Frac. Dim). (* $p < 0.05$, ** $p < 0.01$, and *** $p < 0.001$). (Taken from [76]) 21
1-9 Micro–CT images of transverse cross sections from the caudal region of representative L5 mouse vertebrae, showing the effects of three different one-time radiation doses (0, 1, or 5 Gy) after 11 days or 12 weeks (all different animals). (Taken from [146]) 22
1-10 Illustration of overall non-uniform and complex stress distribution for the frontal slices within a human vertebral body specimen. Arrows point a exemplar region whose stress-state was in light compression, heavy compression and heavy tension at various levels of apparent applied compressive loading. Data presented are taken from **Chapter 4**. 23

2-1 A – F: Absolute trabecular (left column) and cortical (right column) bone mass, mass fraction, load fraction, and difference between mass fraction and load fraction as functions of axial position in the vertebral body. Data are shown as mean ± SD. $* : p < 0.05, ** : p < 0.01, \dagger : p < 0.001$. G – H: no t–test between groups performed. 31
2-2 Scatter plot showing the independent relationships between trabecular mass fraction and load fraction from the control (n = 14 × 10, number of specimens × ten axial sections per specimen) and treatment group (n = 13 × 10). R^2 and p–values are as shown from univariate linear regression. A mixed–effects linear regression model with an interaction term demonstrated a statistically significant interaction between groups ($p < 0.03$). 32
2-3 Mean ± SD initially–failed tissue volume in the (A) cortical compartment (B) trabecular compartment and (C) whole vertebral body for control and treatment groups. The initially–failed tissue volume was calculated for each specimen on a relative basis by normalizing the initially–failed tissue volume by the total bone volume of that specimen. Cross-hatching in the vertebral body initially–failed tissue volume indicated a direct comparison between the trabecular (hatched) and cortical (un–hatched) compartment. Percent differences were calculated relative to the control group. $* : p < 0.05, ** : p < 0.01$. 33
2-4 Representative distribution of initially–failed tissue in tension (red) and compression (blue) at three locations in the vertebral body for the control (upper row) and treatment group (lower row). The caudal, middle, and cranial locations were defined at 10%, 50%, and 90% of the vertebral body height, respectively. 34

3-1 Scatter plot of the vertebral body stiffness and strength for both control (N = 27) and treatment (N = 26) groups. R^2 and p–value were for linear regression of the control and irradiated group separately. Multivariate regression model was use to study the effect of treatment on the strength independent of the effect on stiffness, with p–value = 0.01. The difference of intercept was 0.48 N, which was 29% of the difference of strength between two groups, and 2.6% of the mean strength of the control group. . . . 41
3-2 Definition of the strength offset was derived from the correlation between vertebral stiffness and strength. Strength offset, as shown, was the vertical distance between a mouse vertebral strength to the translated regression line of that group, which passed the origin. The physical interpretation was the portion of vertebral strength that was not correlated with the vertebral stiffness. 42
3-3 Scatter plot of the vertebral body strength offset and vertebral body failure tissue for both control (N = 27) and treatment (N = 26) groups. R^2 and p–value were for linear regression of the control and irradiated group pooled. 43
3-4 Mean ± SD vertebral body, trabecular, and cortical failure tissue for control and irradiated group. Difference in percentage is from irradiated group minus control group. N = 27 for control group, and N = 26 for irradiated group ($* : p < 0.05, \dagger : p < 0.001$). 44

3-5 The mean $\pm$ SD trabecular and cortical failure tissue at five equal–distance sub–steps (0.4%, 0.8%, 1.2%, 1.6%, 2.0% apparent strain) for both groups. The symbol indicates significant difference between the control and treatment group for that compartment ($** : p < 0.01; \dagger : p < 0.001$). N = 13, 13 (L4 only) for control, irradiate groups, respectively. 45

4-1 An illustration of two simplified analytical models. The first row shows the first analytical model (two structures out of six) with a varying number of parallel load paths. The arrow indicates the applied loading direction. The second row shows the second analytical model (two structures out of six) with constant structural mass. 54
4-2 The force–deformation curve of one human vertebral body specimen, acquired from an iterative finite element analysis. Each dot (excluding the one at the origin) was a data point from a nonlinear (both geometric and material–wise) finite element analysis. The applied load was chosen to minimize the computational burden in the linear region on the force–deformation curve and maximize the resolution beyond the linear region. . 55
4-3 (A) The scatter plot of the number of load paths in structures and the corresponding structural strength in the first analytical model. (B) Logarithm transformed fracture tissue and applied load relationship of six structures. The fitted line indicated the linear regression. (C) The fracture tissue growth rate and strength relationship of all six structures. The solid line indicated the nonlinear regression of a 3–parameter exponential model. 56
4-4 (A) The scatter plot of the number of load paths in structures and the corresponding structural strength in the second analytical model. (B) Logarithm transformed fracture tissue and applied load relationship of six structures. The fitted line indicated the linear regression. (C) The scatter plot of fracture tissue growth rate and strength of all six structures. 57
4-5 (A) The damaged tissue and (B) logarithm transformed damaged tissue and applied load relationship of three representative human vertebral body specimens (specimen L, M, and H from **Table 4-1**). The fitted line indicated the (A) exponential regression and (B) linear regression. 58
4-6 The damaged tissue growth rate and strength relationship of all eight human vertebral body specimens. The solid line indicated the nonlinear regression of a 3–parameter exponential model. 59
4-7 The visual representation of bone density distribution (row 1), stress distribution at 75% (row 2), 50% (row 3), 25% (row 4) vertebral height, and damaged tissue distribution (row 5) of three representative human vertebral body specimens (specimen L – left column, M – middle column, and H – right column from **Table 4-1**). Bone density distribution was 2D projection to the top–view. Stress distribution was colorized compression stress at 0.4% apparent strain. Damaged tissue distribution was 2D projection to the top–view overlaying on a bone density distribution projection. Damaged tissue was tissue with maximum principal strain higher than 0.33% or minimal principal strain lower than -0.69% at 0.4% apparent strain. 60

List of Tables

1-1 Commonly reported definition and description of 3D outcomes for trabecular bone micro–architecture. (Taken from [46]) 13

2-1 Microarchitectural measurements and computational stiffness data (mean ± S.D.) for control and irradiated groups. p-value was from the t-test between two groups, bold indicated statistical significance. The percentage difference was calculated relative to the control group. N = 14, 13 for control, irradiated groups, respectively. 30

4-1 Eight specimen strength values, correlation p–values, and R^2 values for the relationship between transformed damaged tissue and strength. Specimen ID as letter were specimen used in **Figure 4-5** and **Figure 4-7** as the representative specimens with relatively low–(L), medium–(M), and high–(H) strength among all specimens. 53

Acknowledgments

Indeed, I cannot finish my Ph.D. without the help of a significant number of professors, mentors, friends, and my family. Here, my gratefulness is far more than following words.

My academic advisor, Professor Tony Keaveny, led me on the way from being a good student to becoming a real researcher. Besides the scientific and clinical research techniques, he always addresses how important rational and critical thinking are in academic and industrial environments. If there is only one thing I can remember about him, that would be (not the exact quote) – "You never know if your idea makes sense until you write it down." At the same time, he is also a fantastic instruction partner to work together. We have been through many Berkeley undergraduate– and graduate–level classes, and it never gets bored to learn from his pedagogical style. (Perhaps) As the last Ph.D. candidate in his academic profession at Berkeley, I hope I did not let him down.

Very same appreciation to my Qualifying Exam Committee and Dissertation Committee, including Prof. Lisa Pruitt, Prof. Per-Olof Persson, Prof. Shawn Shadden, and Prof. Grace Gu. And to those who taught me so much in every classroom, whether fundamental or advanced, leadership or hard-core technical, including Prof. Lin Lin, Prof. Panayiotis Papadopoulos, and Prof. James Demmel.

Thirdly, a big Thank You to all my lab– and office–mates. Dr. Megan Pendleton, thank you for positioning all those scientific questions and kindly providing the existing dataset, so my research could have a great starting point. Dr. Saghi Sadoughi, Dr. Noah Bonnheim, and Dr. Shannon Emerzian, thank all of you for the sharing, collaboration, mentorship, friendship, and support in all aspects. Particularly, Shannon, I really miss those cakes from your bakery. Outside my lab group, I want to appreciate Bo Yang for sitting beside me for the first few years, for helping me settle down in a place thousands of miles from home, and for all the miles we cycled together. Appreciate Zhizhun Shao for being an amazing best friend and for all the ridiculous but fun things we did together. Lastly, I want to thank Emily Lindberg for being the best running partner. Cheers for every single mile (plus wind, mist, chillness, and more) on the tarmac and dirt we conquered together.

Lastly, but most importantly, my Mom and Dad. No word can describe how much I love you and appreciate you. The closest I found is – "I am strong when I am on your shoulders; you raise me up to more than I can be."

Chapter 1

Introduction

As a living tissue in the human body's skeleton, bone supports the body weight, provides an extensive range of motion, protects vulnerable internal organs, and plays a role in minerals storage and blood cells development environment [1]. Like almost all living tissues, bone is subject to aging and various diseases, which could increase the risk of fracture at multiple anatomical sites [2, 3, 4, 5]. One of the most common diseases is osteoporosis (**Figure 1-1**). Osteoporosis means 'porous bone', which occurs when the body loses too much bone, deposits too little bone, or both (Bone Health and Osteoporosis Foundation). As a result, osteoporotic bone is characterized by micro–architecture deterioration and loss of bone mass, which increases bone fragility and susceptibility to fracture [6]. According to the Bone Health and Osteoporosis Foundation (previously National Osteoporosis Foundation), 54 million Americans are living with osteoporosis and low bone mass, which translates to one in two women and up to one in four men aged 50 or above may experience osteoporosis–induced bone fractures.

Among more than 2 million (of the year 2005, predicted over 3 million by 2025) osteoporosis–related fracture cases in the USA, 27%, 21%, and 19% of them occur in the vertebrae, the hip, and the distal forearm, respectively [7]. Hip fracture mortality and morbidity burdens are the most significant among all fracture types. Approximately 31,000 annual deaths occur within six months of hip fracture in the USA, and the rate of death has been shown to persist for up to 10 years post–fracture. Half of those individuals who were ambulatory prior to hip fracture are unable to mobilize independently post–fracture [8, 9]. As for vertebral fractures, the prevalence may be underestimated as many fractures are asymptomatic, and therefore, individuals do not seek medical attention. Furthermore, among those who experience a vertebral fracture, especially among older women, vertebral fractures usually occur due to everyday activities such as lifting and bending, but not due to trauma such as falling [8]. Associated morbidity of vertebral fractures includes back pain, kyphosis, and reduction in life quality [10, 11].

Additional to the social burden of osteoporosis–related fracture, the economic burden is also

significant, costing about $17.9 billion in the USA per year (projected to be around $50 billion by the year 2040) [8, 12]. Thus, there is a clear motivation to improve the screening and management of osteoporosis and osteoporosis–related fractures, which requires a fundamental understanding of the biomechanical aspect of the bone.

Osteoporosis is defined around the concept of bone mineral density (BMD), which can be measured using various methods, including dual X–ray absorptiometry (DXA), quantitative ultrasonic, quantitative computed tomography (QCT), or as simple as direct radiographs estimation [13, 14]. DXA is the current standard by World Health Organization (WHO) among those methods and is widely used. The principle of DXA is providing a two–dimensional areal BMD, which compresses the information of bone size and bone mineral content (BMC) [13]. BMD derived from DXA can be used as a predictor of fracture risk; such prediction was proposed by WHO and modified by the International Osteoporosis Foundation (**Figure 1-2**): Normal – hip BMD greater than one standard deviation (SD) below the young adult female reference mean (T score $\geq$ -1). Osteopenia – hip BMD less than 1 SD below the young adult female reference mean but greater than 2.5 SD below this value (-1 $>$ T score $>$ -2.5). Osteoporosis – hip BMD 2.5 SD or more below the young adult female reference mean (-2.5 $\geq$ T score). Severe osteoporosis – hip BMD 2.5 SD or more below the young adult female reference mean in the presence of one or more fragility fractures [15, 16]. The young adult female mean–value is from a reference database of women aged 20 – 29 years of the National Health and Nutrition Examination Survey [15]. While the BMD threshold values are well defined for women, general categories are not obvious for men. Many studies examining fracture risk in men and women have variously concluded that the fracture risk threshold values are the same or differ between sexes [17, 18].

The clinical consequence of osteoporosis (T score $\leq$ -2.5) is arising fracture risk; that is, quantitatively, the fracture risk doubles for each SD reduction in the BMD derived from DXA, though the increase of fracture risk depends on anatomic sites and age [19]. One major disadvantage of BMD measurement is the low–sensitivity, which means a normal BMD is far from guaranteeing that fracture will not occur. For example, 96% of hip, vertebrae, or distal forearm fractures occur in women without osteoporosis (thus, sensitivity at 4%). Conversely, an osteoporotic BMD measurement only indicates a higher likelihood of fracture since around 45% of women with osteoporosis will fracture their hip, vertebrae, or distal forearm (precision at 45%) [20]. Therefore, more recent screening methods are developed to address the DXA low sensitivity, such as the FRAX tool [21].

Fracture Risk Assessment Tool, or FRAX algorithm, takes seven dichotomous clinical risk factors (CRFs: prior fragility fracture, parental hip fracture, smoking, systemic glucocorticoid use, excess alcohol intake, rheumatoid arthritis, and other cause of secondary osteoporosis), together with age, sex, and body mass index (BMI), to calculate a 10–year fracture probability, independent of BMD measurement [22]. The ability to predict fracture, traditionally expressed as the increase in hazard ratio per SD unit increase in risk score (also called the gradient of risk), is significant

for BMD–only or CRFs–alone but is the highest for FRAX with BMD as additional input [23]. By figures, the mean value of the gradient of risk for hip fracture at the age of 60 is 3.07, 1.95, and 3.51 for BMD–only, CRFs–alone, and CRFs combined with BMD, respectively [24]. Since its launch in 2008, the FRAX tool has been used in 66 countries. There are around 3 million visits per year, and it is available for more than 80% of the world population [22]. Although FRAX shows capability for case finding in the absence of BMD, the major limitation is the interpretation of the prediction, such as fixed intervention threshold or age–adjusted intervention threshold [22, 25]. Overall, the unsatisfied low sensitivity of osteoporosis screening (both BMD and FRAX) suggested the complex relationship between fracture risk (of the hip, vertebrae, or distal forearm) and observable bone properties (including BMD, bone size, bone strength, etc.).

From a biomechanical perspective, the bone fracture risk inherently depends on two aspects: the loading situation and the bone structural properties, that is, the ability of bone to resist mechanical failure [26] (**Figure 1-3**). The loading situations are determined mainly by the kinematic of bone and neighboring muscles, attached ligaments, and physiological activities [27, 28, 29]. For example, it is estimated that over 90% of hip fractures in the elderly occur at a fall, which involves a monotonic impact loading, where the peak force can be as high as 5574 N in a simulated side–way fall (well exceeds the average femoral strength in the elderly) [30, 31]. Thus, the strength or toughness of the femoral neck, femoral head, and pelvic are studied for such application [32, 33]. By contrast, 60% of detected vertebral fractures are spontaneous, which occur during normal activities, suggesting a damage accumulation process due to repetitive compression, bending, or torsional loadings [34]. During each cycle, the force or moment could be well below the corresponding strength of the vertebrae. Therefore, the fatigue properties of the vertebral body are the topic of many studies [26, 31, 35]. Bone structural properties, such as strength, are associated with bone mass, bone micro–architecture, and bone tissue–level properties [26]. The subsequent section will cover these relationships in detail. On a high level, these relationships suggest that there may be a convoluted pathway by which how bone mass, bone micro–architecture, bone tissue-level properties, or changes of one or more of them due to aging or disease could affect bone structural properties [31]. Understanding this convoluted pathway may help researchers explain the aforementioned low sensitivity of a fixed BMD or a fixed FRAX 10–year fracture probability threshold. Therefore, this work will focus on the relationship between bone micro–architecture and bone structural properties, including stiffness, strength, and failure mechanism, in both murine and human vertebral bodies.

The remainder of this chapter is to provide fundamental pieces of knowledge for subsequent chapters. First, we start with biological and engineering perspectives on bone composition and hierarchical structure. Then, the second section covers the biomechanical aspects of the vertebral body, including whole–bone level mechanical properties and how aging, diseases, and other environmental factors affect those properties. Following that, we provide some advantages, disadvantages, and current challenges of numerical modeling of the vertebral body. At last, the novelties, objectives, and goals of this dissertation are stated.

1.1 Composition and Structure of Bone

Bone is made of inorganic phase, organic phase, and water. On a weight basis, bone is approximately 60% inorganic, 40% organic, and 10% water; whereas on a volume basis, bone is about 40% inorganic, 35% organic, and 25% water [36]. The inorganic phase of bone is mainly crystalline–type hydroxyapatite, with impurities of carbonate, magnesium, and acid phosphate [37]. The organic phase is primarily type–I collagen (90% by weight), some other minor collagen types (III and VI), and a variety of non–collagenous proteins. At the nanometer scale, type–I collagens are arranged in parallel with each other head–to–tail with a gap of approximately 40 nm between each molecule [36]. Mineralization begins in these hole zones and extends into other intermolecular spaces, thus, resulting in a mineralized collagen fibril (about 30 nm in diameter and 300 nm in length) [38].

Bone is a hierarchical structure with the basic unit as mineralized collagen fibril (at 0.1 μm scale) (**Figure 1-4**). At 1 – 10 μm scale, mineralized collagen fibrils are found stacked as thin sheets called lamellae (about 7 μm thick), which contain unidirectional fibrils in alternating angles between layers; alternatively, mineralized collagen fibrils form a block of randomly oriented woven fibrils. Lamellar bone is commonly found in the adult human, whereas woven bone is often found in situations like rapid growth or an initial fracture healing process. At the next level of scale, primary lamellar bone is new tissue consisting of large concentric rings of lamellae that circle the outer 2 to 3 mm of the long bone diaphysis. Haversian bone consists of 10 to 15 lamellae arranged in a concentric cylinder about a central Haversian canal (diameter of 50 μm), which contains blood vessels, nerves, and a variety of bone cells. Laminar bone is made of a series of concentric laminae (each lamina about 100 – 200 μm thick) around the marrow cavity [36, 39].

At the largest scale level (1 – 5 mm), there are two distinct types of bone: cortical bone and trabecular bone (**Figure 1-5**). The former consists of tightly packed lamellar, Haversian, or woven bone. In the cortical bone, concentric lamellae and the Haversian canal have termed an osteon (about 200 μm in diameter and 1 – 3 mm in length), which is the basic unit of bone remodeling (or turnover). Between Haversian canals, Volkmann's canals run transversely to provide radial paths for blood flow. Trabecular bone, on the other hand, is commonly found in the diaphysis of long bone and centrum of the vertebrae and consists of a network of rods and plates (called trabeculae, about 100 – 300 μm thick) formed by less well–organized lamellar packets [36]. Typically, cortical bone is defined as bone tissue with a volume fraction higher than 70%; trabecular bone is then bone tissue with a volume fraction less than 70%. Here, the volume fraction is defined as the actual bone tissue volume divided by the specimen bulk volume. A related definition is an apparent density (i.e., specimen–level, in contrast to the tissue–level), which equals volume fraction multiplies tissue density, where tissue density is the actual bone tissue–level mass density. Tissue density is similar in cortical and in trabecular bone (about 2.0 g/cm^3), thus, the apparent density of cortical (about 1.85 g/cm^3) and trabecular bone (as low as 0.1 g/cm^3 in the spine and up to about 0.6 g/cm^3 at the proximal femur are mostly determined by the volume fractions [40, 41, 42].

For the trabecular bone, the variation of apparent density – including the information of bone volume fraction and tissue density – can explain most of the variation of the apparent mechanical behaviors such as apparent modulus and apparent strength [43, 44]. However, the scatter in apparent mechanical behaviors for any particular value of apparent density suggests that the micro–architecture (or morphology) of the trabecular bone, namely the shape and arrangement of the rod– and plate–like trabeculae, also affect trabecular bone apparent mechanical behaviors [45]. In the field of bone biomechanics, high–resolution micro-computed tomography (micro–CT) is widely used to scan and measure the micro–architecture of trabecular bone. A typical resolution is on the order of 10 μm, which is sufficient for human and large animal trabeculae (about 100 – 200 μm thick) and can be as low as a few μm for small animal models (e.g., mouse) [46]. Among a variety of possible quantitative descriptions of trabecular micro–architecture, there is a minimal set across multiple studies: bone volume fraction, trabecular number, trabecular thickness, and trabecular separation [46, 47]. Additionally, connectivity density and Structural Model Index (SMI) provided more information about the topology and shape of trabeculae [48, 49] (**Table 1-1**).

1.2 Mechanical Performance of Bone

As a hierarchical composite material, bone demonstrates different mechanical properties at different scales [5]. For this chapter, we will focus on a scale of 1 – 10 mm. At this scale, cortical bone specimens were commonly shaped like a dumbbell, and trabecular bone specimens were usually in a cylindrical shape (length at 10 – 50 mm, the aspect ratio is about 3 – 10) [42, 50]. In both cases, the longitudinal (main) axis was the direction of the test. Moreover, at this scale, trabecular bone mechanical properties were defined as apparent mechanical properties, as opposed to the tissue–level mechanical properties. Among the mechanical properties related to the clinical bone fracture risk, stiffness (unit N/mm) reflects the capability of bone to resist deformation under certain types of loading, and strength (unit N) reflects the maximum level of loading a bone specimen could resist. On a force–deformation (or stress–strain) graph, the stiffness (modulus in unit MPa, if stress–strain curve) was measured as the slope of the curve in the linear region, and the strength (ultimate stress in unit MPa, if stress–strain curve) was measured as the peak of the curve along the vertical axis. Other mechanical properties related to the bone fracture risk include fracture toughness (unit $MPa\sqrt{m}$), which measures the capability of bone to resist the crack propagation, and fatigue life (unit cycles) which measures the capability of bone to resist repetitive but subcritical loadings.

Human cortical bone is observed as a transversely isotropic material (**Figure 1-6**) [50]. Along the longitudinal direction, the modulus of cortical bone is $18.1 \pm 1.7\ GPa$, which is 2 – 3 folds of the modulus in the transverse direction (for all directions in the transverse plane) [50, 51, 52]. Additionally, human cortical bone strength is asymmetric with respect to the loading direction. While the compression ultimate stress for cortical bone is about $205 \pm 17.3\ MPa$ (in the longitudinal direction, $131 \pm 20.7\ MPa$ in the transverse direction), the tensile ultimate stress is only about $135 \pm 15.6\ MPa$ (in the longitudinal direction, as low as $53 \pm 10.7\ MPa$ in the transverse direction)

[50]. The modulus of human trabecular bone heavily depends on age, anatomic site, and orientation of the loading, which can vary as much as 100–fold with a typical range of $10 - 3000\ MPa$ [42, 53, 54]. Affected by the same preceding factors, the strength of human trabecular bone is strongly and linearly correlated with the modulus, and a typical value is between $0.1 - 30\ MPa$ [55].

At 1 – 10 mm scale, mechanical properties inherently depend on bone porosity, micro–architecture (of trabecular bone), and tissue–level properties [5]. For both cortical and trabecular bone, modulus, strength, and fracture toughness are negatively (linearly or exponentially) correlated with porosity [42, 56, 57, 58, 59]. Changes in the porosity could explain about 75% of changes in the cortical strength [60], 70 – 90% of changes in the trabecular modulus [61], and 60 – 80% of changes in the trabecular strength [62, 63] (**Figure 1-7**). In addition to porosity, SMI (one measurement of trabecular micro–architecture) and vertical trabecular bone volume fraction may also explain a significant amount of the changes in the trabecular strength [64, 65]. Moreover, at the tissue level, an increase of collagen cross–linking, specifically via non–enzymatic, has been associated with reductions in cortical bone strength and fracture toughness [66]. And such effect on human trabecular bone is also excepted given the tissue–level composition similarity between the cortical and trabecular bone [67].

Aging and several diseases have been extensively studied due to the resulting arising bone fracture risk in the clinical observations [68]. The etiologic pathway starts at alterations in bone volume fraction (equivalently, in bone porosity or bone mass), bone micro–architecture, and bone composition. Then, on the macro–level, these changes translate to alterations in bone strength or bone fatigue properties. Eventually, bone mechanical properties changes introduce alterations in bone fracture probability under physiological or eventful loadings [69]. In general, after the third decade of life, human cortical bone shows increased porosity, and trabecular bone shows decreased trabecular number, trabecular thickness, and trabecular connectivity density [70, 71, 72, 73]. Additionally, with increased age, material–wise changes occur, such as increased mineral–to–matrix ratio, increased collagen cross–linking ratio, and increased crystallinity [74, 75]. Together, those changes result in observable increased bone fragility.

For age–related osteoporosis, sex difference adds one more variable to the bone fragility equation. For example, older women with osteoporosis have lower bone volume fraction, trabecular thickness, and ultimate trabecular bone stress than older men with osteoporosis (**Figure 1-8**) [76]. Compared to age–controlled women without fracture incidence, osteoporotic women with fracture history show lower BMD and larger variation in matrix mineralization in the vertebral body, as well as lower BMD and greater crystallinity in the iliac crest [77, 78, 79]. Although there are fewer studies of osteoporotic men, some evidence shows increased trabecular separation and decreased trabecular number in the group with fracture incidence, compared to the group without one [80].

In addition to aging and aging–associated osteoporosis, osteomalacia describes a condition where the bone has insufficient mineralization [81], osteogenesis imperfecta describes genetic abnormalities where the bone lacks type–I collagen [82]. Finally, osteopetrosis describes bone that fails to remodel, therefore, retain extra calcified cartilage [83]. All composition–related bone diseases could significantly increase bone fracture risk but also provided views to study the origin of bone mechanical properties.

The mechanism by which bone quantity (or bone volume fraction) and quality (metrics other than the volume fraction) are affected by aging and aging–associated osteoporosis is the unbalanced bone turnover (or remodeling) [84, 85]. In a healthy status, osteoclasts (one type of bone cell) excavate a microscopic amount of bone, which is followed by osteoblasts (another type of bone cell) refilling it with newly mineralized osteoid (**Figure 1-5**) [86]. Such remodeling process is mainly signaled and controlled by osteocytes (the third type of bone cells) to either repair the microcracks or reshape the bone in order to adapt to varying physiological loadings [87]. Therefore, for osteoporosis patients, antiresorptive treatment is commonly used.

Antiresorptive treatment, such as risedronate and alendronate, have been shown to reduce bone turnover by approximately 35% (associated 49% reduction in the fracture risk) and 60% compared to the baseline in human studies, respectively [88, 89, 90]. Mechanistically, the first subsequence of a reduced bone turnover is the increased BMD. Animal studies show that a 15% increased BMD could translate to a 100% increase in trabecular bone strength [91]. A second result of the reduced bone turnover is a better trabecular micro–architecture. Evidence shows a decrease in the number and depth of resorption cavities and preservation of existing trabecular (trabecular number, thickness, and connectivity), which explains 91% changes in bone strength if combined with BMD measurement (compared to 80% if BMD alone) [84, 92]. The last direct subsequence of reduced bone turnover is a higher degree of mineralization. A modest increase in mineralization could explain the bone strength increases following antiresorptive treatment, independent of the bone volume fraction [93]. Together, studies suggest antiresorptive treatment increases bone strength and decreases bone fracture risk in a compounding manner [84]. However, such benefits depend on the anatomic sites. For example, vertebral body fracture risk appears to be plateau after a certain level of reduction in bone turnover, while nonvertebral fractures do not [94, 95]. Moreover, recent studies raise serious concerns about atypical fracture following a long–term (5+ year) antiresorptive treatment [96, 97, 98]. A few animal studies suggest that a severer suppression of bone remodeling could lead to accumulation of microcracks and increased non–enzymatic collagen cross–linking within bone tissue, therefore, decreasing the fracture toughness or fatigue life (up to three–fold) [99, 100, 101]. Additional concern includes a high degree of mineralization that may potentially lead to brittle bone tissue [96].

Like the osteoporosis associated with aging, ionizing radiation can also introduce significant bone loss and therefore increased bone fracture risk [102, 103]. Such effect is particularly inter-

esting and is being extensively studied for the long–term spaceflight and clinical radiation therapy (RT) applications [104]. Astronauts are subject to galactic cosmic radiation (GCR) and solar particle events (SPEs) in the cosmic environment. It is estimated that a 400–day of space travel near Earth would result in 0.16 – 0.32 Gy accumulated GCR dose, and an 8 – 24 hours SPE would result in 1 – 2 Gy of particles radiation ($1\ Gy = 1\ J/Kg$, indicating how much radiation energy per unit mass absorbed). By contrast, patients with gynecological or pelvic tumors commonly receive 54 Gy ionizing radiation during a six–week of treatment, where the dose absorbed by nearby bone tissue is about half of it (27 Gy) [102].

The long–term side effect of RT on bone quality has been well–documented [105, 106]. For example, rib fracture occurs after RT for breast cancer at the rate of 1.8% to 19% [107]; hip fracture risk increased by 65%, 66%, and 214% following RT for cervical, rectal, and anal cancer treatment, respectively [105, 108]. Mechanistically, ionizing radiation has been shown to rapidly increase osteoclast number and surface ($> 200\%$) as early as three days after the exposure [109], followed by a significant decrease of osteoblast number and matrix formation [110, 111]. Moreover, osteoblast precursors are likely damaged by the exposure, which makes the late effect more significant and delays the recovery [112]. Affected osteoclast and osteoblast activities are believed to contribute to the deterioration in bone mass and bone micro–architecture following ionizing radiation [113]. Studies have demonstrated that demineralization of bone, thinning of bone, and loss of trabecular connectivity occur as a consequence of RT [108, 113, 114] (**Figure 1-9**). In addition to the negative impact on bone mass and micro–architecture, ionizing radiation has been found to increase non–enzymatic collagen cross–linking, which leads to a decreased ultimate strain and fracture toughness of bone tissue [35, 66].

However, on the whole–bone level, animal models show controversial results in terms of how ionizing radiation affects the bone's mechanical properties. Some report a loss of vertebral stiffness (-10%) and no loss of vertebral strength following 2 Gy of iron ions [115], or a reduction of femoral strength following 5 Gy (-18%) and 12 Gy (-20%) of X–ray [116]. While others report increased compressive strength with a two weeks latency following the exposure [116]. This work will partially address such controversial observations in the subsequent two chapters.

1.3 Numerical Methods for Bone Biomechanics

Numerical methods, specifically the finite element method (FEM, or FEA for analysis), have been widely used in the field of bone biomechanics research. Compared to the conventional gold–standard experimental biomechanical testing, such as uniaxial compression on a vertebral body and 3– or 4–point bending on the femoral neck in a wet laboratory, high–resolution imaging–based finite element analysis (FEA) provides advantages that are otherwise impossible to implement in an experimental setting [117, 118, 119].

Firstly, it is non–destructive to observe the deformation and fracture behaviors of specimens *in silico*, which means parameter study with respect to material properties or boundary conditions is possible. With various boundary conditions, researchers can get multiple mechanical properties, such as compression stiffness, tensile strength, and bending toughness, of the same specimen [120, 121]. In addition, with selected assumptions in material properties, researchers can isolate the effect of material and micro–architecture on the whole–bone level mechanical properties [122, 123, 124]. For example, how tissue ductility may affect vertebral strength without any noise or variation from the trabecular morphology [125]. Secondly, simulations provide a better spatial and temporal angle of view to study the deformation and fracture of a specimen. While experimental results are on the apparent level, FEA can output the stress– or strain–distribution of bone tissue at any given location within the specimen at any given loading stage [126, 127, 128, 129] (**Figure 1-10**). Moreover, for a destructive experimental test (e.g., strength or fracture toughness measurement), FEA results can output the sequence and location of fractured bone tissue at any loading progress [130, 131]. The ability to virtually probe into the specimen is critical for studies focusing on the failure process and mechanism of the bone structure. A third advantage of the simulation comes from a calibration process with the help of experimental tests. For example, the modulus of human trabeculae is challenging to measure with high confidence due to the irregularity and small size of individual trabeculae [132]. With a proper calibration process, the tissue–level material properties can be easily acquired [133, 134, 119].

In the field of bone biomechanics, modern FEA includes two main approaches: continuum modeling–based FEA and high–resolution voxel–based FEA. The former requires images or volume information of the specimen on the scale of 1 – 5 mm, which are typical results from QCT or magnetic resonance imaging (MRI) [135, 136, 137]. The continuum modeling then uses the material properties as a function of spatial coordinates, determined by the pixel–wise color intensity. By contrast, the latter is derived from micro–CT with the scale of 5 – 50 μm. Thus, the micro–CT based FE model can capture the irregular shape of individual trabeculae and the connectivity between them, which simplifies the assumption of material properties to be homogeneous [119]. Both approaches have been validated against experimental tests under a variety of loading situations [138, 139, 140, 141, 142], and this work will utilize the micro–CT based FEM.

The main challenge of micro–CT based FEA is the intensive computational requirement from both software and hardware perspectives. In this work, the vertebral body of a small animal (mouse) model (physical scale about 2 mm in diameter and 2 mm in height [143]) has a degree–of–freedom (DOF) in the range of $4.4 - 7.7 \times 10^6$, and a human vertebral body (physical scale about 45 mm in M / L direction, 32 mm in A / P direction, and 30 mm in height) has DOF up to 186×10^6. Therefore, we used an implicit highly–scalable parallel framework (Olympus) to handle the computation work [144]. Briefly, Olympus is based on the Berkeley–owned parallel FEA solver (parFEAP [145]), which incorporates several state–of–art numerical libraries,

including PETSc [1], METIS [2], and ParMETIS [3], as well as a parallel input-output (IO) interface. The actual high-performance computing (HPC) is implemented on a state-of-art supercomputer (Stamepde2 [4], Texas Advanced Computing Center at The University of Texas at Austin), where each computing node (1736 nodes hosted) is equipped with two 24–cores Intel Xeon Platinum 8160 (Skylake architecture with hyper–threading technology) and 192 GB memory. In total, this work consumed about 161,000 CPU–hour computational resources, equivalently, about 18–year of continuous computing on a single–core processor.

1.4 Novelty of This Work

Previously, our research group has used an experimental approach to establish the effect of ionizing radiation on the mouse vertebral tissue–level ductility, bone mass, bone micro-architecture, vertebral stiffness, and vertebral strength. We reported relatively large differences in the vertebral tissue collagen cross–linking, the trabecular mass, and the trabecular micro–architecture induced by ionizing radiation; however, relatively small (and statistically not significant) differences in the vertebral stiffness and strength [146, 143, 147]. Such observations were inconsistent with a typical correlation between the bone morphology and bone mechanical behaviors [26]. Therefore, in this work, we used micro–CT based numerical approach to study the effect of ionizing radiation on the mouse vertebral micro–mechanics and structure–function relationship. This novel study design may help us interpret the previous observations from the experimental setting and, more importantly, understand the effect of ionizing radiation on bone micro-mechanics from a fundamental scientific viewpoint.

For the human vertebrae biomechanics, our group has extensively used the state–of–art high–resolution micro–CT based numerical approach to illustrate the deformation and failure mechanism of the human vertebral body. For example, we established the cortical–trabecular load–sharing mechanism in the human vertebral body [128], the initial failure tissue distribution at the cortical endplates and trabecular centrum [129], the strong correlation between trabecular SMI (structural model index), trabecular vertical bone volume fraction, failed tissue fraction and the whole–bone strength [148, 64, 149]. However, previous analyses focused on either the linear region of deformation or specific time steps of a nonlinear analysis, which did not provide the damage process across the entire loading range. Thus, in this work, we explored the inherent damage process of the human vertebral body and explained its relationship with the whole–bone strength using both

[1] PETSc is a suite of data structures and routines for the scalable (parallel) solution of scientific applications modeled by partial differential equations. link

[2] METIS is a set of serial programs for partitioning graphs, partitioning finite element meshes, and producing fill reducing orderings for sparse matrices. The algorithms implemented in METIS are based on the multilevel recursive-bisection, multilevel k-way, and multi-constraint partitioning schemes. link

[3] ParMETIS extends the functionality provided by METIS and includes routines that are especially suited for parallel AMR computations and large–scale numerical simulations. link

[4] Stampede2, generously funded by the National Science Foundation (NSF) through award ACI-1134872, is one of the Texas Advanced Computing Center (TACC), University of Texas at Austin's flagship supercomputers. link

analytical and numerical approaches. This novel study design may help researchers understand certain key aspects of the human vertebral fragility and fracture risk.

1.5 Objectives and Scopes

The overall objective of this work was to seek insights and improve understanding in the field of bone micro–mechanics. Bone micro–mechanics studies could help researchers clarify the fundamental relationship between bone micro–architecture and bone apparent mechanical behavior. More importantly, it is of scientific and clinical interest to understand the mechanism by which changes in bone morphology induced by aging, diseases, drug treatment, and environmental factors such as ionizing radiation translate to alterations in bone strength and, ultimately, fracture risk.

Chapter 2 was based on a previous experimental study where we found significant changes in mouse vertebral body micro–architecture but not observable changes in whole-bone stiffness following irradiation. This chapter was designed to explain such inconsistency using a linear computational approach. Mouse vertebral body mass–sharing, load–sharing mechanism, and high–stress tissue distribution were quantified and compared between the control and treatment groups. Those micro–mechanics measurements were taken to clarify the role of the trabecular and cortical compartments in the mouse vertebral body, which may bring insights into applications of aging– and osteoporosis–related studies.

Chapter 3 focused on the effects of ionizing radiation on mouse vertebral body stiffness, vertebral body strength, and any difference between them. This chapter used nonlinear computational models to quantify the changes in mouse vertebral body failure mechanism, such as fracture tissue spatial and temporal distribution following irradiation. These failure mechanism measurements were explored to explain the effect of ionizing radiation on bone strength independent of the effect on bone stiffness. Such explanations were valuable in elucidating the effect of aging or drug treatment on bone strength and fracture risk.

Chapter 4 explored the concepts of damage law and structural redundancy in the human vertebral body. This study used simplified analytical models and high–resolution micro–CT data of the human vertebral body to illustrate the damage process of the human vertebral body. Since the relationship between the damage process and whole–bone strength may illustrate if human vertebrae with different strengths fail in different manners. Moreover, the concept of structural redundancy in the human vertebral body was explored. This study could help researchers understand the mechanism by which degradation in bone porosity and micro–architecture manifests into increased fracture risk of human vertebrae.

At last, **chapter 5** list the conclusions and potential future directions based on this work.

Table 1-1: Commonly reported definition and description of 3D outcomes for trabecular bone micro–architecture. Variables in bold are the minimal set of variables that should be reported when describing trabecular bone morphology. (Taken from [46])

Abbreviation	Variable	Description	Standard unit
Tb. BV/TV	Bone volume fraction	Ratio of the segmented bone volume to the total volume of the region of interest	$\%$
Tb. N	Trabecular number	Measure of the average number of trabeculae per unit length	$1/mm$
Tb. Th	Trabecular thickness	Mean thickness of trabeculae, assessed using direct 3D methods	mm
Tb. Sp	Trabecular separation	Mean distance between trabeculae, assessed using direct 3D methods	mm
Conn.D	Connectivity density	A measure of the degree of connectivity of trabeculae normalized by total volume	$1/mm^3$
SMI	Structure model index	An indicator of the stucture of trabeculae; SMI will be 0 for parallel plates and 3 for cylindrical rods	

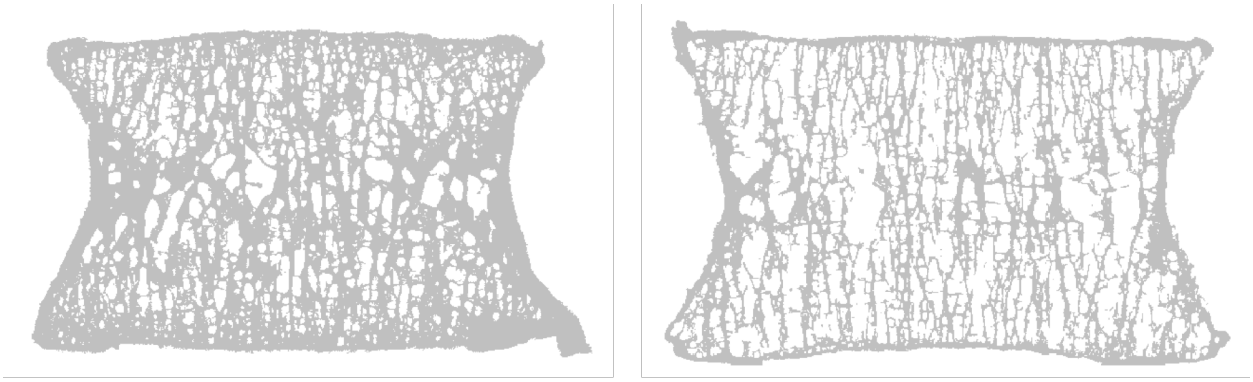

Figure 1-1: Comparison of frontal slices (1 mm of thickness) from the vertebral body of a healthy (left) and an elderly (right). The osteoporotic one (right) shows significant loss of bone mass and deterioration of the trabecular micro–architecture.

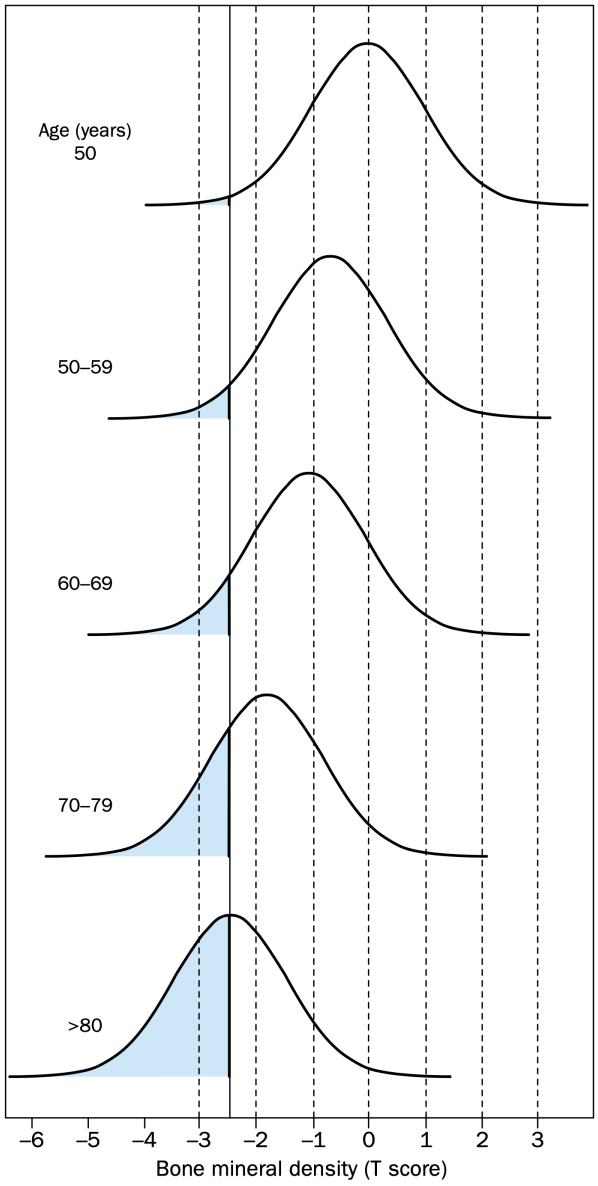

Figure 1-2: Distribution of BMD in women of different ages. The prevalence of osteoporosis is indicated by blue area under the curve. (Taken from [13])

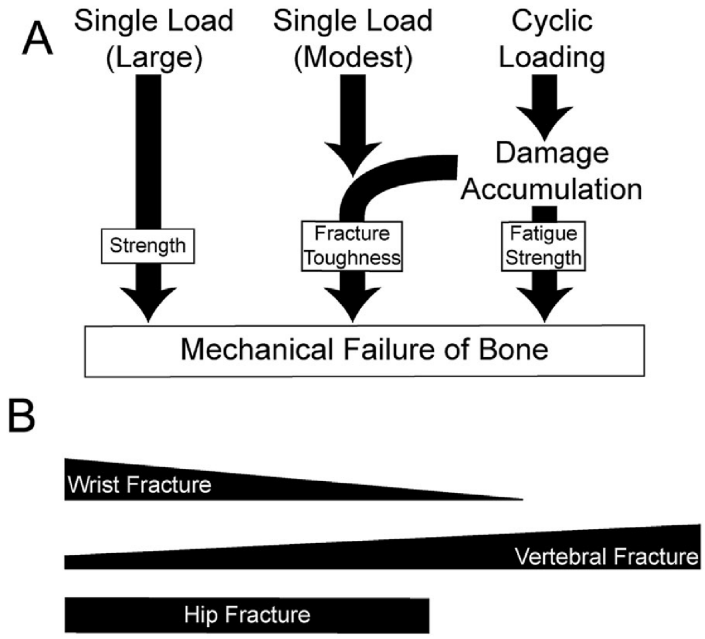

Figure 1-3: Mechanistic pathways to mechanical failure of bone. (A) Fracture may occur as a result of a single large load, a single modest load applied in the presence of preexisting tissue damage or as a result of many cycles of loading and associated damage accumulation. Each of these mechanistic pathways to mechanical failure are dominated by a different bone tissue material property (strength, fracture toughness, or fatigue strength). (B) Hypothetical representations of the relative importance of each mechanistic pathway to common osteoporosis–related fracture are shown with darkened regions. Wrist fractures occur predominately as a result of a single large load. Vertebral fractures occur predominately due to cyclic loading and less often due to a single large overload. Hip fractures are almost always associated with a single loading event but may also be associated with damage accumulation from prior overloads. (Taken from [26])

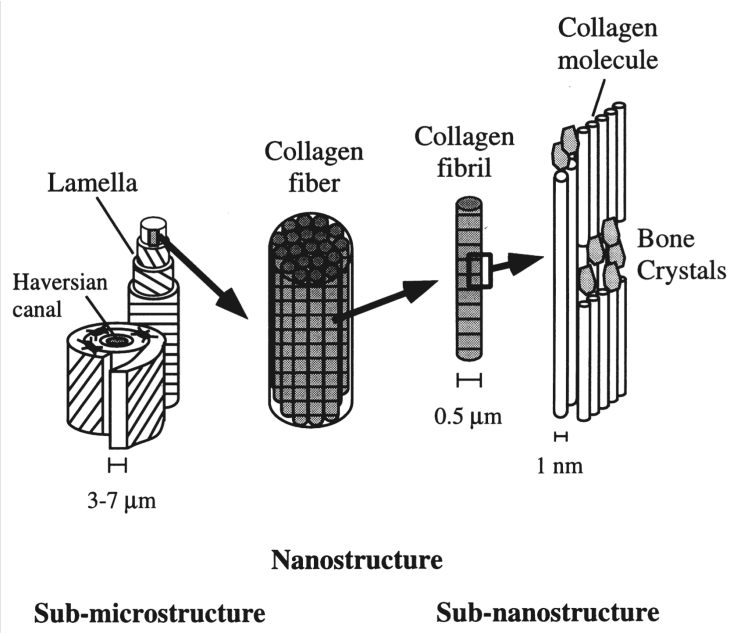

Figure 1-4: Hierarchical structure of bone tissue. Left to right: Haversian bone, lamellae, mineralized collagen fiber, collagen fibril, and collagen molecules with hole zones filled by minerialization. (Taken from [150])

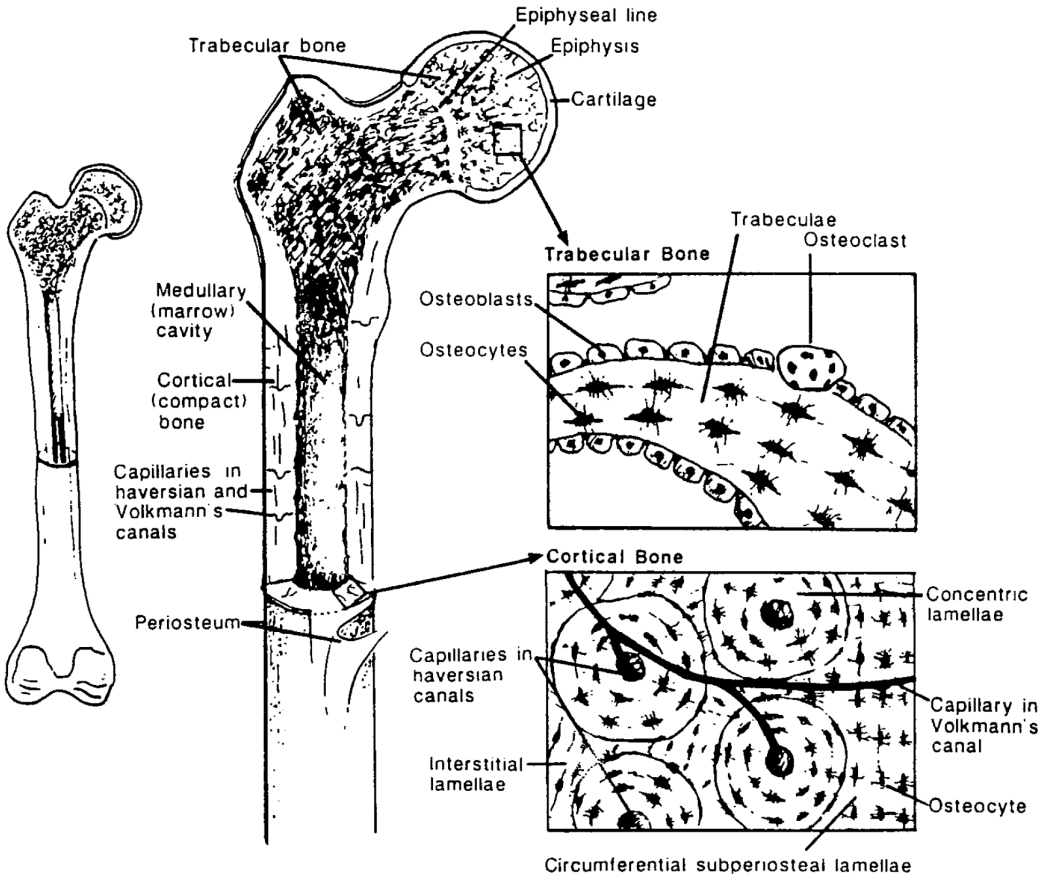

Figure 1-5: Schematic diagram of cortical and trabecular bone showing the different micro–structures. (Taken from [45])

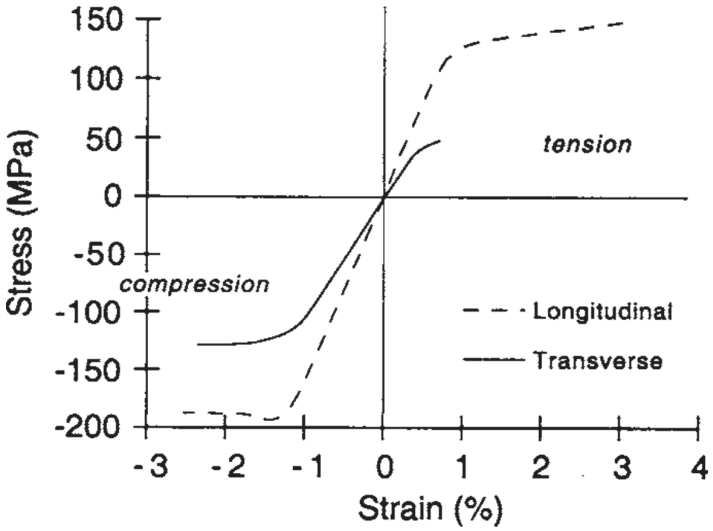

Figure 1-6: Typical stress–strain behavior for human cortical bone. The bone is stiffer in the longitudinal direction, indicative of its elastic anisotropy. It is also stronger in compression than in tension, indicative of its strength asymmetry. (Taken from [36])

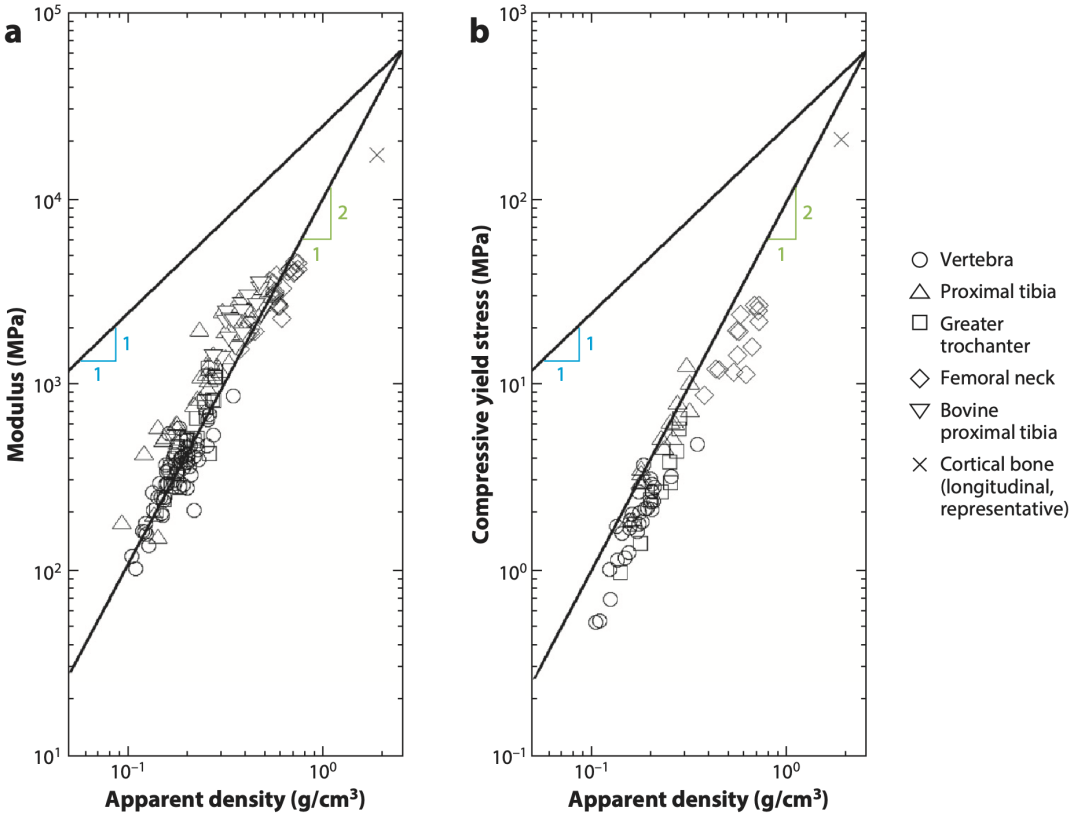

Figure 1-7: Log–log plots for (a) trabecular Young's modulus and (b) trabecular compressive yield strength as functions of trabecular apparent density. Lines indicating power–law exponents of one and two are drawn on the plots. (Taken from [5])

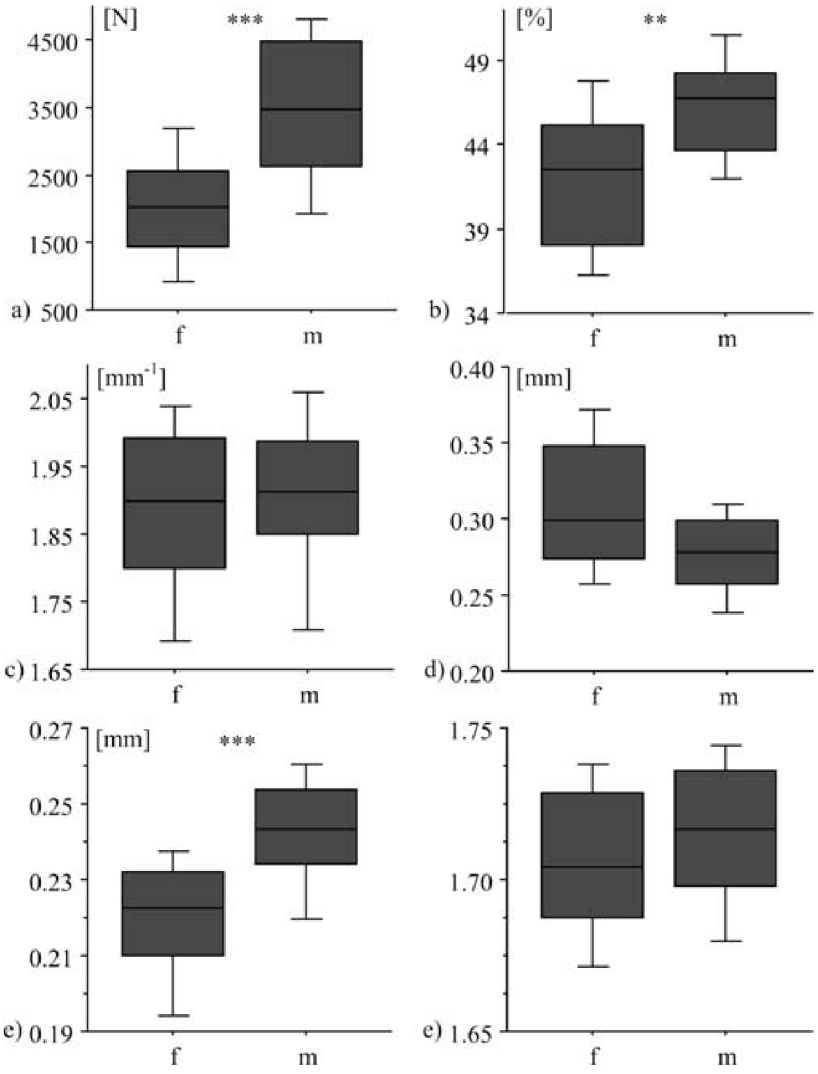

Figure 1-8: Box plots with gender differences in age–matched groups for (a) maximum failure load, (b) apparent bone volume fraction (app. BV/TV), (c) apparent trabecular number (app. Tb. N), (d) apparent trabecular separation (app. Tb.Sp), (e) apparent trabecular thickness (app. Tb.Th), and (f) fractal dimension (Frac. Dim). (* $p < 0.05$, ** $p < 0.01$, and *** $p < 0.001$). (Taken from [76])

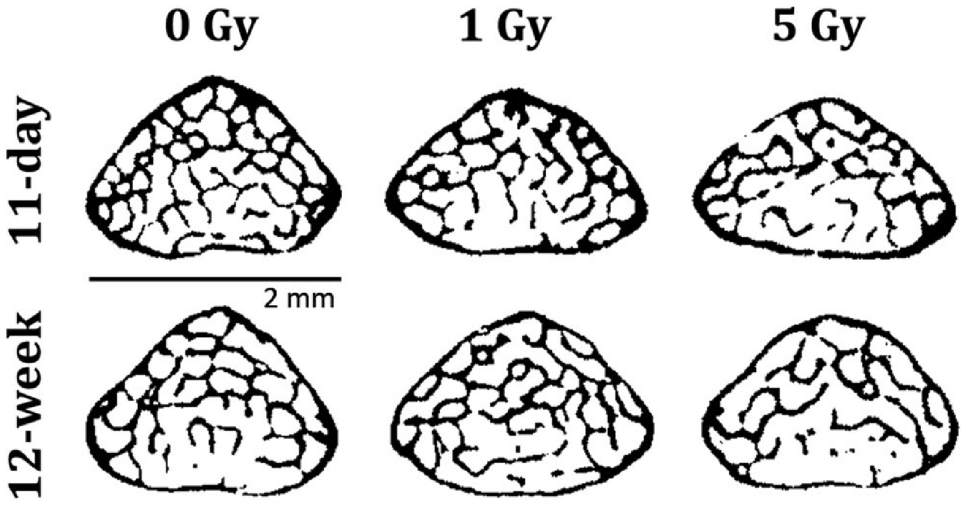

Figure 1-9: Micro–CT images of transverse cross sections from the caudal region of representative L5 mouse vertebrae, showing the effects of three different one-time radiation doses (0, 1, or 5 Gy) after 11 days or 12 weeks (all different animals). (Taken from [146])

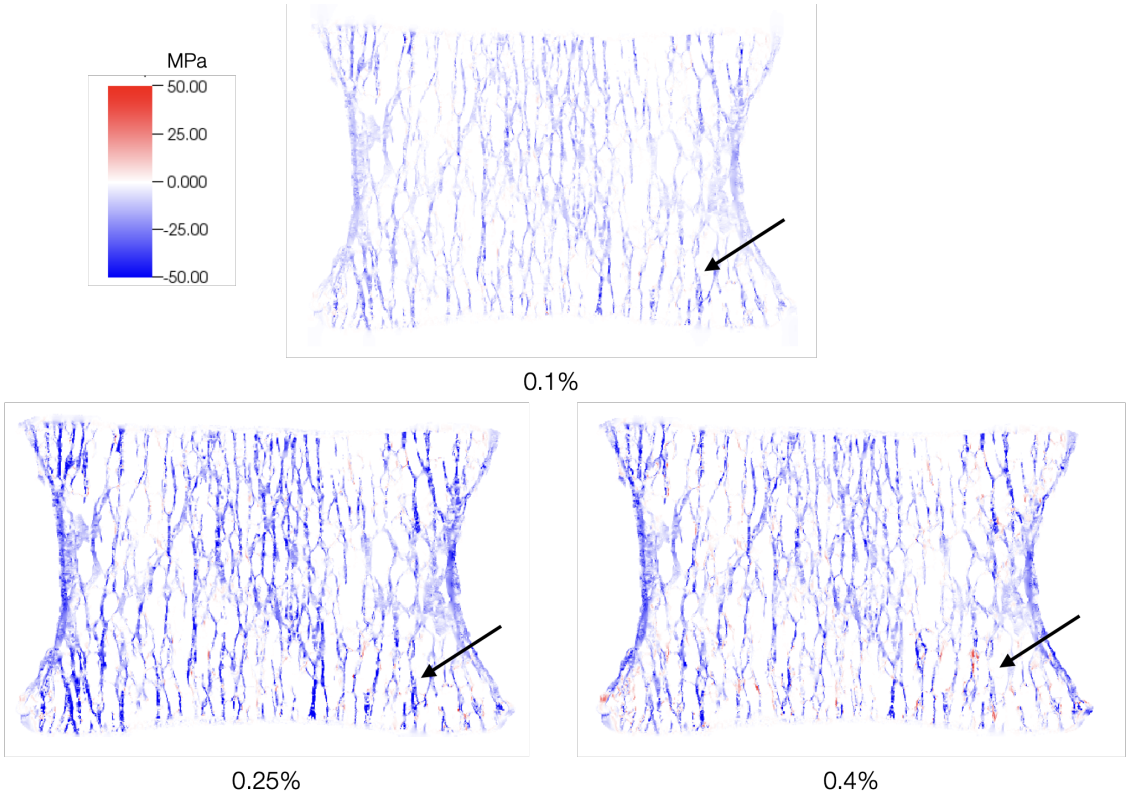

Figure 1-10: Illustration of overall non-uniform and complex stress distribution for the frontal slices within a human vertebral body specimen. Arrows point a exemplar region whose stress-state was in light compression, heavy compression and heavy tension at various levels of apparent applied compressive loading. Data presented are taken from **Chapter 4**.

Chapter 2

Structure–Function Relationship and Load–Sharing within Irradiated Murine Vertebral Body

2.1 Introduction

Numerous studies have shown that ionizing radiation can impact bone morphology, such as reducing trabecular number and connectivity, and increasing the collagen cross–linking [151, 66, 105, 104, 152, 153, 103, 102]. However, the expected corresponding adverse effects on the whole–bone stiffness or strength have not been consistently observed [115, 116, 154]. For example, 2 Gy of Fe ions irradiation could result in a 14% reduction in mouse vertebrae bone volume fraction, but not a significant reduction (around 6% reduction) in the stiffness [115]. And 5 Gy of X–ray irradiation led to a significant loss of mouse distal femur trabecular bone but not significant loss of the strength (at a latency of 6–week) [116]. One of our previous works also demonstrated that despite reduced trabecular mass (by 17.2%) and altered microarchitecture, 5 Gy of gamma–irradiation only affected the mouse vertebral strength by a minimal difference (3.3% reduction and not significant) [146]. Therefore, it is not fully understood how changes in these structural properties induced by ionizing radiation translate into changes in whole–bone mechanical behaviors or how bone can accommodate some decline in microarchitecture without a concomitant decline in stiffness or strength.

Part of the reason for this lack of understanding is that the effect of ionizing radiation on the structural–function relationship for the whole–bone, such as load–sharing and its relationship with mass–sharing, has not been studied, an issue that can be addressed by the micro–computed tomography (micro–CT) based finite element (FE) analysis. The high–spatial resolution of micro–CT data (voxel sizes on the order of 10 μm) enables the modeling of the complete morphology of

the bone tissue in three dimensions, including the spatially variable trabecular microstructure and cortex. In addition, FE models based on micro–CT data intrinsically incorporate the specimen–specific structural anisotropy and connectivity of the trabecular network, enabling robust inter– and intra–specimen comparisons [155, 156, 157, 158, 159, 160, 121]. Another key advantage of this approach is the ability to parametrically control key variables for interest; for example, by assigning the same tissue–level material properties to all specimens to isolate structural effects independent of material properties – a type of study that is not possible experimentally.

Here, we used micro-CT and mechanical testing data from a prior study [146] in which morphologic changes to mice vertebrae were induced by exposure to 5 Gy of γ–radiation to explore structure–function relationships in mouse vertebral bone. Our goal is to better understand the effect of ionizing radiation on the micromechanics of mouse vertebrae and elucidate the mechanism by which the mouse vertebrae could accommodate significant changes in trabecular morphology with a relatively small reduction in the whole–bone stiffness.

2.2 Methods

This computational study utilized data from a prior experimental study [146]. Briefly, at 17 week–of–age the C57BL/6J male mice (n = 28) were randomly divided into two groups (n = 14 per group): one group was irradiated by acute whole–body γ–radiation, absorbing a 5 Gy total dose; the other group was sham–irradiated as the control group. The group of mice exposed to ionizing radiation had significantly different L5 vertebral trabecular microarchitectural parameters compared to the control mice. There was no detectable difference in cortical thickness or whole–bone stiffness between groups (**Table 2-1**). Details of the IRB–approved ionizing radiation study are described elsewhere [146].

Based on the micro–CT data of 28 L5 vertebrae, manual contouring was performed on each thresholded micro–CT slice to segment the trabecular centrum from the cortex. Then, each voxel (10 μm isotropic resolution) was converted directly into a linear 8–noded solid finite element. At this resolution, approximately four finite elements spanned the thickness of each individual trabecula (trabecular thickness $= 40.5 \pm 1.5$ μm, mean $\pm$ S.D.), sufficient for the numerical convergence of computed tissue-level strains [161].

All bone tissue elements (i.e., those in both cortical and trabecular compartments) were assigned the same linearly elastic, isotropic, and homogeneous material properties: Young's modulus of 10 GPa [143], Poisson's ratio of 0.3. While the material properties of bone tissue may be altered by radiation [116], the same material properties were assigned to all vertebrae in both the irradiated and control group in order to isolate the effects of bone mass and microarchitecture on the whole–bone elastic behavior.

Each specimen was virtually loaded in uniaxial compression using displacement–type boundary conditions. All nodes on the cranial surface of the vertebral body were uniformly displaced to 0.5% apparent–level compressive strain. At the caudal surface, all nodes were fixed in all degrees of freedom [143]. To compare the element–wise results across specimens under the same level of apparent loading force, FEA results (including displacement–, strain–, stress–field) were linearly scaled to achieve a constant cranial reaction force of 32.5 N (comparable to the experimental failure force of 32.5 $\pm$ 5.6 N, the value was from the control group, while there is no significant difference between the control and irradiated groups.) [146].

On average, each individual finite element model comprised approximately 1.6 million elements (1.2–2.0 million elements, depending on the bone) and was solved in parallel using a supercomputing cluster (Savio Cluster; University of California, Berkeley). Each model was algorithmically partitioned into 48 domains and distributed onto two compute nodes, each with 24 cores and 64 GB of memory. Finite element problems were then solved using a Krylov Subspace iterative linear solver (Finite Element Analysis Program 8.3; University of California, Berkeley), consuming a total of 648 CPU hours for all samples.

To assess whether the radiation–induced morphologic changes preferentially affected the mechanical behavior of the cortical or trabecular compartment, the total internal axial (vertically oriented) force was compared between cortical and trabecular compartments at each slice. Total internal axial force in each compartment was defined as the summation of axial stresses of all elements within that compartment at each slice multiplied by the total cross–sectional area of the bone tissue in that slice (100 $\mu m^2 \times$ number of elements).

Based on the vertical internal force in the cortical and trabecular compartments, the trabecular load fraction was calculated as a function of axial position within the vertebral body. To quantify the axial position within the vertebral body, each vertebral body was evenly split into ten axial sections, where each axial section contained several vertical slices (depending on the height of the sample). Trabecular load fraction was calculated as the internal force in the trabecular compartment divided by the total internal force (trabecular plus cortical) and was computed at each axial section (cortical load fraction = 1 – trabecular load fraction) [128]. Similarly, the trabecular mass fraction was quantified as the number of voxels in the trabecular compartment (i.e., absolute trabecular tissue mass, thereby assuming a uniform mineral density of $2.0\ g/cm^3$ [160]) divided by the total number of voxels, and was also computed at each axial section. Comparisons between the control and treatment groups were assessed at each axial position in the vertebral body (cranial–to–caudal).

To study the spatial distribution of initial failure tissue distribution, we defined principal stress thresholds of 33 MPa in tension, and 81 MPa in compression, based on tension/compression yield strain asymmetry [162]. Any element in which the principal stresses exceeded these thresholds in

either tension or compression was classified as 'initially–failed tissue'. A pilot study showed the tissue modulus has no effect on the initially–failed tissue distribution due to the constant reaction force of all samples by the linear scaling operation. The volume and compartmental distribution of initially–failed tissue were compared between groups.

The primary outcomes of this analysis were the absolute trabecular and cortical tissue masses, load– and mass–sharing measures, and the initially–failed tissue distribution. Unpaired t–tests were used to compare absolute trabecular and cortical tissue masses as well as load– and mass–sharing outcomes between two groups, independently for each axial section in the vertebral body. A mixed–effects linear regression model was used to test for a relationship between trabecular mass fraction (independent variable) and trabecular load fraction (dependent variable), including the consideration of multiple observations from the same vertebral body. An interaction term was also included in the model to assess whether the relationship between load fraction and mass fraction depended on treatment. Unpaired t–tests were also used to compare the initially–failed tissue compartmental distribution.

Statistical analyses were conducted in JMP Pro (16.0), and two–sided $p < 0.05$ was considered statistically significant.

2.3 Results

Irradiation significantly reduced trabecular mass fraction and, correspondingly, the load fraction, while the load–sharing in the mouse vertebra occurred primarily via the cortex (typically $> 50\%$ and up to 83% cortical load fraction). Absolute trabecular tissue mass was significantly lower in the irradiated versus control group at all axial cross–sections in the vertebral body ($p < 0.03$, depending on location, **Figure 2-1**A), whereas the cortical tissue mass was not altered ($p > 0.11$, **Figure 2-1**B). As a result, the trabecular mass fraction was lower in the irradiated versus control group, both on average in the whole bone (-12.8% difference, $p < 0.002$) and at almost all axial cross–sections in the vertebral body (**Figure 2-1**C–D). Similarly, the trabecular load fraction was also lower in the irradiated versus control group, both on average (-21% difference, $p < 0.0001$) and at each axial cross–section ($p < 0.015$, depending on location, **Figure 2-1**E–F). In addition, for both the control and irradiated group, there was a significant difference between the mass fraction and load fraction (positive difference in the trabecular and negative difference in the cortical compartment) at almost all axial sections (**Figure 2-1**G-H).

There was evidence that irradiation altered the structure–function relationship in the vertebral body. Results from the regression analysis demonstrated that the trabecular load faction was significantly associated with the trabecular mass fraction ($R^2 = 0.92, p < 0.0001$, **Figure 2-2**). There was a statistically significant interaction between trabecular mass fraction and treatment ($p < 0.03$), indicating that the relationship between mass fraction and load fraction was altered by

radiation (an 8% decrease in the slope).

For both control and treatment groups, the initially–failed tissue occurred primarily in the cortical compartment (**Figure 2-3**, **Figure 2-4**). The irradiated group had more initially–failed tissue than the control group ($p = 0.035$), and this difference was attributed primarily to differences in initially–failed cortical tissue. In the control group, there were only 9.5% initially–failed cortical tissue, compared to 13.3% in the treatment group ($p < 0.01$, **Figure 2-3**A). The initially–failed trabecular tissue was not different between groups ($p = 0.88$, **Figure 2-3**B). Considering the whole bone (trabecular plus cortical), there was 3.9% more initially–failed tissue than the control group (12.7% versus 16.6%, $p = 0.035$, **Figure 2-3**C).

2.4 Discussion

Following irradiation, there was a reduction in trabecular mass fraction and in trabecular load fraction as the trabecular mass fraction was controlled. Together, these reductions resulted in a shift of the axial load from the trabecular centrum into the cortex. Thus, because the cortical structure was not measurably diminished by radiation exposure, the whole–bone stiffness showed a relatively small and not significant difference between the control and irradiated groups.

Our study provided novel mechanistic explanations for the effect of ionizing radiation on bone morphology and the corresponding effect on the whole–bone mechanical behavior. Previous studies have demonstrated that ionizing radiation preferentially affects the trabecular compartment relative to the cortical compartment in mice vertebral bodies or femurs, but that whole–bone stiffness is not necessarily directly impacted by ionizing radiation [112, 163, 164, 115, 151, 165]. Meanwhile, the whole–bone mechanical properties such as stiffness and strength were known to be inherently and strongly associated with bone mass, microarchitecture, and tissue–level material properties [166, 167, 35, 168, 87, 169, 117, 148]. To partially explain such inconsistency, we revealed that the whole–bone elastic property can be maintained following a shift of axial compressive loading to the cortex, which could be attributed to a reduction of trabecular mass fraction and altered structure–function relationship (i.e., a lower trabecular load fraction as the trabecular mass fraction was controlled) following ionizing radiation.

The protective effect of the cortex on the whole–bone stiffness may be distinct for the murine vertebrae and human vertebrae. While both murine and human vertebrae exhibit a similar U–shaped trend in cortical–trabecular load–sharing as a function of axial position [128]. There are inherent structural characteristic differences between them. For example, the cortex is the dominant structural compartment for resisting axial loads in mice vertebrae, but the trabecular centrum is the dominant structural compartment in human lumbar vertebrae [63, 129, 160, 127]. Meanwhile, the preferential effects of ionizing radiation on the trabecular compartment relative to the cortical compartment have been suggested to be attributed to the larger trabecular cellular surface

area exposed to radiation [102, 170, 109, 171]. Therefore, ionizing radiation may also preferentially affect the trabecular compartment in human vertebrae, as human vertebrae also have a much larger trabecular cellular surface area relative to the cortical shell [148]. Together, for a human vertebral body, if the trabecular mass loss, microarchitecture degradation, and structure–function relationship alteration were introduced by ionizing radiation, the thin cortical shell may not generate a protective effect on the whole–bone stiffness.

One of the limitations of this work was assigning identical bone tissue–level properties in the FE model for both control and irradiated groups. Studies have shown that ionizing radiation can increase the amount of collagen cross–linking in the bone tissue [172, 173, 147]. However, such an increase in collagen cross–linking could manifest in loss of bone strength or bone toughness [116], but not elastic properties (i.e., stiffness) [66]. Assigning the identical bone tissue modulus in both control and treatment groups enabled us to isolate the effect of irradiation on the structure–function relationship of the mouse vertebral body, such as the correlation between the trabecular mass fraction and trabecular load fraction, without involving the compounded effects of irradiation on both bone microarchitecture and bone tissue properties.

Another limitation of this work was the linearity in the FE analysis. Without nonlinear large–deformation and material failure properties, our results were limited to initially-failed tissue distribution using a principal stress failure criterion of bone tissue. However, we observed that the overall proportion of initially–failed tissue was significantly higher in the irradiated group than in the control group when the vertebral body was under the same level of axial compressive loading. Such change was attributed to a higher proportion of initially–failed tissue in the cortical (due to more load–sharing) and an unchanged proportion of initially–failed tissue in the trabecular compartment (even with less load–sharing). Therefore, such altered initially–failed tissue distribution implied that the failure mechanism may be altered by ionizing radiation without computationally expensive nonlinear FE analysis. Meanwhile, it also suggested that the protective effects of the cortex on the whole–bone stiffness may not be extrapolated to a similar protective effect on the whole–bone failure behavior.

In summary, we found how ionizing radiation could alter the structure–function relationship and load–sharing within the mouse vertebral body, and the protective effect of the cortex on the trabecular centrum in terms of the whole–bone level stiffness. Together, these findings provided a mechanism by which relatively large effects of ionizing radiation on vertebral morphology translated into relatively small effects on vertebral elastic behaviors in a murine model.

Table 2-1: Microarchitectural measurements and computational stiffness data (mean $\pm$ S.D.) for control and irradiated groups. p-value was from the t-test between two groups, bold indicated statistical significance. The percentage difference was calculated relative to the control group. N = 14, 13 for control, irradiated groups, respectively.

Parameters	11-day, 0 Gy (control)	11-day, 5Gy (% difference)	p-value
Tb.BV/TV (%)	19.9 ± 0.03	-22.3	**0.000**
Tb.Sp (mm)	0.19 ± 0.02	16.1	**0.000**
Tb.SMI	0.75 ± 0.21	107.5	**0.000**
Tb.Conn.D ($1/mm^3$)	268 ± 35	-17.0	**0.001**
Tb.N ($1/mm$)	5.05 ± 0.43	-11.8	**0.000**
Tb.Th (mm)	0.04 ± 0.001	5.4	**0.001**
Ct.Th (mm)	0.05 ± 0.006	0.5	0.91
Vertebral Stiffness (N/mm)	2185 ± 225	-6.4	0.07

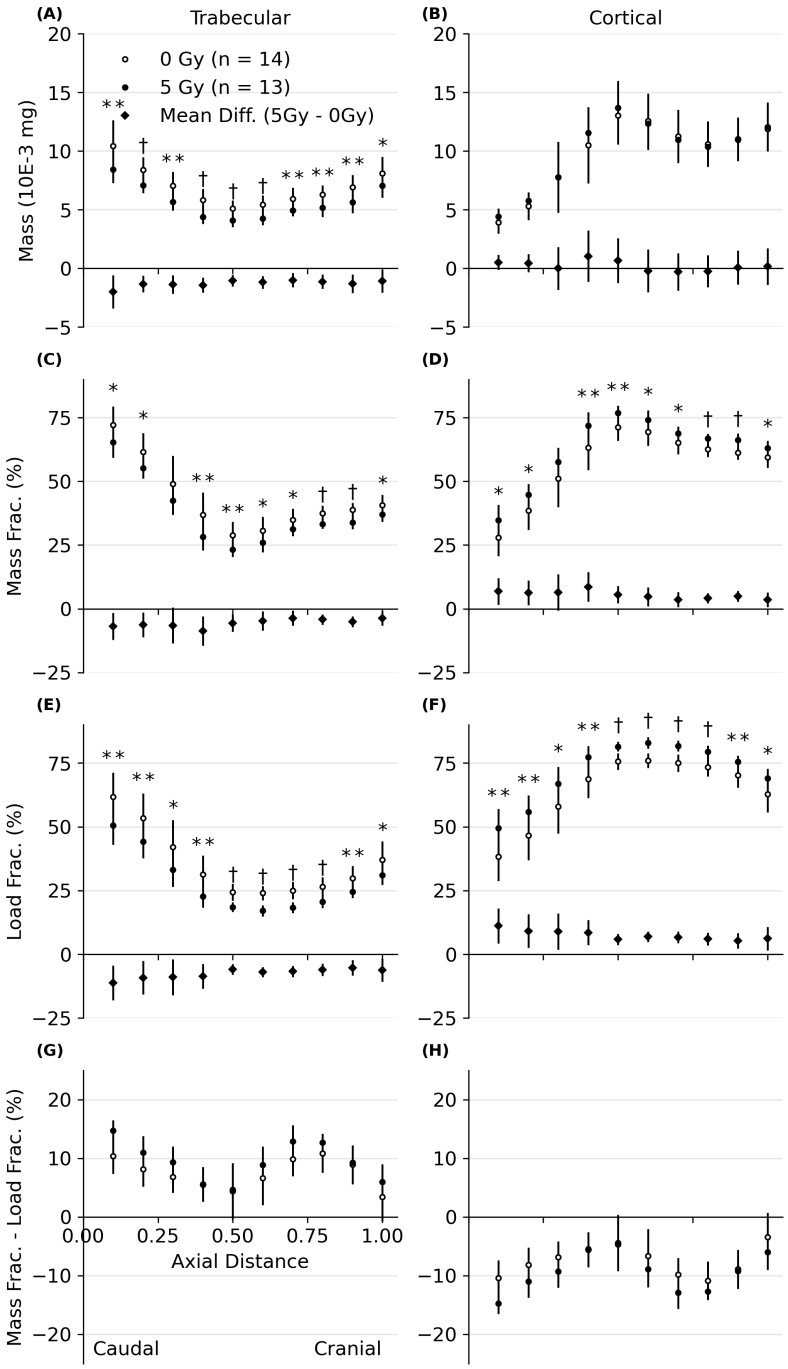

Figure 2-1: A – F: Absolute trabecular (left column) and cortical (right column) bone mass, mass fraction, load fraction, and difference between mass fraction and load fraction as functions of axial position in the vertebral body. Data are shown as mean $\pm$ SD. $* : p < 0.05, ** : p < 0.01, \dagger : p < 0.001$. G – H: no t–test between groups performed.

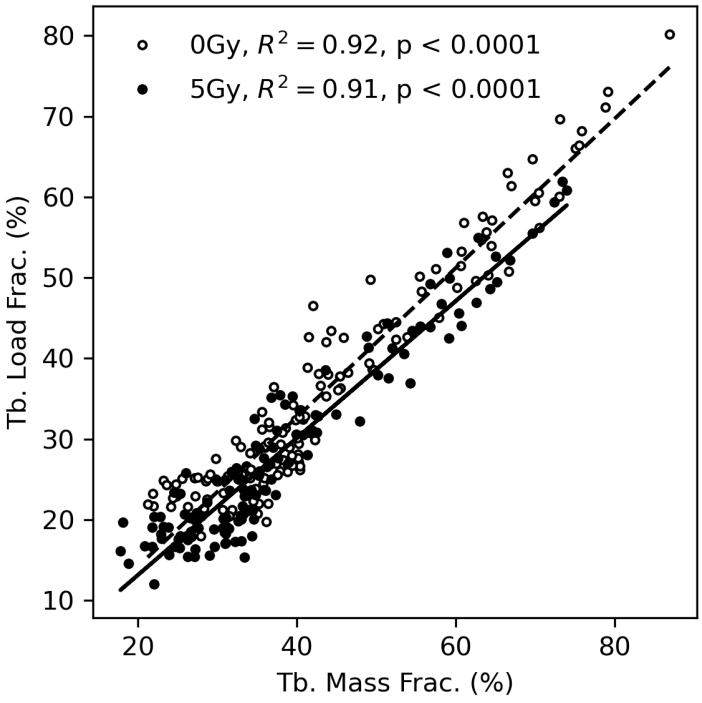

Figure 2-2: Scatter plot showing the independent relationships between trabecular mass fraction and load fraction from the control (n = 14 $\times$ 10, number of specimens $\times$ ten axial sections per specimen) and treatment group (n = 13 $\times$ 10). R^2 and p–values are as shown from univariate linear regression. A mixed–effects linear regression model with an interaction term demonstrated a statistically significant interaction between groups ($p < 0.03$).

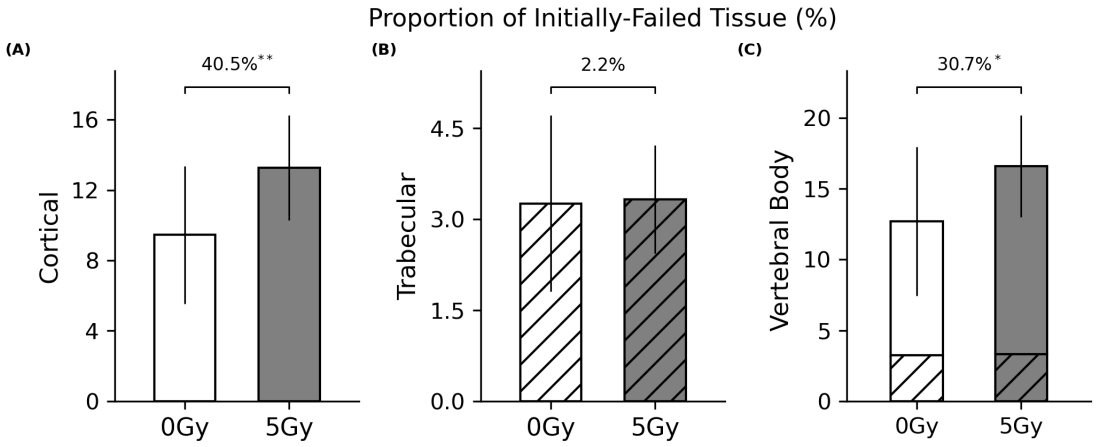

Figure 2-3: Mean $\pm$ SD initially–failed tissue volume in the (A) cortical compartment (B) trabecular compartment and (C) whole vertebral body for control and treatment groups. The initially–failed tissue volume was calculated for each specimen on a relative basis by normalizing the initially–failed tissue volume by the total bone volume of that specimen. Cross-hatching in the vertebral body initially–failed tissue volume indicated a direct comparison between the trabecular (hatched) and cortical (un–hatched) compartment. Percent differences were calculated relative to the control group. $* : p < 0.05, ** : p < 0.01$.

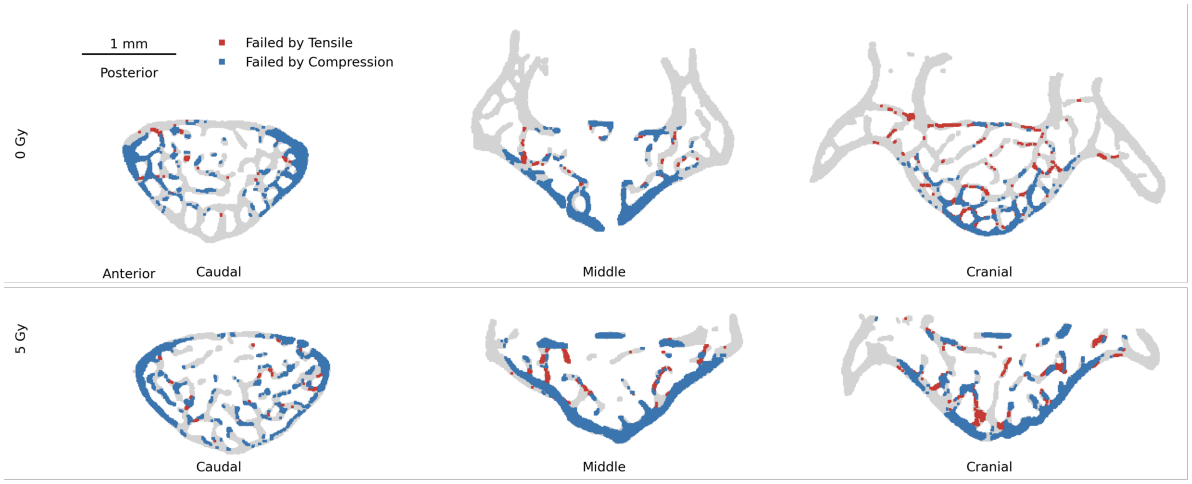

Figure 2-4: Representative distribution of initially–failed tissue in tension (red) and compression (blue) at three locations in the vertebral body for the control (upper row) and treatment group (lower row). The caudal, middle, and cranial locations were defined at 10%, 50%, and 90% of the vertebral body height, respectively.

Chapter 3

Distinct Changes in Bone Stiffness and Strength in Irradiated Murine Vertebral Body

3.1 Introduction

Ionizing radiation exposure, either from clinical radiation therapy targeting malignant tumors or from long–term space travel in a cosmic environment, has been shown to negatively affect bone stiffness, strength, and fatigue life in both animal models and clinical studies [102, 104, 105, 106]. The effect of ionizing radiation on bone mechanical properties has been observed and associated with the combination of changes in bone porosity, microarchitecture, and tissue–level material properties [113, 108, 165, 174, 146]. However, while previous animal studies showed consistent changes in bone mass and trabecular microarchitecture induced by irradiation but controversial results in whole–bone strength [115, 116, 175, 146]. Numerous clinical data–based studies confirmed a significant increase in clinical fracture risk following radiation therapy at multiple anatomic sites, including pelvic and rib [105, 107]. Therefore, it is of both scientific and clinical interest to understand how changes in bone mass and microarchitecture induced by irradiation mechanistically manifest into changes in bone strength and fracture risk.

It is established that the whole–bone stiffness is associated with bone mass and bone microarchitecture, and the whole–bone strength is strongly correlated with the whole–bone stiffness [57, 31, 5, 42]. Meanwhile, the whole–bone strength is also mechanistically related to the bone failure mechanism [26, 63]. For example, previous studies have demonstrated that the initial failure tissue was localized at the endplates within the human vertebral body, which implied a weak–link of the load-bearing capacity [129]. And there were multiple failure modes – by axial compression, bending, or buckling – in the human trabecular bone [176, 177]. Moreover, the structural redundancy

may play a role in the whole–bone failure process and bone fragility [149]. However, it is unclear whether the bone failure mechanism could be altered by ionizing radiation. If so, the loss of bone strength could be more prominent than the loss of bone stiffness following irradiation through an independent pathway. Thus, such investigation is able to provide novel mechanistic understandings of the effect of ionizing radiation on bone fracture risk. In addition, it may also bring insights into bone aging and osteoporosis–related drug treatment studies where the changes in bone fracture risk were primarily attributed to changes in bone mass, bone microarchitecture [68, 85, 82, 178, 179], and possibly changes in the bone failure mechanism.

Thus, in this work, we use micro–computed tomography (micro–CT) data from a prior experimental study [146], combined with nonlinear finite element (FE) analysis, to explore the effect of ionizing radiation on the failure mechanism in the mouse vertebrae.

3.2 Methods

Micro–CT data from twenty–eight skeletally mature C57BL/6J male mice (Jackson Labs West, Sacramento, CA) were included in this study. Details of the IRB–approved ionizing radiation study and specimen preparations (upon which the micro–CT data used here are based) are described in detail elsewhere [146]. Briefly, after randomization, the treatment group (N = 14) received 5 Gy of whole–body of γ–radiation, while the control group (N = 14) was sham–irradiated. On the 11th day after irradiation, both groups were humanly sacrificed. All mice L4 and L5 vertebral bodies were included in this study.

After acquiring the binary micro–CT images (resolution of $10\mu m$) for each mouse L4 and L5 vertebral body, computation models were constructed. Firstly, each micro–CT image was manually segmented into trabecular and cortical compartments. Then, each specimen's micro–CT images were converted into a 3D volume using a customized IDL code [128]. At last, each 10 μm voxel in the mouse vertebral body volume was converted to an 8–noded cube finite element using a customed C++ code [128].

All bone tissue elements were assigned the identical fully ductile [180], rate–independent elasto–plasticity [181], and homogeneous properties: Young's modulus of 5.4 GPa [146]; Poisson's ratio of 0.3; tissue–level tensile and compressive yield strains of 0.33% and 0.81% [118], respectively. Each mouse vertebral body was axially loaded to 2% compressive apparent strain with all degree–of–freedom (DOF) fixed within the caudal surfaces and displacement–type boundary condition applied on the cranial surface. Both geometrical and material nonlinearity were included in the finite element analysis using an implicit, parallel framework [144, 117]. On average, each mouse vertebral body consisted of 1.5 million elements (1.1 – 2.0 million) and 6.0 million DOFs (4.4 – 7.7 million). All analyses were implemented on the Stampede2 supercomputer (Texas Advanced Computing Center, The University of Texas at Austin, TX, U.S.A.) with

48 computing cores. The total computing recourse required for 54 nonlinear analyses was about 1500 CPU–hours.

The mouse vertebral body whole–bone level computational stiffness and strength were derived from the force–deformation curve. The deformation was evaluated directly as the displacement of boundary condition, whereas the force – the reaction force on the cranial surface – was evaluated by summation of axial direction stress multiplying by the corresponding surface area of each element (100 μm^2) on the cranial surface. Both deformation and force were evaluated at 20 equally spaced sub–steps in the nonlinear analysis. The stiffness was then defined as the slope of the line between the origin and the first sub–step (at 0.2% apparent strain) on the force–deformation curve. And the strength was defined as the reaction force at 2% compressive apparent strain.

At 2% apparent compressive strain, failure–related computational outcomes were evaluated within trabecular and cortical compartments. Trabecular failure tissue was defined as the volume of trabecular tissue with strain beyond the yield strain in the trabecular compartment. Likewise, we could define cortical failure tissue. Vertebral body failure tissue was the summation of trabecular and cortical failure tissue. Moreover, to study the failure process as a function of the applied load. Trabecular failure tissue and cortical failure tissue were also evaluated at five equal–distance sub–steps (0.4%, 0.8%, 1.2%, 1.6% and 2% apparent strain) in the nonlinear analysis.

Computational stiffness, strength, and failure–related outcomes at 2% apparent strain – vertebral body, trabecular, and cortical failure tissue – were compared between the control and treatment groups using the unpaired t–test. At five equal–distant sub–steps in the nonlinear analysis, trabecular and cortical failure tissue were compared between the control and treatment groups using the unpaired t–test. Additionally, trabecular failure tissue and cortical failure tissue were compared in each group using the unpaired t–test.

The first multivariate regression model was used to study the relationship between the vertebral body stiffness, treatment (as independent variables), and strength (as the dependent variable), including the interaction term between stiffness and treatment. If the correlation between the vertebral body stiffness and strength was significant, we defined the vertebral body strength offset as the vertebral strength minus the regression linear factor multiplying vertebral stiffness, which represented the portion of vertebral strength that was not correlated with (or explained by) the vertebral stiffness (**Figure 3-2**). Then, a second multivariate regression model was used to study the relationship between vertebral body failure tissue, treatment (as independent variables), and strength offset (as the dependent variable), including the interaction term between vertebral body failure tissue and treatment.

All statistical analysis was in JMP Pro (Ver 16.0), with a significant level at $p < 0.05$.

3.3 Results

Both vertebral body stiffness and strength were lower in the treatment group than in the control group. Following irradiation, the mouse vertebral body had 7.4% lower stiffness ($p = 0.0054$) and 8.8% lower strength ($p = 0.0002$) compared to the control group.

Irradiation affected the vertebral body strength independent of the effect on the vertebral body stiffness; such independent effect could be attributed to the vertebral body failure tissue. Vertebral body strength showed a strong correlation with vertebral body stiffness in the control group ($R^2 = 0.76, p < 0.0001$) and in the treatment group ($R^2 = 0.43, p = 0.0003$, **Figure 3-1**). The effect of treatment on the strength was significant including ($p = 0.014$) or excluding ($p = 0.011$) the interaction term between treatment and stiffness in the regression model (interaction term $p = 0.95$). With the same level of vertebral body stiffness, irradiated mouse vertebral body had a lower level of strength than the control group, where the intercept offset was 0.48 N, which was 29% of the total strength difference between two groups. The strength offset was highly and linearly correlated with the vertebral body failure tissue ($R^2 = 0.84, p < 0.0001$, **Figure 3-3**). Additionally, the effect of treatment ($p = 0.90$) or the interaction term between treatment and vertebral body failure tissue ($p = 0.61$) in the regression model was not significant.

Irradiation affected the trabecular failure tissue but not cortical failure tissue, resulting in less vertebral body failure tissue in the treatment group than in the control group (**Figure 3-4**). Following irradiation, trabecular failure tissue showed a 22.8% lower value in the treatment group ($p < 0.0001$), while cortical failure tissue showed a trend of 5.3% increase in the treatment group ($p = 0.15$). Together, the irradiated vertebral body showed a 6% less volume of vertebral body failure tissue than the control group ($p = 0.036$).

For all loading stages other than the initial one (0.4% apparent strain), there was more cortical failure tissue than trabecular failure tissue in the control group (max $p < 0.0001$, depending on loading stage), such difference was accentuated by the treatment and was attributed to a lower trabecular failure tissue (max $p < 0.0001$, depends on loading stage, **Figure 3-5**). By contrast, at the initial loading stage (0.4% apparent strain), there was more trabecular failure tissue than cortical failure tissue in the control group ($p = 0.0005$), and such difference was no longer observable in the irradiated group ($p = 0.53$).

3.4 Discussion

Our results suggested that ionizing radiation affected bone failure properties (strength) more than bone elastic properties (stiffness) by altering the amount of failure tissue in the trabecular compartment in the mouse vertebral body. Our previous results indicated that ionizing radiation preferentially negatively impacts the trabecular mass and microarchitecture but not the cortical mass

or cortical thickness [146]. In this work, we found that there were about 23% less trabecular failure tissue following irradiation, whereas the cortical failure tissue showed no observable change. Together, the mouse vertebral body (i.e., trabecular plus cortical) failure tissue was significantly lower by 6% in the irradiated group than in the control group. Furthermore, vertebral body failure tissue was found to be highly correlated with the strength offset, which quantified the effect of ionizing radiation on the strength independent of the effect on the stiffness. Thus, we concluded that ionizing radiation affected mouse vertebral body strength (about 9 %) more than stiffness (about 7%) by affecting the trabecular failure tissue.

We found that the ratio between trabecular and cortical failure tissue was consistent during the whole–bone failure process for both groups and was altered by ionizing radiation. For the initial loading stage (0.4% apparent strain), we observed an increased cortical failure tissue and unchanged trabecular failure tissue following irradiation. This result was consistent with our previous linear computational study based only on the L5 specimens since 0.4% apparent strain was in the linear region of the whole–bone force–deformation curve. By contrast, for loading stages later than the initial one ($>$ 0.4% apparent strain), the trabecular failure tissue was around 37 – 38% of the vertebral failure tissue and ionizing radiation decreased this ratio to about 30%. Such effect was attributed to the lower trabecular failure tissue and unchanged cortical failure tissue. Together, these results suggested that ionizing radiation consistently affected the vertebral body failure mechanism during the entire whole–bone failure process by decreasing the trabecular failure tissue.

Previous studies have demonstrated that ionizing radiation could affect bone strength in the small animal models from biomechanical testing or clinical observations, which are consistent with our results [115, 116, 147, 105]. Some studies also had efforts attributing such effect either to a higher level of stress in the trabecular compartment following irradiation using linear FE analysis [115]), or a reduction of bone tissue ductility following irradiation by optimizing the material properties in a nonlinear FE model [116]. In addition to those findings, our study provided a mechanistic explanation for the distinct effects of ionizing radiation on bone stiffness and strength, namely, ionizing radiation affected bone strength independent of affecting bone stiffness by decreasing the volume of bone failure tissue in the whole–bone failure process.

Our nonlinear computational results provided insights into the different effect sizes of the trabecular mass and microarchitecture versus the bone strength induced by irradiation. Previous studies reported that the cortical mass and thickness were not altered by irradiation [146]. Meanwhile, our result showed that cortical failure tissue was the majority portion of the vertebral body failure tissue in the post–yielding loading stages ($>$ 0.4% apparent strain). Therefore, the cortex may provide a protective role on the whole–bone strength as the trabecular bone mass and microarchitecture were negatively affected by irradiation, which was an analogy to our previous work (**Chapter 2**). Thus, for the mouse vertebral body, the cortex played a dominant and protective

role in both bone stiffness and strength due to a dominant role in mass fraction. Such a mechanism may also partially explain some previous observations. For example, it was reported that ionizing radiation altered the trabecular bone mass and microarchitecture but not cortical bone or the whole–bone strength in mouse tibia or femur [163, 112]. Since the difference between cortical and trabecular mass in mouse tibia and femur was more evident than the vertebrae [182].

One strength of this study was using nonlinear FE analysis to illustrate the effect of ionizing radiation on the failure mechanism of the murine vertebral body, which has not been reported to our knowledge. Compared to the linear FE analysis, which could only evaluate high–stress distribution to imply the initial failure location of the bone tissue [115, 129], a nonlinear analysis could track actual failure tissue location and mode (i.e., in tension or compression) [63, 176]. Our cortical and trabecular failure tissue results have shown to be very different in the initial loading stage than in the failure loading stage. More than half of the failure tissue was in the trabecular compartment at the initial loading stage. However, that ratio dropped to around 30% (in the irradiated group) at the post–yielding stages. Such findings would be impossible to observe in a linear analysis setting and were a necessity to explain the mechanism by which ionizing radiation affected the whole–bone strength.

One of the limitations of our study was assigning identical elasto–plasticity tissue properties for both control and irradiated groups. Evidence showed that ionizing radiation could decrease bone tissue–level ductility by increasing the collagen crosslink [172, 173, 147]. Meanwhile, studies using the human vertebral body reported that one SD decrease in tissue–level ductility was associated with a 7% decrease in the whole–bone strength [125]. In this work, our nonlinear FE analysis derived strength result did not incorporate the tissue-ductility and changes in tissue-ductility by ionizing radiation. However, with consideration of the reduced tissue–level ductility following irradiation, the strength of both groups would be lower [116]; while the strength of the irradiated group would decrease more than the control group. As a result, the tissue–level ductility would only accentuate the strength difference between the control and irradiated group. More importantly, by assigning the identical bone tissue material properties, our study revealed the effect of ionizing radiation on the vertebral failure mechanism associated with the changes in bone morphology only, but not a compounding effect involving changes in bone material proprieties.

Another limitation in our study was that the relationship between the effect of ionizing radiation on bone morphology and strength might not be well extrapolated into the human vertebral body case. For example, studies have shown that the mass– and load–sharing was dominated by the cortex in the mouse vertebral body (**Chapter 2**) whereas by the trabecular centrum in the human vertebral body [128], which implied that the protective effect of the cortex on the trabecular centrum in terms of the elastic and failure properties may not be observed in human vertebrae following irradiation. However, the principle that ionizing radiation affected bone strength independent of the effect on bone stiffness may still apply in the human vertebrae.

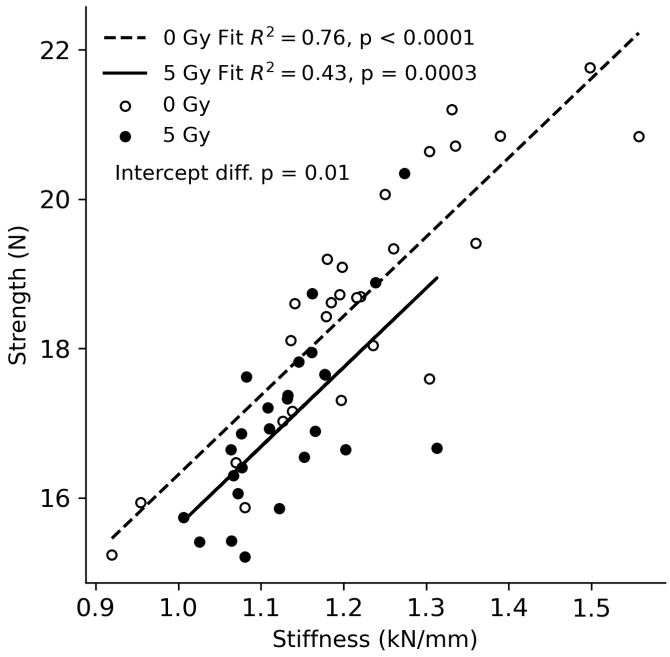

Figure 3-1: Scatter plot of the vertebral body stiffness and strength for both control (N = 27) and treatment (N = 26) groups. R^2 and p–value were for linear regression of the control and irradiated group separately. Multivariate regression model was use to study the effect of treatment on the strength independent of the effect on stiffness, with p–value = 0.01. The difference of intercept was 0.48 N, which was 29% of the difference of strength between two groups, and 2.6% of the mean strength of the control group.

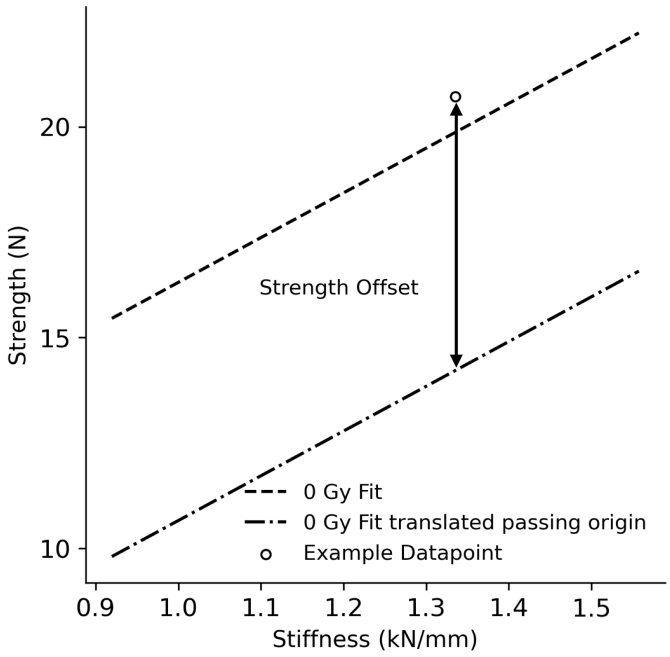

Figure 3-2: Definition of the strength offset was derived from the correlation between vertebral stiffness and strength. Strength offset, as shown, was the vertical distance between a mouse vertebral strength to the translated regression line of that group, which passed the origin. The physical interpretation was the portion of vertebral strength that was not correlated with the vertebral stiffness.

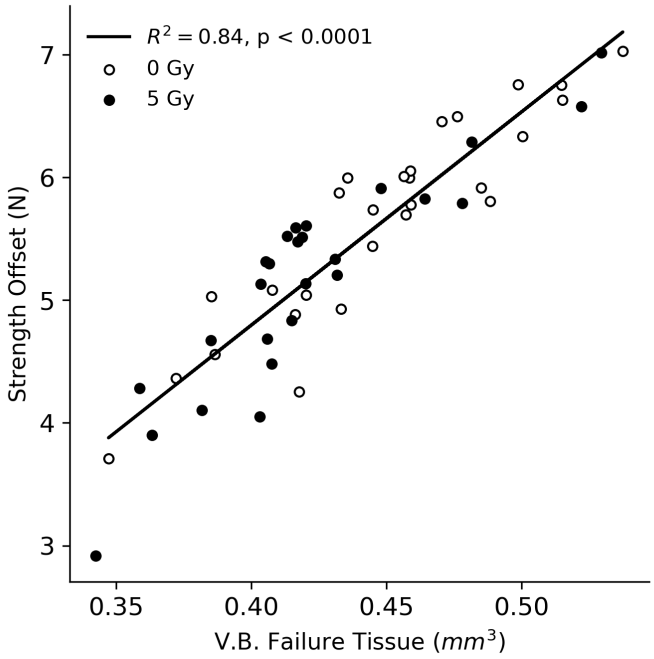

Figure 3-3: Scatter plot of the vertebral body strength offset and vertebral body failure tissue for both control (N = 27) and treatment (N = 26) groups. R^2 and p–value were for linear regression of the control and irradiated group pooled.

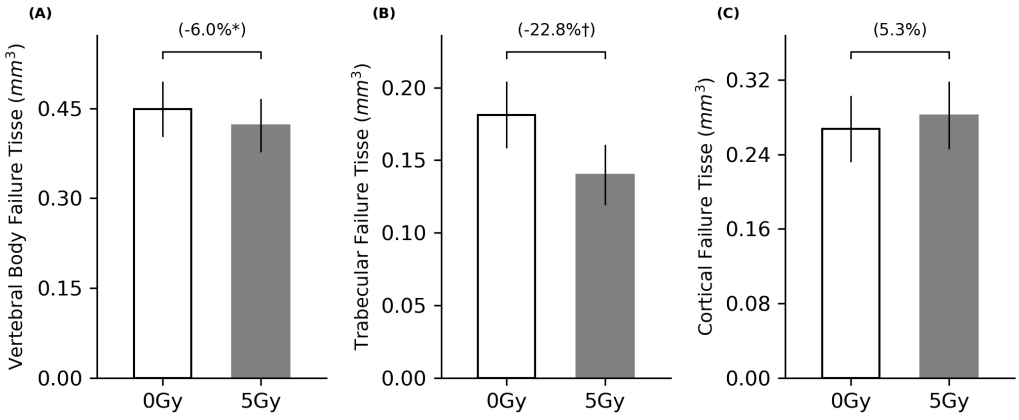

Figure 3-4: Mean $\pm$ SD vertebral body, trabecular, and cortical failure tissue for control and irradiated group. Difference in percentage is from irradiated group minus control group. N = 27 for control group, and N = 26 for irradiated group $(* : p < 0.05, \dagger : p < 0.001)$.

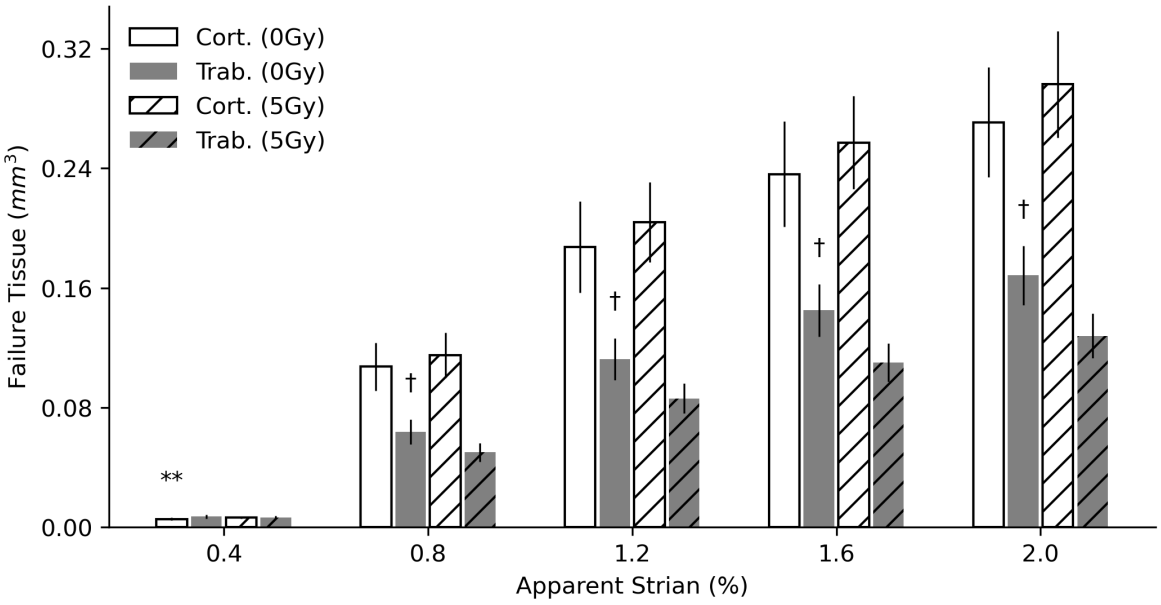

Figure 3-5: The mean $\pm$ SD trabecular and cortical failure tissue at five equal–distance sub–steps (0.4%, 0.8%, 1.2%, 1.6%, 2.0% apparent strain) for both groups. The symbol indicates significant difference between the control and treatment group for that compartment ($** : p < 0.01; \dagger : p < 0.001$). N = 13, 13 (L4 only) for control, irradiate groups, respectively.

Chapter 4

Damage Law and Structural Redundancy in Human Vertebral Body

4.1 Introduction

For the human vertebrae, bone strength has been associated with bone mass, certain measurements of bone micro–architecture, and material–level tissue strength [63, 177, 31]. Thus, aging– and disease–related bone strength loss and increased fracture risk have been attributed to either one of these factors or combined [146, 183, 184, 66, 185]. However, less is known about the overall damage process of human vertebrae as a function of the applied load or the role of structural redundancy in the whole-bone fracture behavior. For example, being an analogy to the crack propagation rate in the field of fracture mechanics, the accumulation rate of damaged tissue in the human vertebrae could reflect the structural–wise fragility, which inherently depends on the bone morphology and material properties. Previous studies have shown that under axial compression loading, the high–risk tissue was relatively more in the trabecular centrum than in the cortical shell, and the initial failure occurred at the endplate of human vertebrae [129, 186, 28]. Nevertheless, it is still unclear if the accumulation rate of high–risk or damaged tissue was the same between these compartments or among human vertebrae with different levels of whole–bone strength. Associated with the concept of the damage process, structural redundancy is also one rarely studied description of the failure mechanism within the human vertebrae [149]. It was reported that a human vertebra with a high level of bone volume fraction was associated with a high degree of structural redundancy [149]. However, it remains unknown how varying degrees of structural redundancy would affect the accumulation rate of damaged tissue, therefore, ultimately affecting the vertebral fracture behavior.

Redundancy in a structure, as a classic concept in civil and aviation engineering [187, 188, 189], could be generally defined as the absence of critical structural components whose failure would cause a collapse of the structure [190, 191, 192, 193]. In the field of bone mechanics, there

have been studies reporting multiple possible load paths in the human vertebra under compression loading, suggesting that if one vertical load path failed, alternative load paths were available, which implied some degree of structural redundancy [64, 148, 176]. However, it is unclear that in the event of significant loss of structural redundancy due to aging or diseases, if the human vertebral fragility, therefore the fracture risk, would increase independently of the loss of bone mass. Such investigation could provide a novel understanding of the evolution of bone [194], and potentially help improve human vertebrae clinical fracture risk assessment.

Thus, the objective of this study was to explore the damage process and structural redundancy within the human vertebrae body using both simplified analytical models and high–resolution micro–computer tomography (micro–CT) based nonlinear finite element (FE) analysis.

4.2 Methods

Two simplified analytical models were used to illustrate the failure mechanism within the human vertebrae (**Figure 4-1**). In the first model, we aimed to study the effect of the number of parallel load paths in the direction of the applied load on the fractured tissue accumulation rate. Six structures were assumed with a varying number (100, 200, 400, 600, 800, and 1200) of elastic brittle vertical rods in parallel in each structure. The bottom ends of all rods were fixed, and the top ends of all rods were connected to a rigid horizontal bar. Both ends allowed horizontal expansion but not rigid body motions. The apparent compressive load was applied on the rigid horizontal bar. The stiffness of all rods was 1.0 N/mm (using unity for simplicity), while the strength of all rods was normally distributed with the mean value of 1.0 N and SD of 0.25 N (if any rod was with negative strength, it was removed). Each rod was elastically deformed under the apparent applied load, while the fractured rods were removed when the internal force was beyond its strength.

The second model was designed to explore the effect of the number of parallel load paths on the fracture tissue accumulation rate while the total structural mass is controlled. Different from the first analytical model, both stiffness and strength of rods were linearly scaled (with the same scaling factor) such that structure–wise stiffness was the same as the 1200–rod structure. All five structures were scaled individually. Other parameters remained the same as in the first model.

For both analytical models, the strength (ultimate force) and the volume of fracture tissue (shorten as the fracture tissue) at each applied load were collected for all six structures. A linear regression model was used to study the relationship between the number of load paths and the structural strength for each model. Separate linear regression models were used to investigate the relationship between the logarithm transformed fracture tissue and applied load for each structure. For each structure, if the correlation was significant, the corresponding slope was defined as the fracture tissue growth rate. The third nonlinear regression model (3–parameter exponential model) was used to study the relationship between the fracture tissue growth rate and structural strength

for each analytical model.

In addition to two analytical models, eight human L1 vertebral bodies (age: 68 $\pm$ 14 years, mean $\pm$ S.D., range: 51 – 89 years, n = 3 female, n = 5 male) were analyzed. All specimens were micro–CT scanned with a resolution of 37 μm (Scanco Medical AG, Brüttisellen, Switzerland), thresholded, and coarsened to a resolution of 74 μm to reduce the computational burden. An averaging technique was used to identify the human vertebral body's cortical shell and cortical endplates [128]. After which, extra elements representing polymethyl methacrylate (PMMA) material were added to both inferior (bottom) and superior (top) endplates to make planar surfaces. To further reduce the computational burden, PMMA elements were elongated in the inferior-superior direction (dimension as 74 μm by 74 μm by 222 μm), where bone elements are isotropic voxels (dimension as 74 μm by 74 μm by 74 μm) [121]. Human vertebral body partition and PMMA element manipulation were processed using an image processing software (IDL software suite, ITT Visual Information Solutions, Boulder, CO, USA). Following that, each 74 μm cubic voxel in the human vertebral body volume was then converted to an 8–noded element to create a human vertebral body finite element model using a customed C++ code [128, 195].

Bone tissue elements were assigned the identical elastic properties: Young's modulus of 18.5 GPa; Poisson's ratio of 0.3 [196], and PMMA elements were assigned fully elastic properties: Young's modulus of 2.5 GPa; Poisson's ratio of 0.3 [63]. To simulate bone tissue behavior in a brittle manner, a manually iterative process was implemented [162]. To initialize the process: all bone tissue was assigned identical fully ductile, rate–independent elasto-plasticity [181] properties: tissue–level tensile and compressive yield strains of 0.33% and 0.69% [120], respectively. Post–yield modulus was 5% of the elastic modulus [118]. Then, the model was constrained by a roller–type boundary condition on the inferior surface and a displacement–type boundary condition on the superior surface [125].

During each iteration (incremental 0.1% uniaxial compressive apparent strain), given the element–wise strain results from the last iteration, any undamaged element with maximum principal strain higher than 0.33% or minimal principal compressive strain lower than -0.69% was classified as a damaged element. Damage was modeled by reducing the Young's modulus 100–fold [162, 180]. Meanwhile, an updated displacement–type boundary condition on the superior surface (an increment of 0.1% before apparent strain of 0.2% and 0.05% after the apparent strain of 0.2% added to the last iteration [125]) was applied on the updated model. Such non–uniform increment of the displacement–type boundary condition was validated in a pilot parameter study and implemented to reduce the computational burden. Then, the updated model with an updated boundary condition was solved from zero–displacement to get the current iteration element–wise strain results. Both geometrical and material nonlinearity were included in the finite element analysis using an implicit, highly–scalable parallel framework (Olympus) [144, 117].

The iterative process was terminated when the resultant reaction force at the superior surface of the current iteration was lower than the one of the last iteration, indicating a whole–bone level fracture occurred. Overall, such a manually iterative process for one human vertebral body specimen consisted of five or six fully nonlinear (both geometrical and material nonlinearity) finite element analyses where each of the analyses provided one data point on the overall whole–bone level force–deformation curve (**Figure 4-2**).

On average, each human vertebral body consisted of 27.7 million elements (16.6 – 45.9 million) and 115 million degree–of–freedoms (74.3.1 – 186.2 million). All analyses were implemented on the Stampede2 supercomputer (Texas Advanced Computing Center, The University of Texas at Austin, TX, U.S.A.). The total computing recourse required for 48 nonlinear analyses was about 144,000 CPU–hours.

The strength of the human vertebral body was defined as the maximum force on the whole–bone level force–deformation curve. The corresponding deformation (in the unit of apparent strain) was defined as the failure apparent strain. Damaged tissue was defined as the volume of damaged bone tissue and was evaluated at each load step (from zero apparent strain to failure apparent strain). All data manipulations and regression analyses were the same as the aforementioned analytical models.

A visual representation of the human vertebral body damaged tissue at the failure apparent strain was made for three representative specimens, including specimens with relatively low–, medium– and high–level strength among all specimens. For each visual representation, bone tissue was projected onto the top view (from the direction of the superior to the inferior aspect of the human vertebral body) to generate the bone density distribution. Damaged tissue was also projected on the top view and overlaid on the bone density distribution. In addition, compression stress in the vertical direction was colorized and plotted at three transverse 0.5 mm thick slices (25%, 50%, and 75% of the total vertebra height). PMMA material was removed from the visual representation for simplicity.

All statistical analysis was in JMP Pro (Ver 16.0), with a significant level at $p < 0.05$.

4.3 Results

For the first analytical model, structural strength was linearly correlated with the number of load paths ($R^2 = 1.0, p < 0.0001$, **Figure 4-3**A). Logarithm transformed damaged tissue was linearly and highly correlated with applied load for all six structures (minimal $R^2 = 0.94$, maximum $p = 0.0001$, **Figure 4-3**B), and the structural strength was nonlinearly correlated with the fracture tissue growth rate ($R^2 = 0.99, p < 0.0001$ for both scale and growth rate in the 3–parameter

exponential model, **Figure 4-3**C).

By contrast, for the second analytical model, the correlation between the structural strength and number of load path ($p = 0.17$) and the correlation between the structural strength and the fracture tissue growth rate ($p = 0.96$ for the scale and $p = 0.32$ for the growth rate in the 3–parameter exponential model) were not significant (**Figure 4-4**A,C). Logarithm transformed fracture tissue was still linearly correlated with applied load for all six structures (minimal $R^2 = 0.94$, maximum $p = 0.0001$, **Figure 4-4**B).

Across all human vertebrae specimens, the logarithm transformed damaged tissue was highly and linearly correlated with applied force up to the whole–bone level fracture, with the minimal R^2 value of 0.98 and maximum p–value of 0.04 (**Table 4-1**). In addition, three representative specimens, including one with low strength, one with medium strength, and one with high strength among eight specimens, showed that such correlation was consistent regardless of the vertebral body strength level (**Figure 4-5**).

The vertebral body damaged tissue growth rate was highly and nonlinearly correlated with the vertebral body strength, with a p-value < 0.001 (for both scale and growth rate in the 3–parameter exponential model) and $R^2 = 0.96$ (**Figure 4-6**). Such results indicated that a weak vertebra may accumulate damaged tissue more rapidly than a strong one, and this trend was flattened when the vertebrae strength was beyond a certain threshold.

The damaged tissue spatial distribution overlaying on the areal bone tissue density spatial distribution for three representative specimens indicated a varying number of load paths from the top view (**Figure 4-7**). For the specimen with low or medium strength, There were regions where there was practically no vertical load path being heavily loaded or damaged. By contrast, the specimen with high strength demonstrated a more uniform and distributed damaged tissue pattern, which may translate to a larger number of existing damaged vertical load paths across the whole cross–section of the specimen.

4.4 Discussion

Our results revealed the exponential damage law and its relationship to bone strength of the human vertebral body. Quantitatively, the volume of damaged tissue increases exponentially as the applied load increases on the whole–bone level. Expressly, the growth rate of the damaged tissue indicated whether the vertebral body accumulated damaged tissue relatively slowly or rapidly. Furthermore, we showed that damaged tissue growth rate was negatively and nonlinearly correlated with the human vertebral body strength, and this relationship could be explained by the number of load paths within the vertebral body in the direction of the applied load.

Mechanistically, a human vertebral body with a low strength level is associated with either small bone size or high bone porosity [197, 198]. Thus, there would be a low number of load paths in the direction of the applied load [64]. As suggested by our first simplified analytical model with a low number of load paths, when failure progressively occurred as the applied load increased, alternative undamaged load paths rarely existed. As a result, an initial damaged load path led to a large accumulation rate of following damaged load paths. When there were a sufficient number of damaged load paths, the ultimate force would occur as the structural strength. Therefore, a weak human vertebral body was associated with a high growth rate of damaged tissue, thus, more structural fragility, which could be attributed to the low number of available load paths in the direction of applied loading.

Our study provided new insights into the human vertebral body fragility and fracture risk. Current theory states that bone fracture risk depends on the applied loading (either of physiological activity or trauma) and the bone load–bearing capability [26]. The loading–bearing capabilities, such as whole–bone level strength, are inherently associated with the material – tissue–level properties – and geometry – bone size and trabecular micro–architecture [125, 162, 80, 60]. Studies have shown that vertebral body fracture risk is affected by age, sex, areal BMD (the main predictor), as well as prior fracture incidence (a strong prediction independent of areal BMD) [199, 31]. However, estimating vertebral fracture risk with high sensitivity is still challenging [13, 137]. Our findings suggested that structural fragility (interpreted from the growth rate of damaged tissue) could play a role in determining the vertebral body fracture risk. As age–related osteoporosis develops, there will be decreasing trabecular number, trabecular connectivity, and trabecular vertical bone volume fraction in the older human vertebral body [68]. Thus, the number of possible load paths in the direction of applied load decreases. With decreased number of load paths available, damaged tissue accumulation is faster and more localized in a high load–to–strength ratio situation. As a result, the osteoporotic vertebral body behaves structurally more brittle than a healthy one. This increased structural fragility may partially explain the increase of the vertebral body fracture risk in the event of subcritical loading followed by overloading or repeated subcritical loadings.

Previous studies demonstrated that a strong human vertebral body was associated with a larger damaged tissue fraction, therefore, possibly a higher degree of structural redundancy than a weak one [149]. In addition, our second analytical model, where the total structural mass was controlled, showed that the arrangement of load paths or degree of structural redundancy had no effect on the structural strength or the damaged tissue growth rate. Therefore, it implied that the structural redundancy in the human vertebral body might not contribute to the fracture risk independent of the low bone strength.

This work showed one of the advantages of investigating the damage process of human bone specimens using a nonlinear whole–bone FE model. There were numerous studies reporting the spatial distribution of failure tissue in the human vertebral body or femoral neck [176, 138, 135],

where results were evaluated at the yielding or ultimate loading step. Such one–point evaluation may bring researchers insights into the failure location or the weakest link within the whole bone, such as vertebral body endplates [186]. However, they did not provide insights into the accumulation rate of damaged tissue, which could be interpreted as structural fragility. In this work, the association between damaged tissue growth rate and whole–bone level strength indicated that a weak human vertebra was structurally more brittle than a strong one, and such a high growth rate of damaged tissue may be related to the increased fracture risk due to aging or diseases in a repeated subcritical loading scenario.

One of the limitations of this study is using the brittle tissue–level material property. It is known that the tissue–level ductility in the FE model could affect the whole–bone level strength by as much as 50% for the human vertebral body [180]. Furthermore, one S.D. change in the tissue–level ductility may result in around 7% change in the whole–bone strength [125]. Therefore, using a fully brittle material property in the FE model may diminish the relationship between the damaged tissue growth rate and whole–bone level strength by reducing the strength difference across specimens. However, given the identical tissue–level material property, variation in the damaged tissue growth rate among specimens inherently arose from the variation in human vertebral body micro–architecture and the re–distribution of the applied load as the fracture progressively occurred. Although assigning a fully brittle material property in the FE model may result in tissue damage earlier than assigning a ductile one. Introducing tissue–level ductility would only exaggerate the strength difference between specimens with varying numbers of load paths. Thus, the negative relationship between the damaged tissue growth rate and whole–bone level strength remained valid.

Table 4-1: Eight specimen strength values, correlation p–values, and R^2 values for the relationship between transformed damaged tissue and strength. Specimen ID as letter were specimen used in **Figure 4-5** and **Figure 4-7** as the representative specimens with relatively low–(L), medium–(M), and high–(H) strength among all specimens.

Specimen ID	Strength (N)	p-value	R^2
1	1277.3	0.045	1.00
L	1313.7	0.002	1.00
3	3492.2	0.001	0.99
4	3985.6	< 0.001	0.99
M	4291.7	< 0.001	1.00
6	4795.1	0.001	1.00
H	7928.3	< 0.001	0.98
8	7949.0	< 0.001	0.99

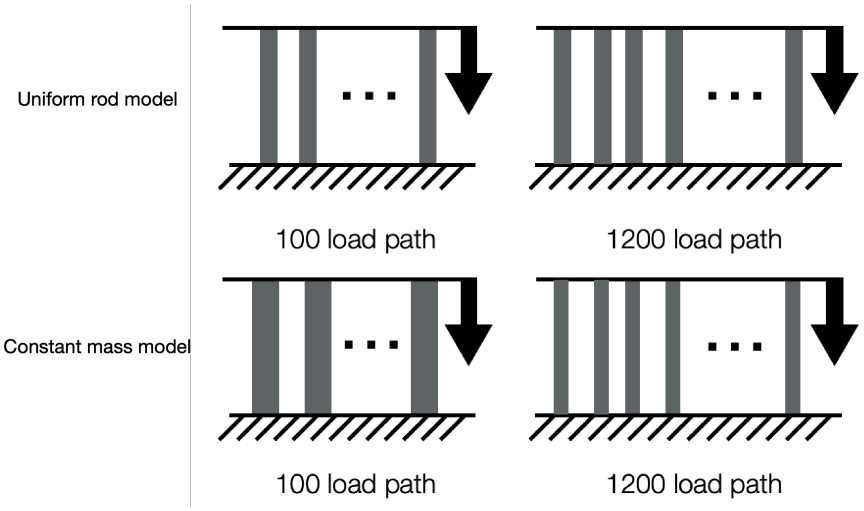

Figure 4-1: An illustration of two simplified analytical models. The first row shows the first analytical model (two structures out of six) with a varying number of parallel load paths. The arrow indicates the applied loading direction. The second row shows the second analytical model (two structures out of six) with constant structural mass.

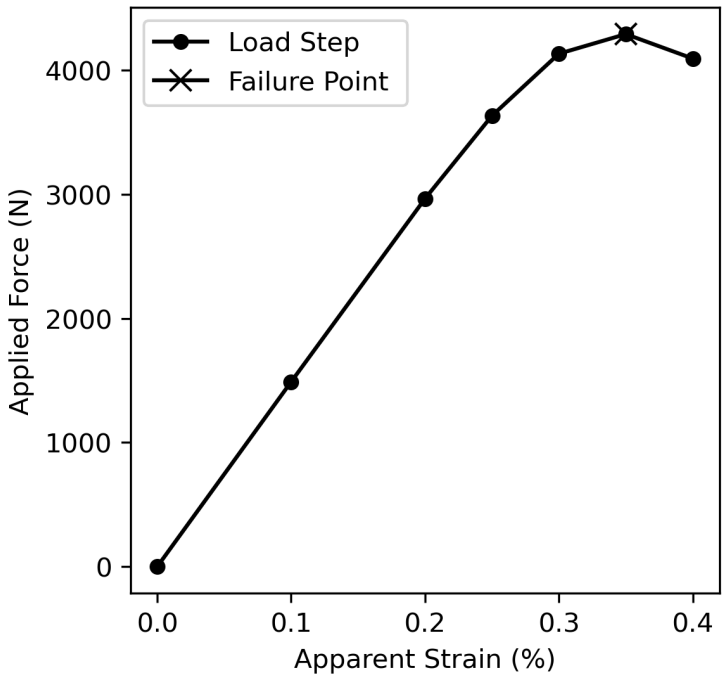

Figure 4-2: The force–deformation curve of one human vertebral body specimen, acquired from an iterative finite element analysis. Each dot (excluding the one at the origin) was a data point from a nonlinear (both geometric and material–wise) finite element analysis. The applied load was chosen to minimize the computational burden in the linear region on the force–deformation curve and maximize the resolution beyond the linear region.

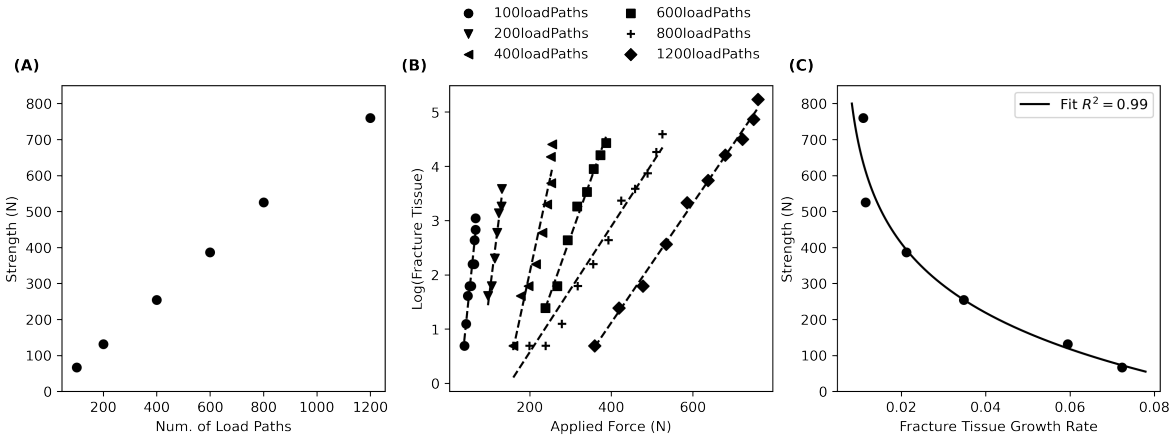

Figure 4-3: (A) The scatter plot of the number of load paths in structures and the corresponding structural strength in the first analytical model. (B) Logarithm transformed fracture tissue and applied load relationship of six structures. The fitted line indicated the linear regression. (C) The fracture tissue growth rate and strength relationship of all six structures. The solid line indicated the nonlinear regression of a 3–parameter exponential model.

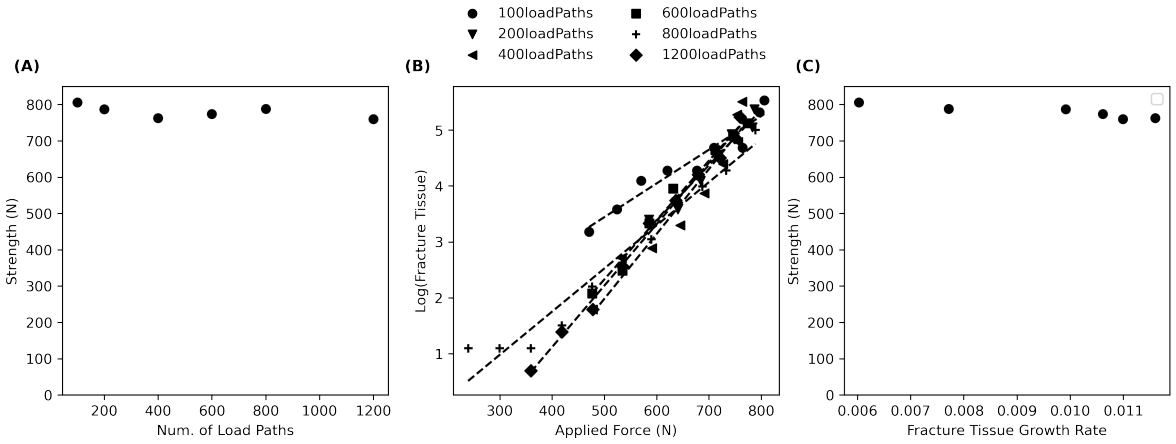

Figure 4-4: (A) The scatter plot of the number of load paths in structures and the corresponding structural strength in the second analytical model. (B) Logarithm transformed fracture tissue and applied load relationship of six structures. The fitted line indicated the linear regression. (C) The scatter plot of fracture tissue growth rate and strength of all six structures.

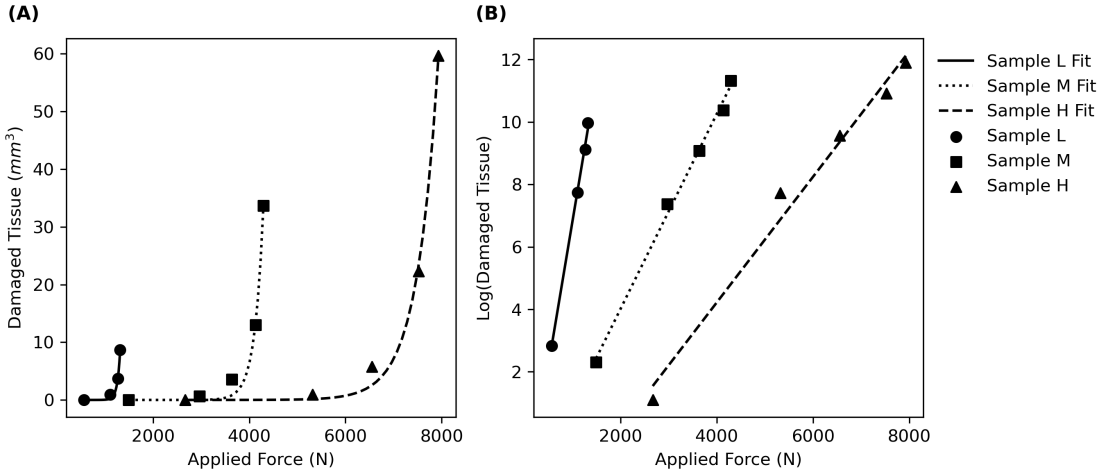

Figure 4-5: (A) The damaged tissue and (B) logarithm transformed damaged tissue and applied load relationship of three representative human vertebral body specimens (specimen L, M, and H from **Table 4-1**). The fitted line indicated the (A) exponential regression and (B) linear regression.

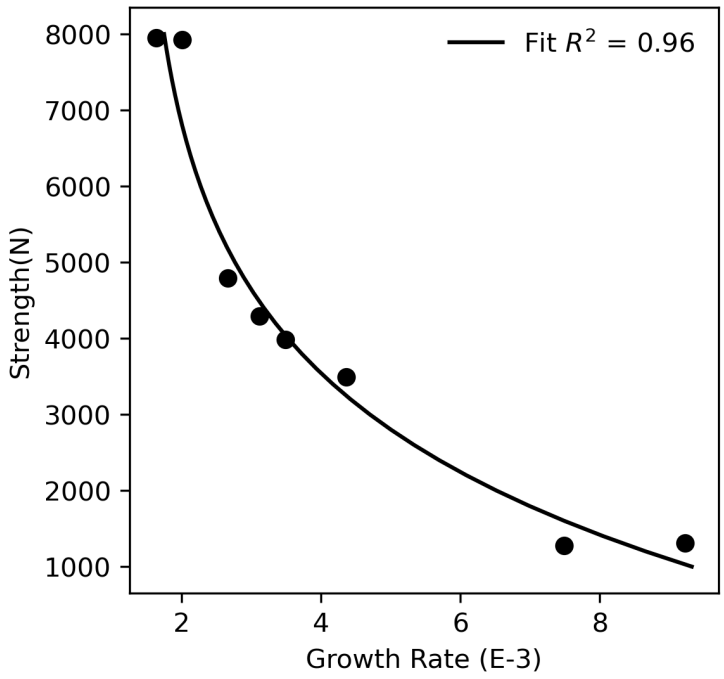

Figure 4-6: The damaged tissue growth rate and strength relationship of all eight human vertebral body specimens. The solid line indicated the nonlinear regression of a 3–parameter exponential model.

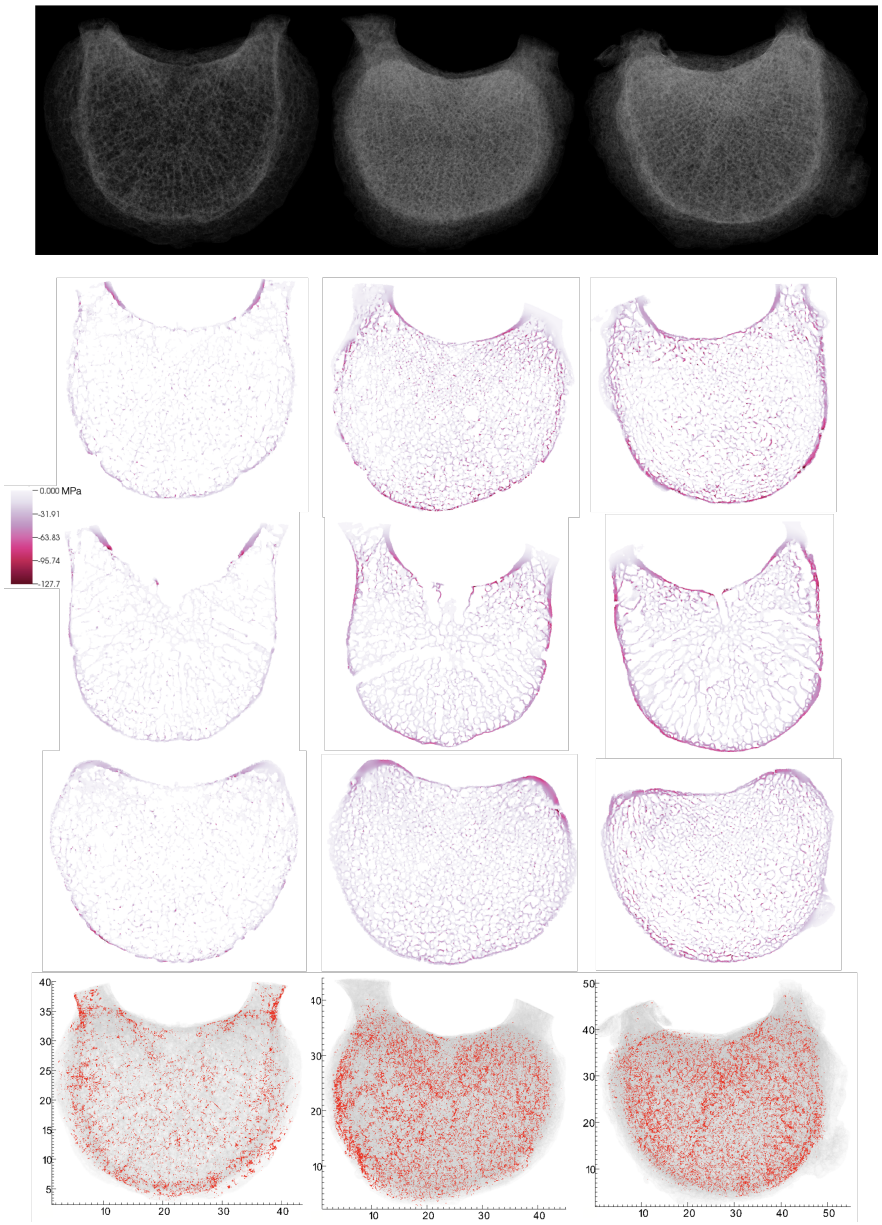

Figure 4-7: The visual representation of bone density distribution (row 1), stress distribution at 75% (row 2), 50% (row 3), 25% (row 4) vertebral height, and damaged tissue distribution (row 5) of three representative human vertebral body specimens (specimen L – left column, M – middle column, and H – right column from **Table 4-1**). Bone density distribution was 2D projection to the top–view. Stress distribution was colorized compression stress at 0.4% apparent strain. Damaged tissue distribution was 2D projection to the top–view overlaying on a bone density distribution projection. Damaged tissue was tissue with maximum principal strain higher than 0.33% or minimal principal strain lower than -0.69% at 0.4% apparent strain.

Chapter 5

Conclusion and Future Works

The overall goal of this work was to improve the fundamental understanding of vertebral micro–mechanics and failure mechanisms, and it was of both scientific and clinical significance. From the essential scientific perspective, this work revealed the protective role of the cortical shell in the vertebral body following irradiation and how ionizing irradiation altered the vertebral strength independent of the alteration in vertebral stiffness in a small animal model. Moreover, this work also established the fundamental exponential damage law in the human vertebral body and its relationship to human vertebral strength. From the clinical perspective, our work enlightened the pathway by which changes in vertebral micro–architecture manifest into changes in whole–bone stiffness and strength, which can be used in the application of aging and drug treatment if similar morphological changes are observed. Furthermore, we also elucidated the structural fragility aspect of the human vertebrae, which may contribute to the understanding of osteoporosis etiology and improvement of future clinical intervention.

Chapter 2 established how ionizing radiation affected mouse vertebral body structure–function relationship and the protective role of the cortical shell in the mouse vertebral body stiffness. Existing studies showed inconsistency between changes in trabecular micro–architecture and whole–bone stiffness following short–term ionizing radiation in mouse vertebral bodies. To explain the inconsistency, we used a high–resolution micro–CT based linear finite element modeling technique. Our results provided evidence that ionizing radiation negatively impacted trabecular mass sharing. Consequently, the trabecular load sharing was reduced, and axial compression load was shifted to the unchanged cortical compartment. In addition to the mass sharing and load sharing changes, we also found a trabecular load–bearing efficiency degradation following irradiation. Expressly, with the same level of mass fraction, the trabecular compartment load fraction was lower following irradiation. Taking the reduced mass sharing and load–bearing efficiency together, we concluded that ionizing radiation shifted axial compression load to the cortical shell, which was already the primary compartment of load–bearing. Therefore, there was no observable change in whole–bone stiffness when there was no observable change in the cortical mass and micro–

architecture following irradiation. This work mechanistically explained the unexpected inconsistency observed in a previous experimental study. More importantly, it brought insights into how ionizing radiation altered the inherent structure–function relationship within the mouse vertebral body, while the whole–bone stiffness showed no significant difference following irradiation. Furthermore, we showed that shifted axial compression load in the cortical shell would increase the amount of initially–failed tissue in the cortical shell, which implied that the protective effect of the cortical shell might not extend to the mouse vertebral strength. From the clinical perspective, we acknowledged the similarity and difference between the mouse (small animal model) and human vertebrae, where the cortical shell played a primary role in the load sharing in the mouse vertebral body but not in the human vertebral body. Thus, the protective effect of the cortical shell may not be extrapolated into human vertebrae cases. However, the changes in trabecular micro–architecture and corresponding changes in the structural–function relationship in the vertebral body may still apply in the study of age–related osteoporosis and drug treatment.

Chapter 3 reported how ionizing radiation affected mouse vertebral stiffness and strength independently by altering the failure tissue in the trabecular compartment. As a natural extension of the linear study in the **Chapter 2**, here we used a high–resolution micro–CT based nonlinear finite element modeling with asymmetric failure criterion to explore the effect of ionizing radiation on the failure mechanism of the mouse vertebral body. Our primary results showed that ionizing radiation reduced both vertebral body stiffness and strength. Using the regression analysis, the correlation between whole–bone stiffness and strength was altered by irradiation. Specifically, the vertebral body with the same level of stiffness was associated with lower strength in the irradiation group than in the control group. This altered stiffness–strength correlation suggested that the vertebral failure mechanism was altered by irradiation. Related to this regression analysis, we argued that the change in vertebral body failure tissue following irradiation – primarily the change in the trabecular failure tissue – was the key explanatory variable to the independent effect of irradiation on the whole–bone strength. Therefore, we concluded that ionizing radiation affected mouse vertebral body strength more than stiffness by affecting the amount of trabecular failure tissue. While the linear finite element analysis in previous work could only provide initially–failed tissue distribution, the nonlinear finite element analysis in this work revealed the actual failure process of the vertebral body. We provided evidence that cortical failure tissue was more than half of the vertebral body failure tissue, and ionizing radiation accentuated such difference, therefore, affecting the vertebral failure mechanism. Although this work focused on the alteration in failure mechanism induced by short–term ionizing radiation, the implication may be valuable for aging– and osteoporosis–related study. Since the change in failure mechanism was inherently associated with changes in bone porosity and bone micro–architecture.

Together, **Chapter 3** and **Chapter 2** elucidated the mechanism by which ionizing radiation affects mouse vertebral body morphology and, therefore, bone stiffness, then ultimately, bone strength. We observed that ionizing radiation negatively impacted the trabecular mass and micro–architecture, resulting in a less efficient load–bearing trabecular compartment and shifting the ax-

ial compression load into the cortical shell. The cortical shell played the primary role in the load sharing and showed a limited protective effect on the whole vertebral stiffness. As the load was beyond the linear region, the reduced trabecular mass and sparse trabecular micro–architecture led to significantly reduced trabecular failure tissue under axial compression, which resulted in a significantly reduced vertebral failure tissue. Such effect contributed to a reduction in vertebral strength independent of the reduction in vertebral stiffness. Thus, our work illustrated how ionizing radiation affects mouse vertebral structure–function relationship and failure mechanism. From the clinical perspective, our work suggested that for aging and osteoporosis development, the loss of vertebral trabecular load sharing may be more than the loss of trabecular mass and micro–architecture since the trabecular structure-function relationship could be altered as the micro–architecture degrading. Furthermore, the loss of vertebral strength may be more than the loss of vertebral stiffness since the failure mechanism could be affected as osteoporosis develops.

Chapter 4 quantified the exponential damage law and its nonlinear relationship with the whole–bone strength in the human vertebral body. In this work, we aimed to explore the damage process and structural redundancy aspects of the human vertebral body and their relation to the fracture risk of human vertebrae. Using the high–resolution micro–CT based nonlinear finite element analysis, our results indicated that the fracture tissue accumulated exponentially as the apparent load was incrementally applied. Moreover, the fracture tissue growth rate was negatively correlated with the whole–bone strength, implying that a weak vertebra accumulated fracture tissue with a higher rate than a strong vertebra. Furthermore, simplified analytical modeling was used to explain the mechanism behind the observations, where it suggested that the fracture tissue growth rate was associated with the number of load paths in the direction of the applied load. Therefore, we have concluded that the higher growth rate of fracture tissue, therefore, more structural–wise fragility of a weak human vertebral body was due to a low number of vertical load paths under axial compression loading. Moreover, our second analytical model implied that the number of load paths did not affect the fracture tissue growth rate if the total bone mass was controlled. Such findings may partially elucidate the etiology of osteoporosis. While previous studies have shown evidence that the loss of bone mass, bone micro–architecture was associated with loss of bone strength, thereby increasing the fracture risk. Our work demonstrated that the increase in structural fragility may also contribute to the increase of fracture risk in human vertebrae.

There are two potential directions of research based on the conclusions provided by this work. Firstly, we have illustrated the mechanism by which ionizing radiation affects the vertebral body morphology, stiffness, and strength. However, the observation was limited to the murine model. While the load–sharing characteristics are in a similar U–shape for both mouse and human vertebral bodies, the mouse vertebral body showed a relatively thick cortical shell and a high load fraction in the cortical shell. By contrast, the human vertebral body trabecular centrum showed a higher load fraction than the cortical shell. Therefore, to understand the mechanism by which ionizing radiation from radiation therapy or long–term space travel affects the human vertebral body, thereby improving the clinical intervention methods, it is necessary to study how the structure–

function relationship and failure mechanism could be altered in the human vertebra using a computational approach. Secondly, we have addressed how structural fragility may play a role in the fracture risk of the human vertebral body. However, our specimens were limited to the old population, where the whole–bone strength was lower than a healthy young human vertebra. Thus, it is worth expanding the investigation into the young population. As such study may reveal the relationship between damaged tissue accumulation rate and aging, providing insights into the etiology of age–related osteoporosis and corresponding interventions.

In closure, this work enhances the understanding of vertebral micro–mechanics and failure mechanisms for both scientific and clinical interests, specifically

- We revealed the effect of ionizing radiation on the mouse vertebral body structure–function relationship and load–sharing, namely, ionizing radiation reduced the trabecular load fraction by lowering the trabecular mass fraction. Meanwhile, it also altered the correlation between the trabecular load fraction and trabecular mass fraction. Those changes explained the difference in effect size between the changes in bone morphology and changes in whole–bone elastic properties.
- We revealed the effect of ionizing radiation on the mouse vertebral body failure mechanism, namely, ionizing radiation reduced the mouse vertebral body failure tissue by lowering the trabecular failure tissue, which explained the effect of ionizing radiation on mouse vertebral body strength independent of the detriment in vertebral body stiffness.
- This work established the nonlinear relationship between the damaged tissue growth rate and human vertebral body whole–bone strength, which mechanistically was determined by the number of vertical load paths under axial compressive loading.

Reference

[1] Peter Grabowski. “Physiology of Bone”. In: *Endocr. Dev.* Vol. 28. 2015, pp. 33–55. DOI: 10.1159/000380991.

[2] Jeffry S. Nyman, Jesse L. Even, Chan Hee Jo, Erik G. Herbert, Matthew R. Murry, Gael E. Cockrell, Elizabeth C. Wahl, R. Clay Bunn, Charles K. Lumpkin, John L. Fowlkes, and Kathryn M. Thrailkill. “Increasing duration of type 1 diabetes perturbs the strength-structure relationship and increases brittleness of bone”. In: *Bone* 48.4 (2011), pp. 733–740. DOI: 10.1016/j.bone.2010.12.016.

[3] Tony M. Keaveny, David L. Kopperdahl, L. Joseph Melton, Paul F. Hoffmann, Shreyasee Amin, B. Lawrence Riggs, and Sundeep Khosla. “Age-dependence of femoral strength in white women and men”. In: *J. Bone Miner. Res.* 25.5 (2010), pp. 994–1001. DOI: 10.1002/jbmr.091033.

[4] Elizabeth J. Samelson, Blaine A. Christiansen, Serkalem Demissie, Kerry E. Broe, Qiong Louie-Gao, L. Adrienne Cupples, Benjamin J. Roberts, Rajaram Manoharam, John D’Agostino, Thomas Lang, Douglas P. Kiel, and Mary L. Bouxsein. “QCT measures of bone strength at the thoracic and lumbar spine: The Framingham study”. In: *J. Bone Miner. Res.* 27.3 (2012), pp. 654–663. DOI: 10.1002/jbmr.1482.

[5] Elise F. Morgan, Ginu U. Unnikrisnan, and Amira I. Hussein. “Bone Mechanical Properties in Healthy and Diseased States”. In: *Annu. Rev. Biomed. Eng.* 20.1 (2018), pp. 119–143. DOI: 10.1146/annurev-bioeng-062117-121139.

[6] B. K. Silverman. “Consensus development conference: Diagnosis, prophylaxis, and treatment of osteoporosis”. In: *Am. J. Med.* 94.6 (June 1993), pp. 646–650. DOI: 10.1016/0002-9343(93)90218-E.

[7] Russel Burge, Bess Dawson-Hughes, Daniel H. Solomon, John B. Wong, Alison King, and Anna Tosteson. “Incidence and Economic Burden of Osteoporosis-Related Fractures in the United States, 2005-2025”. In: *J. Bone Miner. Res.* 22.3 (Mar. 2007), pp. 465–475. DOI: 10.1359/jbmr.061113.

[8] Michael A Clynes, Nicholas C Harvey, Elizabeth M Curtis, Nicholas R Fuggle, Elaine M Dennison, and Cyrus Cooper. “The epidemiology of osteoporosis”. In: *Br. Med. Bull.* 133.1 (Apr. 2020), pp. 105–117. DOI: 10.1093/bmb/ldaa005.

[9] Dana Bliuc, Nguyen D. Nguyen, Vivienne E. Milch, Tuan V. Nguyen, John A. Eisman, and Jacqueline R. Center. “Mortality risk associated with low-trauma osteoporotic fracture and subsequent fracture in men and women”. In: *JAMA - J. Am. Med. Assoc.* 301.5 (2009), pp. 513–521. DOI: 10.1001/jama.2009.50.

[10] Anna Oleksik, Paul Lips, Alison Dawson, Michael E. Minshall, Wei Shen, Cyrus Cooper, and John Kanis. “Health-related quality of life in postmenopausal women with low BMD with or without prevalent vertebral fractures.” In: *J. Bone Miner. Res.* 15.7 (July 2000), pp. 1384–92. DOI: 10.1359/jbmr.2000.15.7.1384.

[11] Olof Johnell and John Kanis. “Epidemiology of osteoporotic fractures”. In: *Osteoporos. Int.* 16.SUPPL. 2 (2005), pp. 6–10. DOI: 10.1007/s00198-004-1702-6.

[12] Nancy E. Lane. “Epidemiology, etiology, and diagnosis of osteoporosis”. In: *Am. J. Obstet. Gynecol.* 194.2 (Feb. 2006), S3–S11. DOI: 10.1016/j.ajog.2005.08.047.

[13] John A. Kanis. “Osteoporosis III: Diagnosis of osteoporosis and assessment of fracture risk”. In: *Lancet* 359.9321 (June 2002), pp. 1929–1936. DOI: 10.1016/S0140-6736(02)08761-5.

[14] T. Lang, P. Augat, S. Majumdar, X. Ouyang, and H. K. Genant. “Noninvasive assessment of bone density and structure using computed tomography and magnetic resonance.” In: *Bone* 22.5 Suppl (May 1998), 149S–153S. DOI: 10.1016/s8756-3282(98)00005-2.

[15] J A Kanis and C C Glüer. “An update on the diagnosis and assessment of osteoporosis with densitometry. Committee of Scientific Advisors, International Osteoporosis Foundation.” In: *Osteoporos. Int.* 11.3 (2000), pp. 192–202. DOI: 10.1007/s001980050281.

[16] J. A. Kanis. “Assessment of fracture risk and its application to screening for postmenopausal osteoporosis: synopsis of a WHO report. WHO Study Group.” In: *Osteoporos. Int.* 4.6 (Nov. 1994), pp. 368–81. DOI: 10.1007/BF01622200.

[17] E. Orwoll. “Assessing bone density in men.” In: *J. Bone Miner. Res.* 15.10 (Oct. 2000), pp. 1867–70. DOI: 10.1359/jbmr.2000.15.10.1867.

[18] P. L. Selby, M. Davies, and J. E. Adams. “Do men and women fracture bones at similar bone densities?” In: *Osteoporos. Int.* 11.2 (2000), pp. 153–7. DOI: 10.1007/PL00004177.

[19] Deborah Marshall, Olof Johnell, and Hans Wedel. “Meta-analysis of how well measures of bone mineral density predict occurrence of osteoporotic fractures.” In: *BMJ* 312.7041 (May 1996), pp. 1254–9. DOI: 10.1136/bmj.312.7041.1254.

[20] J. A. Kanis, O. Johnell, A. Oden, C. De Laet, B. Jonsson, and A. Dawson. “Ten-year risk of osteoporotic fracture and the effect of risk factors on screening strategies.” In: *Bone* 30.1 (Jan. 2002), pp. 251–8. DOI: 10.1016/s8756-3282(01)00653-6.

[21] Tara Coughlan and Frances Dockery. “Osteoporosis and fracture risk in older people”. In: *Clin. Med. (Northfield. Il).* 14.2 (Apr. 2014), pp. 187–191. DOI: 10.7861/clinmedicine.14-2-187.

[22] Yasser El Miedany. “FRAX: re-adjust or re-think.” In: *Arch. Osteoporos.* 15.1 (2020), p. 150. DOI: 10.1007/s11657-020-00827-z.

[23] John A. Kanis, Nicholas C. Harvey, Helena Johansson, Enwu Liu, Liesbeth Vandenput, Mattias Lorentzon, William D. Leslie, and Eugene V. McCloskey. “A decade of FRAX: how has it changed the management of osteoporosis?” In: *Aging Clin. Exp. Res.* 32.2 (Feb. 2020), pp. 187–196. DOI: 10.1007/s40520-019-01432-y.

[24] J. A. Kanis, A. Oden, O. Johnell, H. Johansson, C. De Laet, J. Brown, P. Burckhardt, C. Cooper, C. Christiansen, S. Cummings, J. A. Eisman, S. Fujiwara, C. Glüer, D. Goltzman, D. Hans, M-A Krieg, A. La Croix, E. McCloskey, D. Mellstrom, L. J. Melton, H. Pols, J. Reeve, K. Sanders, A-M Schott, A. Silman, D. Torgerson, T van Staa, N. B. Watts, and N. Yoshimura. “The use of clinical risk factors enhances the performance of BMD in the prediction of hip and osteoporotic fractures in men and women.” In: *Osteoporos. Int.* 18.8 (Aug. 2007), pp. 1033–46. DOI: 10.1007/s00198-007-0343-y.

[25] John A. Kanis, Nicholas C Harvey, Cyrus Cooper, Helena Johansson, Anders Odén, Eugene V McCloskey, and Advisory Board of the National Osteoporosis Guideline Group. “A systematic review of intervention thresholds based on FRAX : A report prepared for the National Osteoporosis Guideline Group and the International Osteoporosis Foundation.” In: *Arch. Osteoporos.* 11.1 (2016), p. 25. DOI: 10.1007/s11657-016-0278-z.

[26] Christopher J. Hernandez and Marjolein C.H. van der Meulen. “Understanding Bone Strength Is Not Enough”. In: *J. Bone Miner. Res.* 32.6 (2017), pp. 1157–1162. DOI: 10.1002/jbmr.3078.

[27] David E. Krebs, Claire E. Robbins, Leroy Lavine, and Robert W. Mann. “Hip biomechanics during gait.” In: *J. Orthop. Sports Phys. Ther.* 28.1 (July 1998), pp. 51–9. DOI: 10.2519/jospt.1998.28.1.51.

[28] Thomas R. Oxland. “Fundamental biomechanics of the spine–What we have learned in the past 25 years and future directions.” In: *J. Biomech.* 49.6 (Apr. 2016), pp. 817–832. DOI: 10.1016/j.jbiomech.2015.10.035.

[29] Yasumu Kijima and Steven F. Viegas. “Wrist anatomy and biomechanics.” In: *J. Hand Surg. Am.* 34.8 (Oct. 2009), pp. 1555–63. DOI: 10.1016/j.jhsa.2009.07.019.

[30] J. Lo and J. A. Ashton-Miller. “Effect of pre-impact movement strategies on the impact forces resulting from a lateral fall.” In: *J. Biomech.* 41.9 (2008), pp. 1969–77. DOI: 10.1016/j.jbiomech.2008.03.022.

[31] Dennis E. Anderson, Katelyn Burkhart, Mohammad Mehdi Alemi, and Mary L. Bouxsein. “Biomechanics of hip and vertebral fractures”. In: *Marcus Feldman’s Osteoporos.* 2021, pp. 357–378. DOI: 10.1016/B978-0-12-813073-5.00016-2.

[32] Jian Shen, Carrie M. Nielson, Lynn M. Marshall, David C. Lee, Tony M. Keaveny, Eric S. Orwoll, and Osteoporotic Fractures in Men MrOS Research Group. "The Association Between BMI and QCT-Derived Proximal Hip Structure and Strength in Older Men: A Cross-Sectional Study." In: *J. Bone Miner. Res.* 30.7 (July 2015), pp. 1301–8. DOI: 10.1002/jbmr.2450.

[33] Jonathan Reeve and Nigel Loveridge. "The fragile elderly hip: mechanisms associated with age-related loss of strength and toughness." In: *Bone* 61 (Apr. 2014), pp. 138–48. DOI: 10.1016/j.bone.2013.12.034.

[34] Cyrus Cooper, Elizabeth J. Atkinson, W. MichaelO'Fallon, and Joseph L. Melton. "Incidence of clinically diagnosed vertebral fractures: A population-based study in rochester, minnesota, 1985-1989". In: *J. Bone Miner. Res.* 7.2 (1992), pp. 221–227. DOI: 10.1002/jbmr.5650070214.

[35] Claire Acevedo, Vincent A. Stadelmann, Dominique P. Pioletti, Tamara Alliston, and Robert O. Ritchie. "Fatigue as the missing link between bone fragility and fracture". In: *Nat. Biomed. Eng.* 2.2 (Feb. 2018), pp. 62–71. DOI: 10.1038/s41551-017-0183-9.

[36] Tony M. Keaveny, Elise F. Morgan, and Oscar C. Yeh. "Bone Mechanics". In: *Stand. Handb. Biomed. Eng. Des.* Vol. 9. 4. Jan. 2004, pp. 360–366. DOI: 10.3109/10731198109119616.

[37] Bart Clarke. "Normal bone anatomy and physiology." In: *Clin. J. Am. Soc. Nephrol.* 3 Suppl 3 (Nov. 2008), S131–9. DOI: 10.2215/CJN.04151206.

[38] Monzur Murshed. "Mechanism of Bone Mineralization." In: *Cold Spring Harb. Perspect. Med.* 8.12 (2018), pp. 1–11. DOI: 10.1101/cshperspect.a031229.

[39] R. O. Ritchie, J. H. Kinney, J. J. Kruzic, and R. K. Nalla. "A fracture mechanics and mechanistic approach to the failure of cortical bone". In: *Fatigue Fract. Eng. Mater. Struct.* 28.4 (2005), pp. 345–371. DOI: 10.1111/j.1460-2695.2005.00878.x.

[40] Susan M. Snyder and Erich Schneider. "Estimation of mechanical properties of cortical bone by computed tomography." In: *J. Orthop. Res.* 9.3 (May 1991), pp. 422–31. DOI: 10.1002/jor.1100090315.

[41] David L. Kopperdahl and Tony M. Keaveny. "Yield strain behavior of trabecular bone." In: *J. Biomech.* 31.7 (July 1998), pp. 601–8. DOI: 10.1016/s0021-9290(98)00057-8.

[42] Elise F. Morgan and Tony M. Keaveny. "Dependence of yield strain of human trabecular bone on anatomic site". In: *J. Biomech.* 34.5 (2001), pp. 569–577. DOI: 10.1016/S0021-9290(01)00011-2.

[43] L J Gibson. "The mechanical behaviour of cancellous bone." In: *J. Biomech.* 18.5 (May 1985), pp. 317–28. DOI: 10.1016/0021-9290(85)90287-8.

[44] J. C. Rice, S. C. Cowin, and J. A. Bowman. "On the dependence of the elasticity and strength of cancellous bone on apparent density." In: *J. Biomech.* 21.2 (1988), pp. 155–68. DOI: 10.1016/0021-9290(88)90008-5.

[45] Tony KEAVENY and Wilson C. HAYES. “Mechanical properties of cortical and cancellous bone tissue”. In: *Bone*. JANUARY 1993. 1993, pp. 285–344. DOI: doi:10.1201/b14263-14.

[46] Mary L. Bouxsein, Stephen K. Boyd, Blaine A. Christiansen, Robert E. Guldberg, Karl J. Jepsen, and Ralph Müller. “Guidelines for assessment of bone microstructure in rodents using micro-computed tomography”. In: *J. Bone Miner. Res.* 25.7 (2010), pp. 1468–1486. DOI: 10.1002/jbmr.141.

[47] T Hildebrand, Andres Laib, R Müller, J Dequeker, and P Rüegsegger. “Direct three-dimensional morphometric analysis of human cancellous bone: microstructural data from spine, femur, iliac crest, and calcaneus.” In: *J. Bone Miner. Res.* 14.7 (July 1999), pp. 1167–74. DOI: 10.1359/jbmr.1999.14.7.1167.

[48] Martin Stauber and Ralph Müller. “Volumetric spatial decomposition of trabecular bone into rods and plates - A new method for local bone morphometry”. In: *Bone* 38.4 (2006), pp. 475–484. DOI: 10.1016/j.bone.2005.09.019.

[49] A. Odgaard and H J Gundersen. “Quantification of connectivity in cancellous bone, with special emphasis on 3-D reconstructions.” In: *Bone* 14.2 (1993), pp. 173–82. DOI: 10.1016/8756-3282(93)90245-6.

[50] Donald T. Reilly and Albert H. Burstein. “The elastic and ultimate properties of compact bone tissue.” In: *J. Biomech.* 8.6 (1975), pp. 393–405. DOI: 10.1016/0021-9290(75)90075-5.

[51] Mohammad J. Mirzaali, J. Jakob Schwiedrzik, Suwanwadee Thaiwichai, James P. Best, Johann Michler, Philippe K. Zysset, and Uwe Wolfram. “Mechanical properties of cortical bone and their relationships with age, gender, composition and microindentation properties in the elderly.” In: *Bone* 93 (2016), pp. 196–211. DOI: 10.1016/j.bone.2015.11.018.

[52] Xuanliang N. Dong, Rae L. Acuna, Qing Luo, and Xiaodu Wang. “Orientation dependence of progressive post-yield behavior of human cortical bone in compression.” In: *J. Biomech.* 45.16 (Nov. 2012), pp. 2829–34. DOI: 10.1016/j.jbiomech.2012.08.034.

[53] M. J. Ciarelli, S. A. Goldstein, J. L. Kuhn, D. D. Cody, and M. B. Brown. “Evaluation of orthogonal mechanical properties and density of human trabecular bone from the major metaphyseal regions with materials testing and computed tomography.” In: *J. Orthop. Res.* 9.5 (Sept. 1991), pp. 674–82. DOI: 10.1002/jor.1100090507.

[54] Tony M. Keaveny, X. Edward Guo, Edward F. Wachtel, Thomas A. McMahon, and Wilson C. Hayes. “Trabecular bone exhibits fully linear elastic behavior and yields at low strains”. In: *J. Biomech.* 27.9 (1994). DOI: 10.1016/0021-9290(94)90053-1.

[55] Antonius Rohlmann, Hans Zilch, Georg Bergmann, and R Kölbel. “Material properties of femoral cancellous bone in axial loading. Part I: Time independent properties.” In: *Arch. Orthop. Trauma. Surg.* 97.2 (Sept. 1980), pp. 95–102. DOI: 10.1007/BF00450930.

[56] Ani Ural and Deepak Vashishth. “Effects of intracortical porosity on fracture toughness in aging human bone: a microCT-based cohesive finite element study.” In: *J. Biomech. Eng.* 129.5 (Oct. 2007), pp. 625–31. DOI: 10.1115/1.2768377.

[57] Mitchell B. Schaffler and David B. Burr. “Stiffness of compact bone: effects of porosity and density.” In: *J. Biomech.* 21.1 (1988), pp. 13–6. DOI: 10.1016/0021-9290(88)90186-8.

[58] J C Behrens, P S Walker, and H Shoji. “Variations in strength and structure of cancellous bone at the knee.” In: *J. Biomech.* 7.3 (May 1974), pp. 201–7. DOI: 10.1016/0021-9290(74)90010-4.

[59] Elise F. Morgan, Harun H. Bayraktar, and Tony M. Keaveny. “Trabecular bone modulus-density relationships depend on anatomic site.” In: *J. Biomech.* 36.7 (July 2003), pp. 897–904. DOI: 10.1016/s0021-9290(03)00071-x.

[60] R W McCalden, J A McGeough, M B Barker, and C M Court-Brown. “Age-related changes in the tensile properties of cortical bone. The relative importance of changes in porosity, mineralization, and microstructure.” In: *J. Bone Joint Surg. Am.* 75.8 (Aug. 1993), pp. 1193–205. DOI: 10.2106/00004623-199308000-00009.

[61] D R Carter and W C Hayes. “Bone compressive strength: the influence of density and strain rate.” In: *Science* 194.4270 (Dec. 1976), pp. 1174–6. DOI: 10.1126/science.996549.

[62] R. W. Goulet, S. A. Goldstein, M. J. Ciarelli, J. L. Kuhn, M. B. Brown, and L. A. Feldkamp. “The relationship between the structural and orthogonal compressive properties of trabecular bone”. In: *J. Biomech.* 27.4 (1994). DOI: 10.1016/0021-9290(94)90014-0.

[63] Aaron J. Fields and Tony M. Keaveny. “Trabecular architecture and vertebral fragility in osteoporosis”. In: *Curr. Osteoporos. Rep.* 10.2 (2012), pp. 132–140. DOI: 10.1007/s11914-012-0097-0.

[64] Aaron J. Fields, Gideon L. Lee, X. Sherry Liu, Michael G. Jekir, X. Edward Guo, and Tony M. Keaveny. “Influence of vertical trabeculae on the compressive strength of the human vertebra”. In: *J. Bone Miner. Res.* 26.2 (2011), pp. 263–269. DOI: 10.1002/jbmr.207.

[65] I. H. Parkinson, A. Badiei, M. Stauber, J. Codrington, R. Müller, and N. L. Fazzalari. “Vertebral body bone strength: the contribution of individual trabecular element morphology.” In: *Osteoporos. Int.* 23.7 (July 2012), pp. 1957–65. DOI: 10.1007/s00198-011-1832-6.

[66] John D Currey. “Role of collagen and other organics in the mechanical properties of bone”. In: *Osteoporos. Int.* 14 (Sept. 2003), pp. 29–36. DOI: 10.1007/s00198-003-1470-8.

[67] Andreas Fritsch and Christian Hellmich. “‘Universal’ microstructural patterns in cortical and trabecular, extracellular and extravascular bone materials: Micromechanics-based prediction of anisotropic elasticity”. In: *J. Theor. Biol.* 244.4 (Feb. 2007), pp. 597–620. DOI: 10.1016/j.jtbi.2006.09.013.

[68] Adele L. Boskey and Laurianne Imbert. “Bone quality changes associated with aging and disease: a review”. In: *Ann. N. Y. Acad. Sci.* 1410.1 (Dec. 2017), pp. 93–106. DOI: 10.1111/nyas.13572.

[69] J. Homminga, B. R. McCreadie, T. E. Ciarelli, H. Weinans, S. A. Goldstein, and R. Huiskes. “Cancellous bone mechanical properties from normals and patients with hip fractures differ on the structure level, not on the bone hard tissue level”. In: *Bone* 30.5 (2002), pp. 759–764. DOI: 10.1016/S8756-3282(02)00693-2.

[70] Joshua N Farr and Sundeep Khosla. “Skeletal changes through the lifespan–from growth to senescence.” In: *Nat. Rev. Endocrinol.* 11.9 (Sept. 2015), pp. 513–21. DOI: 10.1038/nrendo.2015.89.

[71] Ego Seeman. “Pathogenesis of bone fragility in women and men.” In: *Lancet (London, England)* 359.9320 (May 2002), pp. 1841–50. DOI: 10.1016/S0140-6736(02)08706-8.

[72] Roger M D Zebaze, Ali Ghasem-Zadeh, Ann Bohte, Sandra Iuliano-Burns, Michiko Mirams, Roger Ian Price, Eleanor J. Mackie, and Ego Seeman. “Intracortical remodelling and porosity in the distal radius and post-mortem femurs of women: a cross-sectional study.” In: *Lancet (London, England)* 375.9727 (May 2010), pp. 1729–36. DOI: 10.1016/S0140-6736(10)60320-0.

[73] Bernard P. Halloran, Virginia L. Ferguson, Steven J. Simske, Andrew Burghardt, Laura L. Venton, and Sharmila Majumdar. “Changes in bone structure and mass with advancing age in the male C57BL/6J mouse”. In: *J. Bone Miner. Res.* 17.6 (2002), pp. 1044–1050. DOI: 10.1359/jbmr.2002.17.6.1044.

[74] Samuel Gourion-Arsiquaud, Jayme C. Burket, Lorena M. Havill, Edward DiCarlo, Stephen B. Doty, Richard Mendelsohn, Marjolein C.H. Van Der Meulen, and Adele L. Boskey. “Spatial variation in osteonal bone properties relative to tissue and animal age”. In: *J. Bone Miner. Res.* 24.7 (2009), pp. 1271–1281. DOI: 10.1359/jbmr.090201.

[75] Jayme Burket, Samuel Gourion-Arsiquaud, Lorena M. Havill, Shefford P. Baker, Adele L. Boskey, and Marjolein C H van der Meulen. “Microstructure and nanomechanical properties in osteons relate to tissue and animal age.” In: *J. Biomech.* 44.2 (Jan. 2011), pp. 277–84. DOI: 10.1016/j.jbiomech.2010.10.018.

[76] Martin Hudelmaier, A. Kollstedt, E. M. Lochmüller, V. Kuhn, F. Eckstein, and T. M. Link. “Gender differences in trabecular bone architecture of the distal radius assessed with magnetic resonance imaging and implications for mechanical competence.” In: *Osteoporos. Int.* 16.9 (Sept. 2005), pp. 1124–33. DOI: 10.1007/s00198-004-1823-y.

[77] E. P. Paschalis, F. Betts, E. DiCarlo, R. Mendelsohn, and A. L. Boskey. “FTIR microspectroscopic analysis of human iliac crest biopsies from untreated osteoporotic bone.” In: *Calcif. Tissue Int.* 61.6 (Dec. 1997), pp. 487–92. DOI: 10.1007/s002239900372.

[78] Jochen G. Hofstaetter, Stefan G. Hofstaetter, Kamilla Nawrot-Wawrzyniak, Helmut Hiertz, Josef G. Grohs, Klemens Trieb, Reinhard Windhager, Klaus Klaushofer, and Paul Roschger. "Mineralization pattern of vertebral bone material following fragility fracture of the spine." In: *J. Orthop. Res.* 30.7 (July 2012), pp. 1089–94. DOI: 10.1002/jor.22026.

[79] P. Roschger, E. P. Paschalis, P. Fratzl, and K. Klaushofer. "Bone mineralization density distribution in health and disease." In: *Bone* 42.3 (Mar. 2008), pp. 456–66. DOI: 10.1016/j.bone.2007.10.021.

[80] E Legrand, D Chappard, C Pascaretti, M Duquenne, S Krebs, V Rohmer, M F Basle, and M Audran. "Trabecular bone microarchitecture, bone mineral density, and vertebral fractures in male osteoporosis." In: *J. Bone Miner. Res.* 15.1 (Jan. 2000), pp. 13–9. DOI: 10.1359/jbmr.2000.15.1.13.

[81] A. L. Boskey, H. Gilder, E. Neufeld, B. Ecarot, and F. H. Glorieux. "Phospholipid changes in the bones of the hypophosphatemic mouse." In: *Bone* 12.5 (1991), pp. 345–51. DOI: 10.1016/8756-3282(91)90021-a.

[82] Ahmed El-Gazzar and Wolfgang Högler. "Mechanisms of Bone Fragility: From Osteogenesis Imperfecta to Secondary Osteoporosis". In: *Int. J. Mol. Sci.* 22.2 (Jan. 2021), p. 625. DOI: 10.3390/ijms22020625.

[83] Mininder S Kocher and James R Kasser. "Osteopetrosis." In: *Am. J. Orthop. (Belle Mead. NJ).* 32.5 (May 2003), pp. 222–8.

[84] Solomon Epstein. "The roles of bone mineral density, bone turnover, and other properties in reducing fracture risk during antiresorptive therapy." In: *Mayo Clin. Proc.* 80.3 (Mar. 2005), pp. 379–88. DOI: 10.4065/80.3.379.

[85] Michael Pazianas, Stefan van der Geest, and Paul Miller. "Bisphosphonates and bone quality". In: *Bonekey Rep.* 3.6 (May 2014), pp. 1020–1025. DOI: 10.1038/bonekey.2014.24.

[86] A. M. Parfitt. "The bone remodeling compartment: a circulatory function for bone lining cells." In: *J. Bone Miner. Res.* 16.9 (Sept. 2001), pp. 1583–5. DOI: 10.1359/jbmr.2001.16.9.1583.

[87] Ramin Oftadeh, Miguel Perez-Viloria, Juan C. Villa-Camacho, Ashkan Vaziri, and Ara Nazarian. "Biomechanics and Mechanobiology of Trabecular Bone: A Review". In: *J. Biomech. Eng.* 137.1 (2015), p. 010802. DOI: 10.1115/1.4029176.

[88] J. Y. Reginster, H. W. Minne, O. H. Sorensen, M. Hooper, C. Roux, M. L. Brandi, B. Lund, D. Ethgen, S. Pack, I. Roumagnac, and R. Eastell. "Randomized trial of the effects of risedronate on vertebral fractures in women with established postmenopausal osteoporosis". In: *Osteoporos. Int.* 11.1 (2000), pp. 83–91. DOI: 10.1007/s001980050010.

[89] Steven T. Harris, Nelson B. Watts, Harry K. Genant, Clark D. McKeever, Thomas Hangartner, Michael Keller, Charles H. Chesnut, Jacques Brown, Erik F. Eriksen, Mohammad S. Hoseyni, Douglas W. Axelrod, and Paul D. Miller. "Effects of risedronate treatment on vertebral and nonvertebral fractures in women with postmenopausal osteoporosis: A randomized controlled trial". In: *J. Am. Med. Assoc.* 282.14 (1999), pp. 1344–1352. DOI: 10.1001/jama.282.14.1344.

[90] Rene Rizzoli, S L Greenspan, G Bone, T J Schnitzer, N B Watts, S Adami, A J Foldes, C Roux, M A Levine, B Uebelhart, A C Santora, A Kaur, C A Peverly, J J Orloff, and Alendronate Once-Weekly Study Group. "Two-year results of once-weekly administration of alendronate 70 mg for the treatment of postmenopausal osteoporosis." In: *J. Bone Miner. Res.* 17.11 (Nov. 2002), pp. 1988–96. DOI: 10.1359/jbmr.2002.17.11.1988.

[91] R. Balena, B. C. Toolan, M. Shea, A. Markatos, E. R. Myers, S. C. Lee, E. E. Opas, J. G. Seedor, H. Klein, and D. Frankenfield. "The effects of 2-year treatment with the aminobisphosphonate alendronate on bone metabolism, bone histomorphometry, and bone strength in ovariectomized nonhuman primates." In: *J. Clin. Invest.* 92.6 (Dec. 1993), pp. 2577–86. DOI: 10.1172/JCI116872.

[92] D W Dempster. "The impact of bone turnover and bone-active agents on bone quality: focus on the hip." In: *Osteoporos. Int.* 13.5 (May 2002), pp. 349–52. DOI: 10.1007/s001980200038.

[93] H. Follet, G. Boivin, C. Rumelhart, and P. J. Meunier. "The degree of mineralization is a determinant of bone strength: A study on human calcanei". In: *Bone* 34.5 (2004), pp. 783–789. DOI: 10.1016/j.bone.2003.12.012.

[94] Richard Eastell, I Barton, Rosemary A. Hannon, A Chines, Patrick Garnero, and Pierre D. Delmas. "Relationship of early changes in bone resorption to the reduction in fracture risk with risedronate." In: *J. Bone Miner. Res.* 18.6 (June 2003), pp. 1051–6. DOI: 10.1359/jbmr.2003.18.6.1051.

[95] Marc C. Hochberg, Susan Greenspan, Richard D. Wasnich, Paul Miller, Desmond E. Thompson, and Philip D. Ross. "Changes in bone density and turnover explain the reductions in incidence of nonvertebral fractures that occur during treatment with antiresorptive agents." In: *J. Clin. Endocrinol. Metab.* 87.4 (Apr. 2002), pp. 1586–92. DOI: 10.1210/jcem.87.4.8415.

[96] Matthew R. Allen. "Recent Advances in Understanding Bisphosphonate Effects on Bone Mechanical Properties". In: *Curr. Osteoporos. Rep.* 16.2 (2018), pp. 198–204. DOI: 10.1007/s11914-018-0430-3.

[97] Brett A. Lenart, Dean G. Lorich, and Joseph M. Lane. "Atypical Fractures of the Femoral Diaphysis in Postmenopausal Women Taking Alendronate". In: *N. Engl. J. Med.* 358.12 (2008), pp. 1304–1306. DOI: 10.1056/nejmc0707493.

[98] Clarita V. Odvina, Joseph E. Zerwekh, D. Sudhaker Rao, Naim Maalouf, Frank A. Gottschalk, and Charles Y.C. Pak. "Severely suppressed bone turnover: A potential complication of alendronate therapy". In: *J. Clin. Endocrinol. Metab.* 90.3 (2005), pp. 1294–1301. DOI: 10.1210/jc.2004-0952.

[99] Matthew R. Allen, Susan Reinwald, and David B. Burr. "Alendronate reduces bone toughness of ribs without significantly increasing microdamage accumulation in dogs following 3 years of daily treatment". In: *Calcif. Tissue Int.* 82.5 (2008), pp. 354–360. DOI: 10.1007/s00223-008-9131-8.

[100] Claire Acevedo, Hrishikesh Bale, Bernd Gludovatz, Amy Wat, Simon Y. Tang, Mingyue Wang, Björn Busse, Elizabeth A. Zimmermann, Eric Schaible, Matthew R. Allen, David B. Burr, and Robert O. Ritchie. "Alendronate treatment alters bone tissues at multiple structural levels in healthy canine cortical bone". In: *Bone* 81 (2015), pp. 352–363. DOI: 10.1016/j.bone.2015.08.002.

[101] Matthew R. Allen and David B. Burr. "Three years of alendronate treatment results in similar levels of vertebral microdamage as after one year of treatment". In: *J. Bone Miner. Res.* 22.11 (2007), pp. 1759–1765. DOI: 10.1359/jbmr.070720.

[102] Jeffrey S Willey, Shane A J Lloyd, Gregory A Nelson, and Ted A Bateman. "Space Radiation and Bone Loss." In: *Gravit. Space Biol. Bull.* 25.1 (2011), pp. 14–21.

[103] Theresa A. Guise. "Bone Loss and Fracture Risk Associated with Cancer Therapy". In: *Oncologist* 11.10 (Nov. 2006), pp. 1121–1131. DOI: 10.1634/theoncologist.11-10-1121.

[104] Jeffrey S. Willey, Shane A. J. Lloyd, Gregory A. Nelson, and Ted A. Bateman. "Ionizing Radiation and Bone Loss: Space Exploration and Clinical Therapy Applications". In: *Clin. Rev. Bone Miner. Metab.* 9.1 (Mar. 2011), pp. 54–62. DOI: 10.1007/s12018-011-9092-8.

[105] Nancy N. Baxter. "Risk of Pelvic Fractures in Older Women Following Pelvic Irradiation". In: *JAMA* 294.20 (Nov. 2005), p. 2587. DOI: 10.1001/jama.294.20.2587.

[106] Sue A. Brown and Theresa A. Guise. "Cancer Treatment-Related Bone Disease". In: *Crit. Rev. Eukaryot. Gene Expr.* 19.1 (2009), pp. 47–60. DOI: 10.1615/CritRevEukarGeneExpr.v19.i1.20.

[107] M. Overgaard. "Spontaneous radiation-induced rib fractures in breast cancer patients treated with postmastectomy irradiation. A clinical radiobiological analysis of the influence of fraction size and dose-response relationships on late bone damage." In: *Acta Oncol.* 27.2 (1988), pp. 117–22. DOI: 10.3109/02841868809090331.

[108] Michael J. Mitchell and P. Mark Logan. "Radiation-induced changes in bone." In: *RadioGraphics* 18.5 (1998), pp. 1125–1136. DOI: 10.1148/radiographics.18.5.9747611.

[109] Jeffrey S. Willey, Shane A. J. Lloyd, Michael E. Robbins, J. Daniel Bourland, Hope Smith-Sielicki, Laura C. Bowman, Robert W. Norrdin, and Ted A. Bateman. "Early Increase in Osteoclast Number in Mice after Whole-Body Irradiation with 2 Gy X Rays". In: *Radiat. Res.* 170.3 (2008), pp. 388–392. DOI: 10.1667/RR1388.1.

[110] Jeffrey S. Willey, Eric W. Livingston, Michael E. Robbins, J. Daniel Bourland, Leidamarie Tirado-Lee, Hope Smith-Sielicki, and Ted A. Bateman. "Risedronate prevents early radiation-induced osteoporosis in mice at multiple skeletal locations". In: *Bone* 46.1 (2010), pp. 101–111. DOI: 10.1016/j.bone.2009.09.002.

[111] X. Cao, X. Wu, D. Frassica, B. Yu, L. Pang, L. Xian, M. Wan, W. Lei, M. Armour, E. Tryggestad, J. Wong, C. Y. Wen, W. W. Lu, and F. J. Frassica. "Irradiation induces bone injury by damaging bone marrow microenvironment for stem cells". In: *Proc. Natl. Acad. Sci.* (2011). DOI: 10.1073/pnas.1103973108.

[112] Hisataka Kondo, Nancy D. Searby, Rose Mojarrab, Jonathan Phillips, Joshua Alwood, Kenji Yumoto, Eduardo A.C. Almeida, Charles L. Limoli, and Ruth K. Globus. "Total-body irradiation of postpubertal mice with 137Cs acutely compromises the microarchitecture of cancellous bone and increases osteoclasts". In: *Radiat. Res.* 171.3 (2009), pp. 283–289. DOI: 10.1667/RR1463.1.

[113] John W. Hopewell. "Radiation-therapy effects on bone density". In: *Med. Pediatr. Oncol.* 41.3 (Sept. 2003), pp. 208–211. DOI: 10.1002/mpo.10338.

[114] H Ergün and W J Howland. "Postradiation atrophy of mature bone." In: *CRC Crit. Rev. Diagn. Imaging* 12.3 (Jan. 1980), pp. 225–43.

[115] J.S. Alwood, K. Yumoto, R. Mojarrab, C.L. Limoli, E.A.C. Almeida, N.D. Searby, and R.K. Globus. "Heavy ion irradiation and unloading effects on mouse lumbar vertebral microarchitecture, mechanical properties and tissue stresses". In: *Bone* 47.2 (Aug. 2010), pp. 248–255. DOI: 10.1016/j.bone.2010.05.004.

[116] James D. Wernle, Timothy A. Damron, Matthew J. Allen, and Kenneth A. Mann. "Local irradiation alters bone morphology and increases bone fragility in a mouse model". In: *J. Biomech.* 43.14 (Oct. 2010), pp. 2738–2746. DOI: 10.1016/j.jbiomech.2010.06.017.

[117] Grant Bevill, Senthil K. Eswaran, Atul Gupta, Panayiotis Papadopoulos, and Tony M. Keaveny. "Influence of bone volume fraction and architecture on computed large-deformation failure mechanisms in human trabecular bone". In: *Bone* 39.6 (Dec. 2006), pp. 1218–1225. DOI: 10.1016/j.bone.2006.06.016.

[118] Harun H. Bayraktar, Elise F. Morgan, Glen L. Niebur, Grayson E. Morris, Eric K. Wong, and Tony M. Keaveny. "Comparison of the elastic and yield properties of human femoral trabecular and cortical bone tissue". In: *J. Biomech.* 37.1 (2004), pp. 27–35. DOI: 10.1016/S0021-9290(03)00257-4.

[119] B. van Rietbergen, H. Weinans, R. Huiskes, and A. Odgaard. “A new method to determine trabecular bone elastic properties and loading using micromechanical finite-element models”. In: *J. Biomech.* 28.1 (1995), pp. 69–81. DOI: 10.1016/0021-9290(95)80008-5.

[120] Grant Bevill, Senthil K. Eswaran, Farhad Farahmand, and Tony M. Keaveny. “The influence of boundary conditions and loading mode on high-resolution finite element-computed trabecular tissue properties”. In: *Bone* 44.4 (2009), pp. 573–578. DOI: 10.1016/j.bone.2008.11.015.

[121] Noah B. Bonnheim and Tony M. Keaveny. “Load-transfer in the human vertebral body following lumbar total disc arthroplasty: Effects of implant size and stiffness in axial compression and forward flexion”. In: *JOR SPINE* 3.1 (Mar. 2020), pp. 1–10. DOI: 10.1002/jsp2.1078.

[122] Benjamin C. Bourne and Marjolein C H Van Der Meulen. “Finite element models predict cancellous apparent modulus when tissue modulus is scaled from specimen CT-attenuation”. In: *J. Biomech.* 37.5 (2004), pp. 613–621. DOI: 10.1016/j.jbiomech.2003.10.002.

[123] Sarah K. Easley, Michael G. Jekir, Andrew J. Burghardt, Mei Li, and Tony M. Keaveny. “Contribution of the intra-specimen variations in tissue mineralization to PTH- and raloxifene-induced changes in stiffness of rat vertebrae.” In: *Bone* 46.4 (Apr. 2010), pp. 1162–9. DOI: 10.1016/j.bone.2009.12.009.

[124] E. Verhulp, B. Van Rietbergen, R. Müller, and R. Huiskes. “Micro-finite element simulation of trabecular-bone post-yield behaviour - Effects of material model, element size and type”. In: *Comput. Methods Biomech. Biomed. Engin.* 11.4 (2008), pp. 389–395. DOI: 10.1080/10255840701848756.

[125] Saghi Sadoughi, Annika Vom Scheidt, Shashank Nawathe, Shan Zhu, Ariana Moini, and Tony M. Keaveny. “Effect of variations in tissue-level ductility on human vertebral strength.” In: *Bone* 137.5 (2020), p. 115445. DOI: 10.1016/j.bone.2020.115445.

[126] O. C. Yeh and T. M. Keaveny. “Biomechanical effects of intraspecimen variations in trabecular architecture: A three-dimensional finite element study”. In: *Bone* 25.2 (1999), pp. 223–228. DOI: 10.1016/S8756-3282(99)00092-7.

[127] Haisheng Yang, Shashank Nawathe, Aaron J. Fields, and Tony M. Keaveny. “Micromechanics of the human vertebral body for forward flexion”. In: *J. Biomech.* 45.12 (2012), pp. 2142–2148. DOI: 10.1016/j.jbiomech.2012.05.044.

[128] Senthil K. Eswaran, Atul Gupta, Mark F. Adams, and Tony M. Keaveny. “Cortical and trabecular load sharing in the human vertebral body”. In: *J. Bone Miner. Res.* 21.2 (Nov. 2006), pp. 307–314. DOI: 10.1359/jbmr.2006.21.2.307.

[129] Senthil K. Eswaran, Atul Gupta, and Tony M. Keaveny. “Locations of bone tissue at high risk of initial failure during compressive loading of the human vertebral body”. In: *Bone* 41.4 (Oct. 2007), pp. 733–739. DOI: 10.1016/j.bone.2007.05.017.

[130] David C. Lee, Aurore Varela, Paul J. Kostenuik, Michael S. Ominsky, and Tony M. Keaveny. "Finite Element Analysis of Denosumab Treatment Effects on Vertebral Strength in Ovariectomized Cynomolgus Monkeys". In: *J. Bone Miner. Res.* 31.8 (2016), pp. 1586–1595. DOI: 10.1002/jbmr.2830.

[131] T. Adachi, K. I. Tsubota, Y. Tomita, and J. H. Scott. "Trabecular surface remodeling simulation for cancellous bone using microstructural voxel finite element models". In: *J. Biomech. Eng.* 123.5 (2001), pp. 403–409. DOI: 10.1115/1.1392315.

[132] Dan Wu, Per Isaksson, Stephen J. Ferguson, and Cecilia Persson. "Young's modulus of trabecular bone at the tissue level: A review". In: *Acta Biomater.* 78 (2018), pp. 1–12. DOI: 10.1016/j.actbio.2018.08.001.

[133] Silvio Lorenzetti, Roberto Carretta, Ralph Müller, and Edgar Stüssi. "A new device and method for measuring the elastic modulus of single trabeculae". In: *Med. Eng. Phys.* 33.8 (2011), pp. 993–1000. DOI: 10.1016/j.medengphy.2011.03.012.

[134] A. J C Ladd, J. H. Kinney, D. L. Haupt, and S. A. Goldstein. "Finite-element modeling of trabecular bone: Comparison with mechanical testing and determination of tissue modulus". In: *J. Orthop. Res.* 16.5 (1998), pp. 622–628. DOI: 10.1002/jor.1100160516.

[135] J. C. Lotz, E. J. Cheal, and W. C. Hayes. "Fracture Prediction for the Proximal Femur Using Finite Element Models: Part II—Nonlinear Analysis". In: *J. Biomech. Eng.* 113.4 (Nov. 1991), pp. 361–365. DOI: 10.1115/1.2895413.

[136] J C Lotz, E J Cheal, and W C Hayes. "Fracture Prediction for the Proximal Femur Using Finite Element Models: Part I—Linear Analysis". In: *J. Biomech. Eng.* 113.4 (Nov. 1991), pp. 353–360. DOI: 10.1115/1.2895412.

[137] B T Allaire, D Lu, F Johannesdottir, D Kopperdahl, T M Keaveny, M Jarraya, A Guermazi, M. A. Bredella, E. J. Samelson, D. P. Kiel, D. E. Anderson, S. Demissie, and M. L. Bouxsein. "Prediction of incident vertebral fracture using CT-based finite element analysis". In: *Osteoporos. Int.* 30.2 (Feb. 2019), pp. 323–331. DOI: 10.1007/s00198-018-4716-1.

[138] B. van Rietbergen and K. Ito. "A survey of micro-finite element analysis for clinical assessment of bone strength: The first decade". In: *J. Biomech.* 48.5 (2015), pp. 832–841. DOI: 10.1016/j.jbiomech.2014.12.024.

[139] David L. Kopperdahl, Thor Aspelund, Paul F. Hoffmann, Sigurdur Sigurdsson, Kristin Siggeirsdottir, Tamara B. Harris, Vilmundur Gudnason, and Tony M. Keaveny. "Assessment of incident spine and hip fractures in women and men using finite element analysis of CT scans". In: *J. Bone Miner. Res.* 29.3 (Mar. 2014), pp. 570–580. DOI: 10.1002/jbmr.2069.

[140] Uwe Wolfram, Hans Joachim Wilke, and Philippe K. Zysset. "Valid μ finite element models of vertebral trabecular bone can be obtained using tissue properties measured with nanoindentation under wet conditions". In: *J. Biomech.* 43.9 (2010), pp. 1731–1737. DOI: 10.1016/j.jbiomech.2010.02.026.

[141] Grant Bevill and Tony M. Keaveny. “Trabecular bone strength predictions using finite element analysis of micro-scale images at limited spatial resolution”. In: *Bone* 44.4 (2009), pp. 579–584. DOI: 10.1016/j.bone.2008.11.020.

[142] Xiang Wang, Arnav Sanyal, Peggy M Cawthon, Lisa Palermo, Michael Jekir, John Christensen, Kristine E Ensrud, Steven R Cummings, Eric Orwoll, Dennis M Black, and Tony M Keaveny. “Prediction of new clinical vertebral fractures in elderly men using finite element analysis of CT scans”. In: *J. Bone Miner. Res.* 27.4 (Apr. 2012), pp. 808–816. DOI: 10.1002/jbmr.1539.

[143] Megan M. Pendleton, Saghi Sadoughi, Alfred Li, Grace D. O’Connell, Joshua S. Alwood, and Tony M. Keaveny. “High-precision method for cyclic loading of small-animal vertebrae to assess bone quality”. In: *Bone Reports* 9.October (Dec. 2018), pp. 165–172. DOI: 10.1016/j.bonr.2018.10.002.

[144] M Adams, H Bayraktar, Keaveny, and P Papadopoulos. “Ultrascalable implicit finite element analysis in solid mechanics with over half a billion degrees of freedom”. In: *ACM/IEEE Proc. SC2004 High Perform. Netw. Comput.* 2004, pp. 1–15. DOI: 10.1109/SC.2004.62.

[145] R L Taylor. {*FEAP*} - *Finite Element Analysis Program*. 2014.

[146] Megan M. Pendleton, Shannon R. Emerzian, Saghi Sadoughi, Alfred Li, Jennifer W. Liu, Simon Y. Tang, Grace D. O’Connell, Jean D. Sibonga, Joshua S. Alwood, and Tony M. Keaveny. “Relations Between Bone Quantity, Microarchitecture, and Collagen Cross-links on Mechanics Following In Vivo Irradiation in Mice.” In: *JBMR plus* 5.11 (Nov. 2021), e10545. DOI: 10.1002/jbm4.10545.

[147] Megan M. Pendleton, Shannon R. Emerzian, Jennifer Liu, Simon Y. Tang, Grace D. O’Connell, Joshua S. Alwood, and Tony M. Keaveny. “Effects of ex vivo ionizing radiation on collagen structure and whole-bone mechanical properties of mouse vertebrae”. In: *Bone* 128.June (Nov. 2019), p. 115043. DOI: 10.1016/j.bone.2019.115043.

[148] Aaron J. Fields, Senthil K. Eswaran, Michael G. Jekir, and Tony M. Keaveny. “Role of Trabecular Microarchitecture in Whole-Vertebral Body Biomechanical Behavior”. In: *J. Bone Miner. Res.* 24.9 (Sept. 2009), pp. 1523–1530. DOI: 10.1359/jbmr.090317.

[149] Aaron J. Fields, Shashank Nawathe, Senthil K. Eswaran, Michael G. Jekir, Mark F. Adams, Panayiotis Papadopoulos, and Tony M. Keaveny. “Vertebral fragility and structural redundancy”. In: *J. Bone Miner. Res.* 27.10 (Oct. 2012), pp. 2152–2158. DOI: 10.1002/jbmr.1664.

[150] Jae Young Rho, Liisa Kuhn-Spearing, and Peter Zioupos. “Mechanical properties and the hierarchical structure of bone.” In: *Med. Eng. Phys.* 20.2 (Mar. 1998), pp. 92–102. DOI: 10.1016/s1350-4533(98)00007-1.

[151] Joshua S. Alwood, Akhilesh Kumar, Luan H. Tran, Angela Wang, Charles L. Limoli, and Ruth K. Globus. “Low-dose, ionizing radiation and age-related changes in skeletal microarchitecture”. In: *J. Aging Res.* 2012 (2012), pp. 1–7. DOI: 10.1155/2012/481983.

[152] Mohammad Shahnazari, Wei Yao, WeiWei Dai, Bob Wang, Sophi S. Ionova-Martin, Robert O. Ritchie, Daniel Heeren, Andrew J. Burghardt, Daniel P. Nicolella, Michael G. Kimiecik, and Nancy E. Lane. "Higher doses of bisphosphonates further improve bone mass, architecture, and strength but not the tissue material properties in aged rats". In: *Bone* 46.5 (May 2010), pp. 1267–1274. DOI: 10.1016/j.bone.2009.11.019.

[153] Yoshiki Yamagami, Tasuku Mashiba, Ken Iwata, Makoto Tanaka, Kazutoshi Nozaki, and Tetsuji Yamamoto. "Effects of minodronic acid and alendronate on bone remodeling, microdamage accumulation, degree of mineralization and bone mechanical properties in ovariectomized cynomolgus monkeys". In: *Bone* 54.1 (May 2013), pp. 1–7. DOI: 10.1016/j.bone.2013.01.016.

[154] Takashi Igarashi, Satoru Demura, Satoshi Kato, Kazuya Shinmura, Noriaki Yokogawa, Noritaka Yonezawa, Takaki Shimizu, Norihiro Oku, Hideki Murakami, and Hiroyuki Tsuchiya. "Effects of Radiation on the Bone Strength of Spinal Vertebrae in Rats". In: *Spine (Phila. Pa. 1976)*. Publish Ah.19 (Nov. 2021), E1022–E1030. DOI: 10.1097/BRS.0000000000004282.

[155] Yuan Chen, Enrico DallAra, Erika Sales, Krishnagoud Manda, Robert Wallace, Pankaj Pankaj, and Marco Viceconti. "Micro-CT based finite element models of cancellous bone predict accurately displacement once the boundary condition is well replicated: A validation study". In: *J. Mech. Behav. Biomed. Mater.* 65.September 2016 (2017), pp. 644–651. DOI: 10.1016/j.jmbbm.2016.09.014.

[156] M.G. Goff, F.M. Lambers, R.M. Sorna, T.M. Keaveny, and C.J. Hernandez. "Finite element models predict the location of microdamage in cancellous bone following uniaxial loading". In: *J. Biomech.* 48.15 (Nov. 2015), pp. 4142–4148. DOI: 10.1016/j.jbiomech.2015.10.023.

[157] Jeffry S Nyman, Sasidhar Uppuganti, Alexander J Makowski, Barbara J Rowland, Alyssa R Merkel, Julie A Sterling, Todd L Bredbenner, and Daniel S Perrien. "Predicting mouse vertebra strength with micro-computed tomography-derived finite element analysis". In: *Bonekey Rep.* 4.August 2014 (2015), pp. 1–11. DOI: 10.1038/bonekey.2015.31.

[158] Roberto Carretta, Benoit Luisier, Daniel Bernoulli, Edgar Stüssi, Ralph Müller, and Silvio Lorenzetti. "Novel method to analyze post-yield mechanical properties at trabecular bone tissue level". In: *J. Mech. Behav. Biomed. Mater.* 20 (Apr. 2013), pp. 6–18. DOI: 10.1016/j.jmbbm.2012.12.003.

[159] Glen L. Niebur, Michael J. Feldstein, Jonathan C. Yuen, Tony J. Chen, and Tony M. Keaveny. "High-resolution finite element models with tissue strength asymmetry accurately predict failure of trabecular bone". In: *J. Biomech.* 33.12 (Dec. 2000), pp. 1575–1583. DOI: 10.1016/S0021-9290(00)00149-4.

[160] Noah B. Bonnheim, Mark F. Adams, Tongge Wu, and Tony M. Keaveny. "The Role of Vertebral Porosity and Implant Loading Mode on Bone-Tissue Stress in the Human Vertebral Body Following Lumbar Total Disc Arthroplasty". In: *Spine (Phila. Pa. 1976)*. 46.19 (Oct. 2021), E1022–E1030. DOI: 10.1097/BRS.0000000000004023.

[161] G. L. Niebur, J. C. Yuen, A. C. Hsia, and T. M. Keaveny. "Convergence behavior of high-resolution finite element models of trabecular bone." In: *J. Biomech. Eng.* 121.6 (Dec. 1999), pp. 629–35. DOI: 10.1115/1.2800865.

[162] Shashank Nawathe, Bich Phuong Nguyen, Nasim Barzanian, Hosna Akhlaghpour, Mary L. Bouxsein, and Tony M. Keaveny. "Cortical and trabecular load sharing in the human femoral neck". In: *J. Biomech.* 48.5 (2015). DOI: 10.1016/j.jbiomech.2014.12.022.

[163] Eric R. Bandstra, Michael J. Pecaut, Erica R. Anderson, Jeffrey S. Willey, Francesco De Carlo, Stuart R. Stock, Daila S. Gridley, Gregory A. Nelson, Howard G. Levine, and Ted A. Bateman. "Long-term dose response of trabecular bone in mice to proton radiation". In: *Radiat. Res.* 169.6 (June 2008), pp. 607–614. DOI: 10.1667/RR1310.1.

[164] Eric R. Bandstra, Raymond W. Thompson, Gregory A. Nelson, Jeffrey S. Willey, Stefan Judex, Mark A. Cairns, Eric R. Benton, Marcelo E. Vazquez, James A. Carson, and Ted A. Bateman. "Musculoskeletal changes in mice from 2050 cGy of simulated galactic cosmic rays". In: *Radiat. Res.* 172.1 (2009), pp. 21–29. DOI: 10.1667/RR1509.1.

[165] S. A. Hamilton, M. J. Pecaut, D. S. Gridley, N. D. Travis, E. R. Bandstra, J. S. Willey, G. A. Nelson, and T. A. Bateman. "A murine model for bone loss from therapeutic and space-relevant sources of radiation". In: *J. Appl. Physiol.* 101.3 (2006), pp. 789–793. DOI: 10.1152/japplphysiol.01078.2005.

[166] Jasper Homminga, Barbara R. Mccreadie, Harrie Weinans, and Rik Huiskes. "The dependence of the elastic properties of osteoporotic cancellous bone on volume fraction and fabric". In: *J. Biomech.* 36.10 (2003), pp. 1461–1467. DOI: 10.1016/S0021-9290(03)00125-8.

[167] Ji Wang, Bin Zhou, X. Sherry Liu, Aaron J. Fields, Arnav Sanyal, Xiutao Shi, Mark Adams, Tony M. Keaveny, and X. Edward Guo. "Trabecular plates and rods determine elastic modulus and yield strength of human trabecular bone". In: *Bone* 72 (2015), pp. 71–80. DOI: 10.1016/j.bone.2014.11.006.

[168] Jesper Kabel, Bert Van Rietbergen, Michel Dalstra, Anders Odgaard, and Rik Huiskes. "The role of an effective isotropic tissue modulus in the elastic properties of cancellous bone". In: *J. Biomech.* 32.7 (1999), pp. 673–680. DOI: 10.1016/S0021-9290(99)00045-7.

[169] Elizabeth A. Zimmermann and Robert O. Ritchie. "Bone as a Structural Material". In: *Adv. Healthc. Mater.* 4.9 (2015), pp. 1287–1304. DOI: 10.1002/adhm.201500070.

[170] Kenji Yumoto, Ruth K. Globus, Rose Mojarrab, Joy Arakaki, Angela Wang, Nancy D. Searby, Eduardo A.C. Almeida, and Charles L. Limoli. "Short-term effects of whole-body exposure to 56fe ions in combination with musculoskeletal disuse on bone cells". In: *Radiat. Res.* 173.4 (2010), pp. 494–504. DOI: 10.1667/RR1754.1.

[171] Hisataka Kondo, Kenji Yumoto, Joshua S. Alwood, Rose Mojarrab, Angela Wang, Eduardo A.C. Almeida, Nancy D. Searby, Charles L. Limoli, and Ruth K. Globus. "Oxidative stress and gamma radiation-induced cancellous bone loss with musculoskeletal disuse". In: *J. Appl. Physiol.* 108.1 (2010), pp. 152–161. DOI: 10.1152/japplphysiol.00294.2009.

[172] Megan E. Oest, Bo Gong, Karen Esmonde-White, Kenneth A. Mann, Nicholas D. Zimmerman, Timothy A. Damron, and Michael D. Morris. "Parathyroid hormone attenuates radiation-induced increases in collagen crosslink ratio at periosteal surfaces of mouse tibia". In: *Bone* 86 (2016), pp. 91–97. DOI: 10.1016/j.bone.2016.03.003.

[173] Megan E. Oest and Timothy A. Damron. "Focal Therapeutic Irradiation Induces an Early Transient Increase in Bone Glycation". In: *Radiat. Res.* 181.4 (2014), pp. 439–443. DOI: 10.1667/rr13451.1.

[174] H. J. Williams and A. M. Davies. "The effect of X-rays on bone: A pictorial review". In: *Eur. Radiol.* 16.3 (2006), pp. 619–633. DOI: 10.1007/s00330-005-0010-7.

[175] Katelyn Burkhart, Brett Allaire, Dennis E. Anderson, David Lee, Tony M. Keaveny, and Mary L. Bouxsein. "Effects of Long-Duration Spaceflight on Vertebral Strength and Risk of Spine Fracture". In: *J. Bone Miner. Res.* 35.2 (2020), pp. 269–276. DOI: 10.1002/jbmr.3881.

[176] Shashank Nawathe, Hosna Akhlaghpour, Mary L. Bouxsein, and Tony M. Keaveny. "Microstructural Failure Mechanisms in the Human Proximal Femur for Sideways Fall Loading". In: *J. Bone Miner. Res.* 29.2 (Feb. 2014), pp. 507–515. DOI: 10.1002/jbmr.2033.

[177] Lis Mosekilde. "Vertebral structure and strength In vivo and In vitro". In: *Calcif. Tissue Int.* 53.1 Supplement (1993), pp. 121–126. DOI: 10.1007/BF01673420.

[178] Matthew R. Allen, Ken Iwata, Roger Phipps, and David B. Burr. "Alterations in canine vertebral bone turnover, microdamage accumulation, and biomechanical properties following 1-year treatment with clinical treatment doses of risedronate or alendronate". In: *Bone* 39.4 (2006), pp. 872–879. DOI: 10.1016/j.bone.2006.04.028.

[179] A. M. Parfitt. "Age-related structural changes in trabecular and cortical bone: Cellular mechanisms and biomechanical consequences". In: *Calcif. Tissue Int.* 36.1 Supplement (1984). DOI: 10.1007/BF02406145.

[180] Shashank Nawathe, Frédéric Juillard, and Tony M. Keaveny. "Theoretical bounds for the influence of tissue-level ductility on the apparent-level strength of human trabecular bone". In: *J. Biomech.* 46.7 (Apr. 2013), pp. 1293–1299. DOI: 10.1016/j.jbiomech.2013.02.011.

[181] Panayiotis Papadopoulos and Jia Lu. "A general framework for the numerical solution of problems in finite elasto-plasticity". In: *Comput. Methods Appl. Mech. Eng.* 159.1-2 (July 1998), pp. 1–18. DOI: 10.1016/S0045-7825(98)80101-1.

[182] Dale Johnson, Summer E. Lawrence, Eric W. Livingston, Robert D. Hienz, Catherine M. Davis, and Anthony G. Lau. "Modeling Space Radiation Induced Bone Changes in Rat Femurs through Finite Element Analysis". In: *2018 40th Annu. Int. Conf. IEEE Eng. Med. Biol. Soc.* Vol. 2018-July. July 2018, pp. 1763–1766. DOI: 10.1109/EMBC.2018.8512620.

[183] Vaida Glatt, Ernesto Canalis, Lisa Stadmeyer, and Mary L. Bouxsein. "Age-related changes in trabecular architecture differ in female and male C57BL/6J mice". In: *J. Bone Miner. Res.* 22.8 (2007), pp. 1197–1207. DOI: 10.1359/jbmr.070507.

[184] N. Dalzell, S. Kaptoge, N. Morris, A. Berthier, B. Koller, L. Braak, B. van Rietbergen, and J. Reeve. "Bone micro-architecture and determinants of strength in the radius and tibia: age-related changes in a population-based study of normal adults measured with high-resolution pQCT". In: *Osteoporos. Int.* 20.10 (Oct. 2009), pp. 1683–1694. DOI: 10.1007/s00198-008-0833-6.

[185] Tasuku Mashiba, Mitsuru Saito, Yoshiki Yamagami, Makoto Tanaka, Ken Iwata, and Tetsuji Yamamoto. "Effects of suppressed bone remodeling by minodronic acid and alendronate on bone mass, microdamage accumulation, collagen crosslinks and bone mechanical properties in the lumbar vertebra of ovariectomized cynomolgus monkeys". In: *Bone* 97 (2017), pp. 184–191. DOI: 10.1016/j.bone.2017.01.008.

[186] Aaron J. Fields, Gideon L. Lee, and Tony M. Keaveny. "Mechanisms of initial endplate failure in the human vertebral body". In: *J. Biomech.* 43.16 (Dec. 2010), pp. 3126–3131. DOI: 10.1016/j.jbiomech.2010.08.002.

[187] Panos Tsopelas and Mohamed Husain. "Measures of Structural Redundancy in Reinforced Concrete Buildings. II: Redundancy Response Modification Factor RR". In: *J. Struct. Eng.* 130.11 (Nov. 2004), pp. 1659–1666. DOI: 10.1061/(ASCE)0733-9445(2004)130:11(1659).

[188] Mohamed Husain and Panos Tsopelas. "Measures of Structural Redundancy in Reinforced Concrete Buildings. I: Redundancy Indices". In: *J. Struct. Eng.* 130.11 (Nov. 2004), pp. 1651–1658. DOI: 10.1061/(ASCE)0733-9445(2004)130:11(1651).

[189] E. Acar, A. Kale, and R. T. Haftka. "Comparing Effectiveness of Measures That Improve Aircraft Structural Safety". In: *J. Aerosp. Eng.* 20.3 (July 2007), pp. 186–199. DOI: 10.1061/(ASCE)0893-1321(2007)20:3(186).

[190] Dan M. Frangopol and James P. Curley. "Effects of Damage and Redundancy on Structural Reliability". In: *J. Struct. Eng.* 113.7 (July 1987), pp. 1533–1549. DOI: 10.1061/(ASCE)0733-9445(1987)113:7(1533).

[191] Yoshihiro Kanno and Yakov Ben-Haim. "Redundancy and Robustness, or When Is Redundancy Redundant?" In: *J. Struct. Eng.* 137.9 (Sept. 2011), pp. 935–945. DOI: 10.1061/(ASCE)ST.1943-541X.0000416.

[192] Z.X. Fang and H.T. Fan. “Redundancy of Structural Systems in the Context of Structural Safety”. In: *Procedia Eng.* 14 (2011), pp. 2172–2178. DOI: 10.1016/j.proeng.2011.07.273.

[193] Dusan Krajcinovic and Manuel Americo G. Silva. “Statistical aspects of the continuous damage theory”. In: *Int. J. Solids Struct.* 18.7 (1982), pp. 551–562. DOI: 10.1016/0020-7683(82)90039-7.

[194] J. D. Currey. “The many adaptations of bone.” In: *J. Biomech.* 36.10 (Oct. 2003), pp. 1487–95. DOI: 10.1016/s0021-9290(03)00124-6.

[195] J. Homminga, B. Van-Rietbergen, E. M. Lochmüller, H. Weinans, F. Eckstein, and R. Huiskes. “The osteoporotic vertebral structure is well adapted to the loads of daily life, but not to infrequent ”error” loads.” In: *Bone* 34.3 (Mar. 2004), pp. 510–6. DOI: 10.1016/j.bone.2003.12.001.

[196] Saghi Sadoughi. “Micromechanics of Human Bone: Role of Architecture and Tissue Material Properties”. PhD thesis. UC Berkeley., 2019.

[197] Alexander G. Bruno, Kerry E. Broe, Xiaochun Zhang, Elizabeth J. Samelson, Ching An Meng, Rajaram Manoharan, John D’Agostino, L. Adrienne Cupples, Douglas P. Kiel, and Mary L. Bouxsein. “Vertebral size, bone density, and strength in men and women matched for age and areal spine BMD”. In: *J. Bone Miner. Res.* 29.3 (2014), pp. 562–569. DOI: 10.1002/jbmr.2067.

[198] Laura A.G. Armas and Robert R. Recker. “Pathophysiology of Osteoporosis. New Mechanistic Insights.” In: *Endocrinol. Metab. Clin. North Am.* 41.3 (2012), pp. 475–486. DOI: 10.1016/j.ecl.2012.04.006.

[199] Marjolein Van der Klift, Chris E D H De Laet, Eugene V. McCloskey, Albert Hofman, and Huibert A P Pols. “The incidence of vertebral fractures in men and women: the Rotterdam Study.” In: *J. Bone Miner. Res.* 17.6 (June 2002), pp. 1051–6. DOI: 10.1359/jbmr.2002.17.6.1051.